Automated dual-tip scanning near-field optical microscope for investigation of nanophotonic systems

Dissertation
zur Erlangung des akademischen Grades
doctor rerum naturalium (Dr. rer. nat.)

vorgelegt dem Rat der Physikalisch-Astronomischen Fakultät
der Friedrich-Schiller-Universität Jena

von Msc. Photonics. Najmeh Abbasirad
geboren in Zahedan, Iran

Gutachter:

1. Prof. Dr. Thomas Pertsch, Friedrich-Schiller-Universität Jena

2. Prof. Dr. Achim Hartschuh, Ludwig-Maximilians-Universität München

3. Prof. Dr. Lukas M. Eng, Technische Universität Dresden

Tag der Disputation: 04.07.2022

Table of Contents

1 Introduction

The human curiosity about nature and our surrounding environment arises primarily from visual perception. Amid the scientific revolution, visual observation was regarded as the ultimate methodological approach in terms of reliability. However, a variety of natural phenomena are at scales that human eyes cannot perceive, whether far-distanced stars and planets or tiny elements with subatomic sizes. The evolutionary process of explaining such physical phenomena has always been tied to the development of optical instruments. The explanation of physical phenomena was evolved from philosophical assumptions in ancient times to the current state of complex experiments to verify theoretical models. Many theoretical models that account for physical phenomena in nature have gained credibility through experiments. The close link between systematic experiments using the state-of-the-art instruments and conceptualizing new ideas according to those experiments underpins the growth of natural sciences.

One of the instruments that revolutionized the research in natural sciences is the optical microscope. Optical microscopes are indispensable imaging devices to study optical phenomena in scales that human vision is blind to observe. The ability of optical microscopes to resolve details of objects is described by the optical resolution. By definition, the optical resolution is the shortest distance between two point-like objects that can still be resolved with a microscope. It has long been acknowledged that optical microscopes have limited resolution due to the diffraction limit of light. Hence, ideas to break the diffraction limit until their implementation have a history of a century [1, 2].

The resolution of optical microscopes depends on the numerical aperture (NA) of the objective and the illumination wavelength. The Rayleigh criterion describes

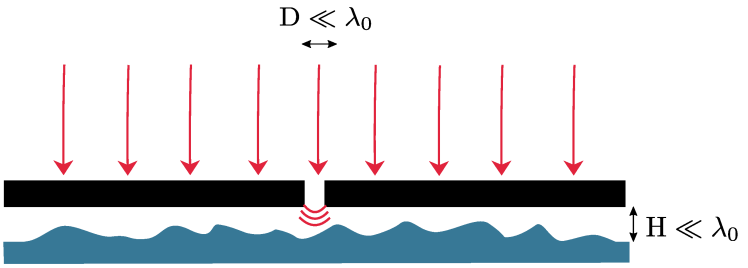

Figure 1.1: Schematic of the proposed idea by Synge to overcome the diffraction limit. The opaque metal film with a subwavelength aperture D $\ll \lambda_0$ scans the sample at a distance H $\ll \lambda_0$. The diameter of the aperture is D and λ_0 is the illumination wavelength.

the diffraction limit of an optical microscope as $\Delta x = \frac{\lambda_0}{2\mathrm{NA}}$, where λ_0 is the illumination wavelength in free space and the numerical aperture $\mathrm{NA} = n\sin\alpha$ relies on the refractive index of the medium n, and its maximum collection angle α of the microscope objective [3]. Thus, the detection and illumination of light always suffer from a so-called diffraction limit when microscope objectives are involved.

A plane wave in free space follows the dispersion relation $k = \sqrt{{k_x}^2 + {k_y}^2 + {k_z}^2}$ with the wave number $k = \frac{2\pi}{\lambda_0}$ [4]. If a plane wave illuminates a subwavelength structure and the wave vectors of the scattered light from the subwavelength structure are characterized by ${k_x}^2 + {k_y}^2 \leq k^2$, the scattered light propagates in free space where it can be collected by an objective. If the wave vectors of the scattered light fulfill the condition ${k_x}^2 + {k_y}^2 > k^2$; they give rise to evanescent waves, which decay exponentially at a small distance away from the sample plane. These evanescent waves contain high spatial frequency information associated with subwavelength features of the sample. The origin of the diffraction limit is related to evanescent waves. Therefore, the detection of evanescent waves is the key solution to circumvent the diffraction limit [5].

In 1928, as a prime example of a person being ahead of time, Synge proposed to image through a subwavelength aperture in an opaque screen that scans within a small distance from the sample (Fig. 1.1). Synge's idea is based on the excitation of evanescent waves. Through a spatially confined aperture, mostly evanescent waves are excited with wave vectors larger than those allowed with propagating plane waves. When these evanescent waves interact with the sample, they provide high spatial frequency information about the optical properties of the sample. However, at that time, a lack of precise positioning technique and appropriate illumination source hampered the realization of Synge's idea [6]. After the invention of the scanning tunneling microscope [7], nanoscale positioning technology became available. The first near-field

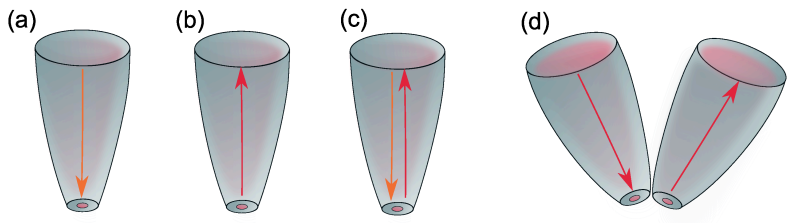

Figure 1.2: Schematics of different SNOM operation modes (a) Illumination (b) Collection (c) Illumination-collection (d) Dual-tip SNOM.

scanning optical microscope (SNOM) was realized in 1984 [8, 9]. A tapered quartz rod with a metallic coating was used as an alternative to an aperture in an opaque screen [8]. Since then, tapered optical fibers with a metallic coating and a small aperture left uncoated at the apex have become the most commonly used SNOM tips [10]. The aperture fiber tip attached to a piezoelectric tuning fork oscillates with the resonance frequency of the tuning fork while approaching the sample to perform near-field measurements. After a safe tip approach, the aperture tip raster scans the sample surface and excites or collects evanescent waves in the near field. The resolution of the aperture tip SNOM depends on the aperture diameter, and its distance from a surface [11–13].

The emergence of near-field optical microscopy coincided with the development of nanofabrication technologies to scale down and miniaturize dielectric and plasmonic nanostructures beyond the diffraction limit [14–16]. A variety of nanophotonic systems using photons instead of electrons as information carriers were proposed in response to demands for faster and smaller photonic devices.

To investigate different optical properties of these subwavelength nanostructures, various SNOM configurations were suggested [17, 18]. Figure 1.2 illustrates different schemes of SNOM operation modes. In the illumination mode (Fig. 1.2(a)), the aperture tip illuminates a sample through a subwavelength aperture. The evanescent waves that pass through the sample or scattered are collected with a microscope objective in the far field. The aperture tip in illumination mode has been widely used to characterize plasmonic nanostructures [19]. The advancement in the field of plasmonics is intertwined with SNOM measurements. The emitted radiation from an aperture tip near a gold or silver film acts as a point source for the excitation of surface plasmon polaritons (SPPs). The scattering, reflection, or interference of SPPs due to the structured plasmonic material is manifest in the modified emission pattern [20]. The theoretical model for describing the emission from the subwavelength

metallic aperture in both near and far field was proposed by Bethe and Bouwkamp using diffraction theory [21, 22]. Because of the similarity of the aperture tip with a subwavelength aperture in the metallic film, several studies were carried out in the far field and near field to investigate the electromagnetic field distribution near the aperture tips [23–25] or subwavelength aperture in the metallic film [26]. All those measurements confirmed that the emission from the aperture tip resembles the dipolar source radiation. However, the combination of electric and magnetic dipoles to model a particular aperture tip relies on the tips' geometry and materials used in fabrication. [27–30]. As long as aperture SNOM tips are not identical, properties of dipolar emission from the individual aperture tip needed to be characterized for polarization-resolved near-field measurements.

In one of the breakthrough experiments using the SNOM in illumination mode, grafting a fluorescent molecule on the apex of the SNOM tip resulted in a more confined illumination source to image a subwavelength nanostructure [12]. This measurement inspired more near-field experiments based on active probes including fluorescent molecules [31, 32], nanocrystal quantum dots [33, 34], nitrogen-vacancy color centers [35–37], and rare-earth atoms [38], grafted at the extremity of the SNOM tip. If a quantum emitter is attached to the apex of the SNOM tip, a more confined point source or a higher resolution near-field image can be achieved [13]. To understand the image formation in the illumination mode SNOM, aperture tips and active probes are viewed as dipolar sources [25, 28, 39–41]. In this regard, the local density of optical states (LDOS) of the surrounding medium is the quantity to be investigated when it comes to the radiated power of a dipole in the classical picture or the spontaneous decay rate of active probes in the quantum picture [42].

In the classical picture, LDOS quantifies the number of available modes in the medium for a particular oscillation frequency and dipole position. The near-field intensity distribution is the result of all excited modes due to the dipolar emission from the aperture tip. Moreover, the dipolar emission from the aperture tip mimics a dipole radiation. Hence, the LDOS of a nanostructured sample is the most relevant quantity to describe the obtained image in the illumination mode [43, 44]. Since the emission from quantum emitters or aperture tips has vectorial nature, only the partial LDOS can be measured in the illumination mode [45]. The partial LDOS indicates how strong is the interaction of a dipole having a specific orientation with each of the excited modes in its surrounding environment [42]. The subwavelength characteristics of the nanostructures leads to the nonradiative modes dominating the partial LDOS in

the near field [43, 45]. To map the LDOS of nanostructures using a single SNOM tip, in illumination mode, the radiative components of the transmitted light are filtered, and thus the angular detection of evanescent waves is carried out in the far field. The corresponding collected intensity map is the partial LDOS of a nanostructure at the excitation position [45–47]. However, if an aperture tip is employed for partial LDOS measurements, its dipolar emission pattern in the near field should be characterized in advance [48]. The map of LDOS obtained using illumination SNOM or lifetime imaging of active probes [31] provides information regarding a position and frequency where the radiation is enhanced or suppressed. However, no near-field information regarding the electromagnetic field distribution due to a quantum emitter interaction with a photonic system is accessible in the illumination mode.

Currently, real-world applications of quantum technology emerge from the quantum photonics research. In this regard, single photon sources are critical components for quantum information processing [49, 50] and quantum sensing [51–53]. The realization of efficient single-photon sources requires the enhancement of the spontaneous decay rate of quantum emitters. When a quantum emitter is placed near photonic nanostructures [54] such as nanoantennas [32, 55, 56], photonic crystal cavities [57, 58], or metasurfaces [59], their spontaneous decay rate is modified resulting in the enhancement of their power radiation in the far field. Accordingly, nanoantennas with different geometries can be grafted at the extremity of the SNOM tip to enhance the electric or magnetic spontaneous decay rate of quantum emitters [60, 61]. Quantum emitters can also be utilized as tip-based quantum sources of light [62]. In fact, research toward the realization of quantum photonics systems requires the precise positioning of quantum emitters as single-photon sources [63]. The spin-orbit interaction of light was reported using the emission from the aperture tip with left or right handed circular polarization to control the directional mode propagation in a photonic crystal waveguide [64].

Figure 1.2(b) shows the collection-mode SNOM, which was used shortly after the realization of the illumination-mode SNOM to image beyond the diffraction limit in the near-field. In the collection-mode SNOM, light is often focused on the sample through an objective, and the aperture tip maps the near-field distribution over a sample. SPP modes in plasmonic interfaces, waveguides, or nanostructures have been mapped using the aperture SNOM [65–71]. The development of 2D photonic crystals is also owed to SNOM measurements. Near-field measurements of the electric and magnetic field distribution near photonic crystal cavities and waveguides

have been carried out with the collection-mode SNOM [72–74]. Furthermore, it was demonstrated that the presence of a SNOM tip shifts the resonance wavelength of high-quality factor photonic crystal microcavities, and it can tune the resonance wavelength in photonic crystal cavities [75–77]. The collection mode also provides direct access to the near field of complex or disordered dielectric media. In this regard, the role of correlated disorders in the enhancement of light-matter interaction has been investigated [78, 79].

Figure 1.2(c) demonstrates the illumination-collection SNOM where the excitation and detection are carried out through a single tip. When it comes to investigating quantum emitters integrated into nanophotonic systems, the illumination-collection mode is the main used SNOM configuration. In the illumination-collection mode, light typically illuminates a sample through an uncoated tip, and the scattered photoluminescence signal from quantum emitters reaches the detector through the same fiber tip. SNOM with just a single tip has enabled the spectral measurement in the near field of quantum emitters embedded in photonic crystal cavities [80, 81]. Typically, an uncoated fiber tip is used to excite and detect the evanescent light through the same fiber to measure the spectral dependence of the LDOS. The imaginary and real part of the electric and magnetic mode volume of photonic crystal nanocavities were also measured using SNOM operating in the illumination-collection mode [82, 83]. Similarly, illumination-collection SNOM has mapped the Anderson localization and speckle pattern in the near field of disordered photonic crystals where light interference leads to a random mode confinement with a small spatial extent [84, 85]. While the illumination-collection mode of SNOM is a proper technique to measure the spectral dependence of LDOS, the spatial measurement of LDOS using this technique leads to low resolution because of the scattered light, which is collected not only from the sharp end of the tip but also through the shaft of the fiber tip. Thus, it is not feasible to map the spatial extent of the excited modes at a particular position with a single tip in illumination-collection mode.

The spatial extend of excited modes in complex structured media is described by the spatial correlation function due to the near-field distribution of the excited modes [86]. Near-field spatial correlation functions of a random medium are governed by the imaginary part of the dyadic Green's function [79]. The dyadic Green's function describes the near-field response of any photonic system to an electric or magnetic dipolar source. In complex and random photonic systems such as random lasers, light undergoes multiple scattering resulting in localized modes or modes with the

limited spatial extent [87]. The cross density of states (CDOS) accounts for the spatial coherence between the point source dipole and the point of interest in random or disordered nanostructures and is obtained from the imaginary part of the Green's function [87–89]. LDOS is also defined mathematically as the imaginary part of the dyadic Green's function [42]. If the dyadic Green's function of a photonic system is known, one can calculate the electromagnetic field components for any arbitrary current distribution. Nevertheless, the amplitude and phase of the electromagnetic near-field components should be known with a high spatial resolution to construct Green's function of nanophotonic systems. While microwave measurements of the Green's function have been recently reported [90], the measurement for the visible and near-infrared spectrum has not been addressed yet. Thus, introducing a technique that enables the dyadic Green's function measurement, can provide powerful means to understand the underlying physics of optical phenomena in complex and random photonic systems.

The dual-tip SNOM is a promising instrument that potentially can measure the dyadic Green function of the photonic systems in visible and near-infrared spectra. The dual-tip SNOM using two aperture tips provides both point source excitation and point detection below the diffraction limit (Fig. 1.2(d)). In perspective, the integration of phase-sensitive measurement into the dual-tip SNOM setup would even allow full vectorial measurements of all electromagnetic field components in the near-field [91]. Despite it's versatility, the dual-tip SNOM rarely has been used due to the complexity of the operation and interpretation of the mapped data. The idea of using two SNOMs for near-field measurements was first introduced by Dallapicola et al. to measure the propagation length of surface plasmon polaritons (SPPs) on a gold waveguide [92]. Since then, the dual-tip SNOM has been utilized mostly for plasmonic studies, including mapping the near-field interference pattern of SPPs on a ring-shaped groove [93], the characterization of SPPs modes in plasmonic waveguides [94] and nanowires [95]. The effect of the excitation tip position on the strength of the excited modes in a multi-mode plasmonic waveguide was explored by excitation and detection in the near field [96]. Moreover, it was dual-tip SNOM that allowed for the first time mapping of a dipolar emission from the aperture tip through the near-field of SPPs on a gold film [48]. In the most recent study the dual-tip SNOM measured the temporal waveform of an ultrafast SPP pulse propagation on a gold film [97]. Apart from the characterization of plasmonic structures, the dual-tip SNOM visualized the local carrier dynamics in a single quantum well [98, 99]. In an

ideal dual-tip SNOM, the excitation tip illuminates a desired area of a sample. The detection tip automatically scans the entire area around the excitation tip and maps the optical near field while avoiding any collision with the excitation tip. Principles of a collision prevention scheme to control a distance between the excitation and detection tip has already been demonstrated in our group [100]. In this regard, the dual-tip SNOM was used to measure a dipolar emission from an aperture tip, and the near field distribution of SPP modes in plasmonic waveguides [101]. However, a user intervention was essential for all near-field measurements to prevent the collision of two tips. Moreover, to obtain a near-field map of the entire area around the excitation tip, several configurations of two tips relative to each other were essential. In other words, several scans were required to obtain a single map of the near-field optical information around the excitation tip [48].

This thesis presents the first realization of a fully automated dual-tip SNOM, which overcomes the limitations of previous techniques and unleashes the capabilities of the dual-tip SNOM to measure the near-field of plasmonic and dielectric nanostructures. The thesis is structured as follows: Chapter 2 describes the instrumentation and optical setup of the first fully automated dual-tip SNOM. Implementing a collision prevention scheme for automating dual-tip SNOM measurements, utilizing a digital SNOM controller, is thoroughly explained. The scan parameters particular to automated dual-tip SNOM are introduced. In Chapter 3, the stability and robustness of the automated dual-tip SNOM for different scan parameters are discussed. Moreover, the feasibility of automated scans for the combination of different scanning probes is investigated. Chapter 4 is devoted to characterizing the emission from excitation aperture tips through the near-field pattern of SPPs at an air-gold interface. Polarization of the dipolar emission from an aperture tip was explored. Three pairs of excitation and detection tips were employed to compare the mapped near-field patterns showing different dipolar emission. We observed the first directional SPPs pattern excited by a emission from the aperture tip. Chapter 5 is dedicated to investigating a dipolar emission from the excitation tip on the edge of a hexagon-like gold platelet. The image dipole method was employed to analytically calculate the measured near-field interference pattern of the SPPs. The results of both analytical calculation and numerical simulation are discussed. In Chapter 6, the dipolar emission from the excitation tip is investigated near a silicon nanodisk metasurface. We have observed the spatial and spectral dependence of the measured near-field patterns corresponding to different excitation wavelengths as well as different excitation

positions relative to the metasurface. A relation between the integrated near-field intensity over the scan area and the normalized power radiated by a classical dipole at the same position of the excitation tip is explored.

2

Fully automated dual-tip SNOM

Dual-tip scanning probe microscopes (SPMs), such as scanning tunneling microscope (STM) and scanning atomic force microscope (AFM), have already been proven as essential instruments for nanomaterial characterization and manipulation [102, 103]. To this end, a single-tip SNOM was utilized in combination with other scanning tip microscopes, e.g., atomic force and scanning electron microscopes (SEM) [104]. Despite the capability of the dual-tip SNOM to excite and detect simultaneously below the diffraction limit, only a few dual-tip SNOM measurements at visible wavelength have been reported so far [48, 92, 93, 95, 96]. The reasons originate from technical challenges that should be addressed for robust dual-tip SNOM measurements. Robust measurements require distance control between the excitation and detection tip. Since the first demonstration of dual-tip SNOM, the collision between two tips has been the main impeding factor for its further development.

Different approaches have been employed to reduce the tips' collision and damage during scans. In the first measurement by the dual-tip SNOM configuration to prevent the collision between the two tips, a user manually stopped the detection tip once the excitation tip appeared in the mapped topography [92]. However, the manual stop of the detection tip using the topography image increases the chance of damage between the excitation and detection tip. Moreover, a sample containing features with different height might cause a misinterpretation and early stop of the detection tip. Above all, the forced stop of the detection tip does not allow a complete scan of the area around the excitation tip. Another scheme to control the distance between two tips is based on the mechanical interaction of tuning forks as weakly coupled oscillators [100]. A fiber aperture tip is glued to one prong of a tuning fork while another prong is fixed to the cantilever as it is shown in Fig. 2.1. The oscillation of the tuning forks results

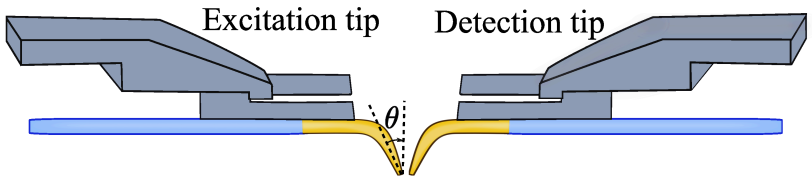

Figure 2.1: Dual-tip SNOM configuration. Two bent fiber tips attached to the tuning forks positioned in proximity of each other. The tapered region of fiber tips makes the angle θ relative to the surface normal.

in mechanical coupling between the excitation and detection tip when they laterally approach. In the proposed collision prevention scheme, the mechanical coupling was used as a signature of the tips' proximity [100]. Thus, a lock-in amplifier (LIA) was used to demodulate the oscillation amplitude of one tuning fork at the resonance frequency of the other. An abrupt increase of the LIA output is a sign for users to stop the detection tip before the excitation tip appears in a topography image. Nevertheless, the user intervention is still required. Furthermore, reconfiguration of the detection tip enables scanning from left or right toward the excitation tip covering a larger scan area around the excitation tip [48]. On the other hand, at least three scans with different dual-tip configurations were necessary to build one near-field image, which is cumbersome in practice. These challenges must be addressed to establish the dual-tip SNOM as a standard near-field microscopy technique. In the ideal dual-tip SNOM, the detection tip should automatically map the optical near-field around the excitation tip just with one scan without user intervention to stop the scan or change the position of a detection tip.

To automate the dual-tip SNOM, the first step is to enhance the overall signal-to-noise ratio (SNR) related to electronics and the controller of the setup. In doing so, we replaced controllers and electronics of two SNOMs connected with many cables, with a fully digital SPM controller capable of controlling both SNOMs concurrently (R9, RHK Technology, Troy, Michigan, USA). The full integration, removing unnecessary interconnecting cables, leads to reduction of the overall electronic noise of the system. Furthermore, all electronics and hardware inside the controller are software configurable and in one housing. The digital controller converts analog oscillation amplitude signals from excitation and detection tips immediately to digital signals before any further process. The early conversion of analog signals to digital signals makes the oscillation amplitude signals immune to external noises and electronic crosstalk, critical factors in automating the dual-tip SNOM.

Moreover, all input signals are processed simultaneously by a field-programmable

gate array (FPGA). The FPGA enables a fast response of the controller and facilitates the implementation of the automated scan. In a fully automated dual-tip SNOM, the excitation tip is stationary, and the detection tip automatically maps the near-field optical information around the excitation tip without any collision with the excitation tip.

This chapter presents the first fully automated dual-tip SNOM, which works in both visible and near-infrared wavelengths and is also capable of measuring structured photonic systems. In Section 2.1, the optical setup and electronics of the automated dual-tip SNOM are explained. The implementation of the collision prevention scheme is presented in Section 2.2. In Section 2.3, I define the parameters which are specific to the dual-tip SNOM and are essential to understand acquired images by the setup. The last section of this chapter highlights the capability of the dual-tip SNOM to robustly measure the near-field of a silicon nanodisk metasurface as a nanostructured sample.

2.1 Optical setup and electronics for automated dual-tip SNOM

Aperture tips (Nanonics Imaging Ltd) are the key components in the dual-tip SNOM setup. In their fabrication process, first, the optical fiber is heated and pulled to form a tapered region with a conical shape. Then, a fiber bend is imposed by an infrared laser leading to the bent angle of 120°. In other words, the fiber tip makes the angle $\theta = 30°$ with the surface normal (Fig.2.1). A chromium adhesion layer and then 200-300 nm of evaporated gold coats the tapered region of the fiber while a subwavelength aperture at the tip apex is left uncoated. The gold coating thickness is larger than its skin depth to prevent light leakage before reaching the aperture exit. In the final step, the fiber aperture tip is glued to one prong of a tuning fork allowing the fiber to oscillate with the same resonance frequency as the tuning fork. Another prong of the tuning fork, however, is glued to a cantilever. The tuning fork is required to adjust the fiber tip height during the scan.

The cantilever is mounted on a SNOM scanning head (MV-4000, Nanonics Imaging Ltd). Each SNOM head comprises a stepper motor inside the housing and a flat piezoelectric scanner where the cantilever is mounted. The stepper motor is used to move the tip coarsely along the xyz axes before scans. For fine lateral and vertical displacements of the tip, the flat piezoelectric scanner is utilized. The coarse positioning of the sample on a custom-designed stage is performed by a piezo slip-stick positioner (Smaract SL-17). In addition, a subnanometer sample displacement relative to the

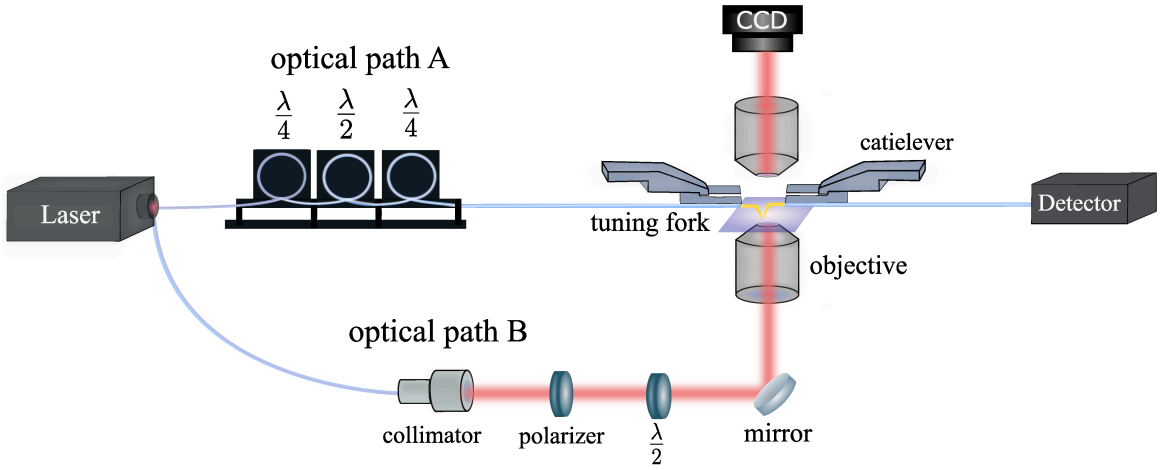

Figure 2.2: The dual-tip SNOM optical setup. The optical path A with the polarization controller to manipulate the polarization of the beam coupled to the excitation fiber tip. The optical path B is used for far-field excitation when just a single tip is used for near-field measurements in the collection mode.

excitation tip is carried out by a closed-looped piezo stage (PI 542.2). Nonetheless, a mechanical and thermal drift of the excitation and detection scan heads during lengthy measurements is inevitable with current conditions of the setup.

The optical setup of the dual-tip SNOM is composed of two optical microscopes. The upright microscope (Zeiss AxioScope A1) enables observation from above and has manual translation to displace the microscope along x, y, and z. Additionally, an inverted optical microscope (Zeiss AxioObserver D1) allows observation and laser coupling from beneath the sample. The upright microscope is equipped with a charge-coupled device (CCD) camera to provide a live image of the sample and the aperture tips. For measurements in the visible or near-infrared, the objective and camera are adapted to the used wavelength. A light-emitting diode (LED) of the upper microscope is replaced with a quartz tungsten halogen lamp covering both visible and near-infrared wavelengths. The light sources for illumination through excitation tip are continuous wave (CW) lasers. A single wavelength HeNe laser, coupled to the end of the excitation tip's fiber, is used for the sample illumination at wavelength $\lambda = 633$ nm. A near-infrared laser that can be tuned between $\lambda = 1490 - 1650$ nm (Tunics Reference, Anritsu), can be utilized for near-field measurements within the near-infrared spectrum. Consequently, two single-photon detectors that are sensitive to visible wavelengths (PerkinElmer SPCM-AQR) and near-infrared wavelengths (ID Quantique ID220) are employed for visible and near-infrared measurements.

Figure 2.2 illustrates two different optical paths which are used in dual-tip SNOM

measurements and collection mode measurements with a single tip. In the optical path A, a fiber polarization controller connected to the excitation tip alters the polarization of the light couples to the excitation aperture tip. For using the single tip SNOM for the collection mode in the visible or near-infrared spectrum, the necessary optics are adapted to the corresponding wavelengths in optical path B (Fig. 2.2,) consisting of a polarizer and half-wave plate to rotate the polarization of an incident beam for the far-field illumination.

Before starting near-field measurements, the stepper motors displace the excitation and detection tip until they are within the camera's field of view. The slip-stick positioner displaces the sample so that both tips and the desired area of the sample can be observed by the camera. A smaller aperture with a shorter distance from the sample surface results in a higher resolution near-field map. However, there is always a compromise between the transmission and the resolution of aperture tips. The larger aperture with higher transmission efficiency leads to the near-field optical image with lower spatial resolution [105]. Hence, the diameter of the aperture can not be reduced arbitrarily. The transmission is especially important in the dual-tip SNOM, where the transmitted light through the aperture of the excitation tip is scattered from the sample and is coupled to the fiber by means of a subwavelength aperture of the detection tip. The power of the scattered light coupling to the detection tip when reaching the detector is $10^{-9} - 10^{-12}$ of the input laser power coupled to the excitation tip [101].

2.2 Working principle of the automated dual-tip SNOM

Figure 2.3 shows the schematic of electronics in the dual-tip SNOM setup. The z feedback loops control the displacement of SNOM tips toward the sample. To do so, the controller applies sinusoidal voltages to piezoelectric tuning forks at their fundamental resonance frequencies. The fundamental resonance frequencies of the tuning forks are in a frequency range between 32-45 kHz. The excitation and detection tips oscillate with the fundamental resonance frequencies f_e and f_d, respectively. Each tuning fork with the fiber tip oscillates with an amplitude proportional to the amplitude of the applied voltage. The tuning forks and fiber tips oscillate vertically in the tapping mode in which the oscillation amplitudes of the tips are large compared to the range of the effective forces originating from the sample surface [106]. When the electrical voltage is applied, it induces mechanical oscillations to the piezoelectric tuning forks leading to oscillating charges measured as an electric current by

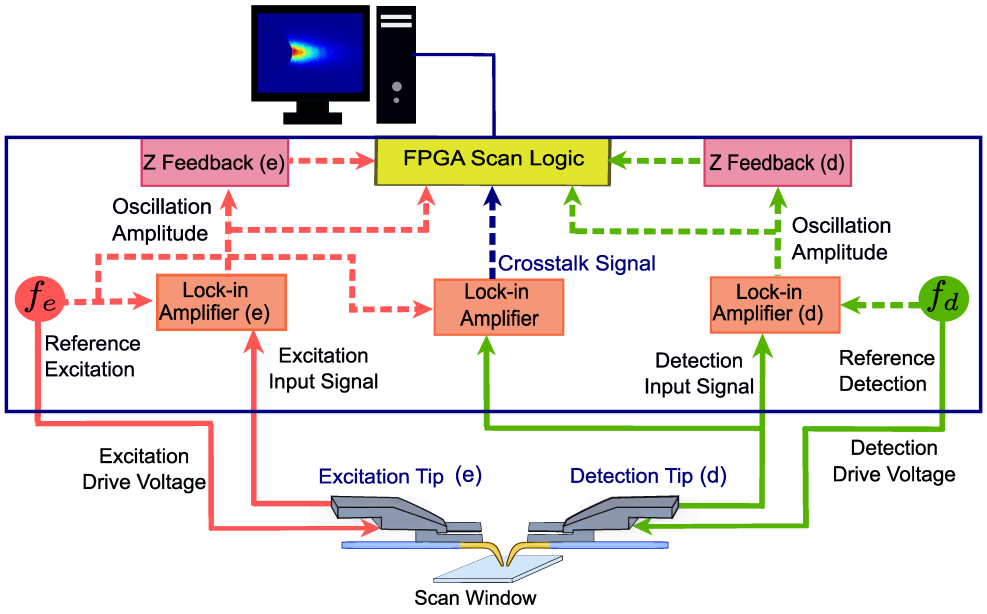

Figure 2.3: Schematics of control electronics for the automated dual-tip SNOM. The signal from the detection tip is associated with green color and red color is linked to the signal from the excitation tip. Dashed lines represent purely digital signals.

the controller. The transimpedance amplifier converts the current to a voltage. The controller digitizes the voltage before an internally integrated digital lock-in amplifier demodulates it. The digitized voltage from each tip is sent to the corresponding LIA. Two LIAs demodulate the signal from the tuning forks at their respective resonance frequency. The ultra-ADC, which converts the analog signal of tuning fork's oscillation amplitude to digital signal, can regenerate the voltage signal with the highest accuracy. During the approach of the oscillating tip attached to the tuning fork toward the sample, the oscillation amplitude is continuously compared to the setpoint value of the Z feedback loop to control the tip's safe approach. The corresponding setpoint is determined according to the oscillation amplitude of the excitation and detection tip when they are far from the sample. The setpoint is usually set to 90% of an unperturbed oscillation amplitude. Within the optical near-field region, the tip oscillation is perturbed by the normal forces from the sample surface. As a result, the oscillation amplitude drops, and once it meets the setpoint, the controller stops the tip's approach toward the sample. For the rest of the measurement, the height of the excitation and detection tip is adjusted with the respective Z feedback loop.

The excitation tip is typically placed at the desired position of the sample within the scan window, i.e., the area where the scan is carried out. The detection tip scans the sample pixel by pixel within the scan window. The time per pixel for the

detection tip is typically set to 20 ms. One can increase the integration time in the controller's software by increasing the time that the detection tip spends at each pixel to acquire the near-field signal. However, the cost that must be paid for increasing the integration time is a longer scan.

The FPGA simultaneously processes the digital data from different components inside the controller to improve the system's response time when tips are coupled mechanically. The dual-tip SNOM requires a third LIA to implement the automated scan. The output signal of this LIA is called "crosstalk" signal. The crosstalk signal is the oscillation amplitude of the detection tip demodulated at the resonance frequency of the excitation tip. When two tips are far from each other, the crosstalk signal is at the noise level and is called "base crosstalk signal," which depends on the oscillation amplitudes of the excitation and detection tips. During the scan, each tuning fork oscillation increases air perturbation, which acts as an external force on the other tuning fork giving rise to their weak coupling [100]. When the detection tip approaches the excitation tip, a smooth increase of the base crosstalk signal is observed [107]. Once the detection tip is within the shear forces region of the excitation tip, their mechanical interaction is much stronger, and the crosstalk signal increases significantly. The sudden increase of the crosstalk signal indicates that the further scan of the detection tip must be avoided. Therefore, the crosstalk signal is a reliable indicator for implementing the automated dual-tip SNOM [100].

We introduced a function in the controller's software to enable the automated scan. The function's input is the predefined threshold value that is set according to the base crosstalk signal. The detection tip stops scanning when the crosstalk signal exceeds the threshold value. The detection tip scan is typically performed with a time per pixel of 20 ms. Once the crosstalk signal exceeds the threshold, the remaining pixels of the scan line is filled with a very short time per pixel of 2 µs. Finally, the detection tip sweeps back and continues scanning the next line. A parabolic-like region of irrelevant data is built up due to the presence of the excitation tip within the scan window. This region is called "avoidance area". All acquired signals (topography, optical, crosstalk and etc.) within the avoidance area are meaningless and they are needed only to meet the conditional scan logic of the program. Thus, during image processing the pixels within the avoidance area are set to zero.

Figures 2.4(a) and (b) illustrate the schematics and the corresponding topography signal on a gold film for scan directions along the x axis and y axes. In Fig. 2.4(a), the detection tip scanned the sample along the x axis. The start point of the scan

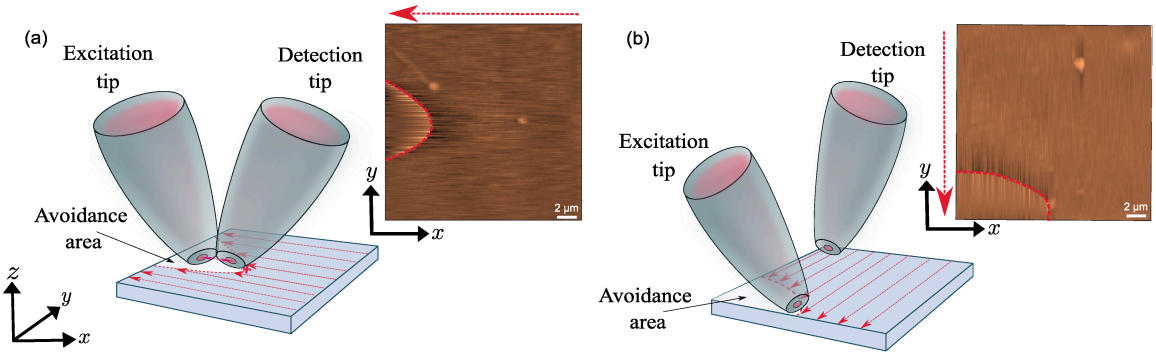

Figure 2.4: Schematics of the dual-tip SNOM for the scan directions along the (a) x and (b) y axes. The corresponding topography images on a gold film are shown next to the schematics. The red dashed arrows denote the direction and position where the detection tip starts scanning. The red dashed parabolic curve denotes the boundary of the respective avoidance area in both schematics and map topographies.

is the start point of the red arrow in both schematic and topography map. Since the detection tip scans from the opposite direction of the excitation tip, it can map the whole area around the excitation tip. The boundary of the avoidance area is highlighted by the red dashed parabolic curve. In Fig. 2.4(b) the detection tip approaches the excitation tip from the side along the y axis. As a result, the avoidance area no longer shows a parabolic shape, and the detection scan cannot map the near-field on the other side of the excitation tip. Selecting the scan direction depends on the position of the desired area on the sample relative to the excitation tip.

The well-defined boundaries of the avoidance area approved the robustness of the measurements by the automated dual-tip SNOM [99].

More factors have been taken into consideration to realize the fully automated and robust dual-tip SNOM when compared with the first attempt to automate a dual-tip SNOM [99]. Kaneta et al, utilized excitation and detection tips with the same resonance frequency 32.7 kHz, oscillating parallel to the sample. In their technique to control the distance between the two tips an extra oscillation frequency was required to implement the heterodyne technique. The extra oscillation frequency of 100 Hz that was applied to the detection tip gave rise to an additional oscillation parallel to the sample and perpendicular to the direction of the detection tips' resonance oscillation. However, a relatively large oscillation amplitude limited the resolution of acquired images. In other words, the tip covered a larger area due to the additional motion; therefore, the pixel size was larger. Moreover, tips' distance from a sample was considered to be constant during scans which in turn limited their technique only to flat surfaces. However, as it was seen in the automated dual-tip SNOM there

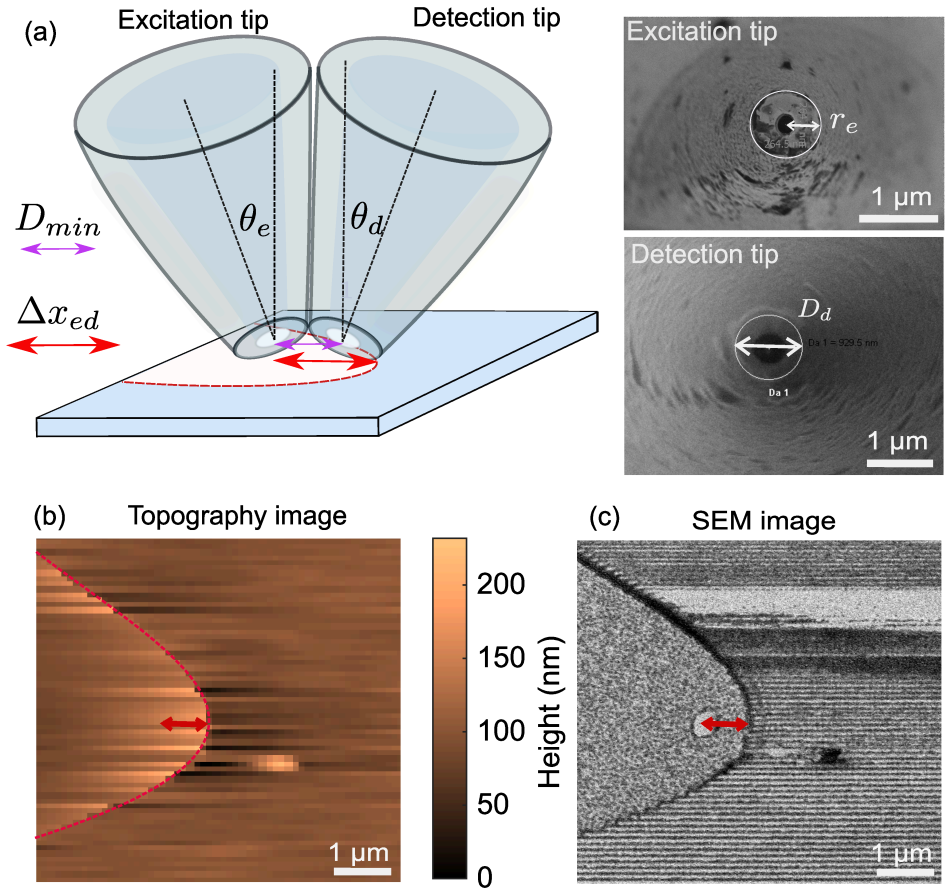

Figure 2.5: Automated dual-tip SNOM configuration (a) Schematic of the excitation and detection tips at the minimum distance from each other. The white parabolic region is the avoidance area, and the red dashed curve indicates its boundary. θ_e and θ_d are the angles that excitation and detection tips make with the surface normal, respectively. The red double-sided arrow corresponds to Δx_{ed}, a distance from the outer edge of the detection tip to the center of the excitation tip's aperture. The purple double arrow D_{min} is the minimum distance between the center of the excitation and detection tips' apertures. SEM images of the excitation and detection tips used in the mapped topography in (b). (b) Topography map of a gold film with a photoresist on top. (c) The SEM image of the mapped topography in (b). The boundary of the avoidance area is evident in the SEM image. The hole within the avoidance area denotes the illumination spot size.

is no need for an extra oscillation frequency, and the fundamental frequency of the tips is used to implement the automated collision prevention scheme. The resonance frequency of the tips (30-45 kHz) leads to almost 300 times faster detection speed of the lock-in amplifier when compared with a demodulation signal with oscillation frequency of 100 Hz. Furthermore, demodulation of low-frequency signals is more susceptible to electronic and vibrational noise interference, which negatively affects the distance control between the two tips and the overall stability of the scan. The

speed of data processing is another important factor in realizing the robust automated dual-tip SNOM, which is only feasible by using the fully digital controller. The digital controller in our setup can be set up at 50-100 µs intervals to check if the crosstalk signal exceeds the threshold value.

2.3 Minimum distance and relative position of two tips

The exact coordinate position of the excitation tip's aperture over a sample is required to analyze and interpret the results of the dual-tip SNOM measurements. To this end, the SEM images of the excitation and detection tips have to be taken before the dual-tip SNOM measurements. SEM images provide geometry information such as the diameter of the aperture, the diameter of the tip apex, the thickness of the aperture rim, and the bend angle of the tip. Fig. 2.5(a) shows the schematics of two tips when they are at minimum distance from each other and the SEM images of the excitation and detection tips that were taken after a topography measurement in Fig. 2.5(c)

In Fig. 2.5(a), the center position of the excitation tip's aperture on the sample is determined by the displacement Δx_{ed} (equal to a double red arrow) from the vertex of the avoidance area toward the negative x direction. Δx_{ed} is measured as a distance from the outer edge of the detection tip to the center of the excitation tip that can be calculated using the SEM images. Since the avoidance area has a parabolic shape, it implies that the distance between the two apertures' centers varies during the scan. In other words, the last obtained pixel at a boundary of the avoidance area, is mapped at different distances from the excitation tip's position. The shortest distance of Δx_{ed} occurs when the detection tip scans the line across the vertex of the avoidance area. The double purple arrow in Fig. 2.5(a) denotes the minimum length D_{min} between the center of the two apertures Δx_{ed} and D_{min} are calculated by the following expressions,

$$\Delta x_{ed} = D_d \cos\theta_d + r_e \cos\theta_e, \tag{2.1}$$

$$D_{min} = r_d \cos\theta_d + r_e \cos\theta_e, \tag{2.2}$$

Here r_e and r_d are the radius of excitation and detection aperture tip from the edge of the apex to the center of the aperture. The diameter of the detection tip's apex is $D_d = 2r_d$. The tilt of the detection and excitation tip relative to the surface normal is θ_e and θ_d (See Fig. 2.5(a)). These angles varies between $15° < \theta_e, \theta_d < 30°$ corresponding to $0.86 < \cos\theta_e, \cos\theta_d < 0.96$. To validate the accuracy of the value $\Delta x_{ed}(Eq.2.1)$ calculated by geometry parameters of the tips, the SEM image of the

sample was used to measure Δx_{ed} . For this purpose, the detection tip was scanned a gold film covered with 3-5 nm photoresist. Figure 2.5(b) is the corresponding mapped topography image in which the red-dashed curve denotes the boundary of the avoidance area. After the dual-tip SNOM measurement the SEM image of the scanned area on the gold film was taken. Figure 2.5(c) shows the SEM image of the mapped area of the gold film in Fig. 2.5(b). When the excitation tip illuminates the gold film at $\lambda = 1550$ nm, it creates a hole in the photoresist equal to the size of the aperture projection on the surface. Moreover, the relatively thin photoresist was removed by the detection tip oscillating with a large amplitude in the tapping mode. The boundary of the avoidance area is therefore easily discernible in the SEM image.

In Fig. 2.5(c), $\Delta x_{ed} = 650$ nm (red double arrow) is measured as the distance from the apex of the avoidance area's vertex to the center of the hole. On the other hand, the calculated value of $\Delta x_{ed} = 610$ nm is obtained from Eq. (2.2) using the measured geometry data. The small difference between the measured and calculated value is attributed to the change of tilt angles when tips are mounted on cantilevers. Nevertheless, calculations of Δx_{ed} from measured geometry data provides a sufficiently accurate value to find the position of the excitation tip on the sample and the minimum distance D_{min} between the centers of the two tips' apertures.

2.4 Near-field measurements of nanostructured samples

Thus far, the dual-tip SNOM measurements were reported only for flat and unstructured samples. However, most photonic systems feature nanostructures. Hence, I investigated the applicability of the automated dual-tip SNOM for nanostructured samples. In this regard, a dielectric metasurface with nanodisk arrays was measured using the automated dual-tip SNOM. Aside from the topography and optical signals, phase, amplitude, and crosstalk signals were also obtained simultaneously during the scan.

In Fig. 2.6, measured signals are shown for the topography of the silicon nanodisk metasurface, the oscillation amplitude of the detection tip, the oscillation phase of the detection tip, the near-field intensity, and the crosstalk signal. The excitation tip illuminated the metasurface at wavelength $\lambda = 1.62$ µm. The well-defined boundary of the avoidance area in all mapped signals shows the stability and robustness of the collision prevention scheme on a metasurface as an example of a structured sample. Furthermore, the topography, phase, and amplitude signals provide a good approximation of the position of the nanodisks. The blunt apex of the detection tip

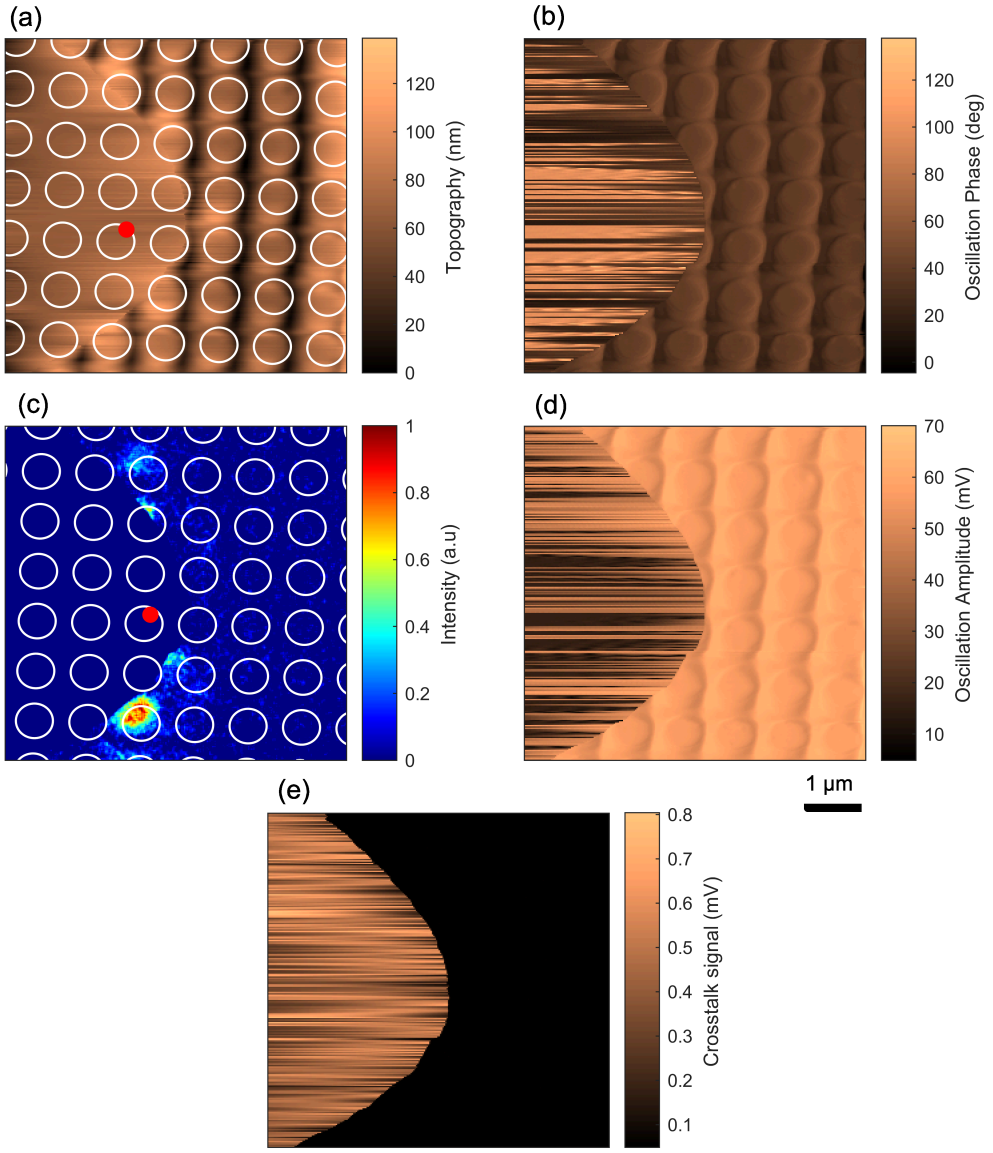

Figure 2.6: Maps of (a) the silicon metasurface topography (b) the oscillation phase of the detection tip (c) the near-field intensity (d) the oscillation amplitude of the detection tip (e) the crosstalk signal. White circles denote the position of the nanodisks. The red dot indicates the position of the aperture.

mapped the topography, which is the convolution of its apex and the nanodisks [108]. Thus, the mapped topography does not represent the diameter and position of the nanodisk's edge accurately. However, in the mapped oscillation phase of the detection tip (Fig. 2.6(b)), the edges of the nanodisks are sharper compared to the topography and amplitude maps. The sharp edges are due to the oscillation phase being sensitive to changes in height and the different types of materials used in the fabrication of the metasurface, which are silicon nanodisks on a glass substrate. As a result, the

mapped phase is a better indicator to find the position of nanodisks. Furthermore, the outer edge of the detection tip's apex is the point of contact with the sample as long as the tip is bent. Thus, a pixel where the optical signal is collected is offset by $r_d \cos\theta_d$ from a pixel where a corresponding topography signal is mapped. This offset is about 350 nm for the detection tip used in Fig. 2.6. The position of the nanodisks in the near-field intensity map (Fig. 2.6 (d)) is therefore determined by applying the offset along the positive x-direction to the positions of the nanodisks in the mapped phase in Fig. 2.6(b). Hence, maps of the topography, phase, and amplitude signals can be used to find the feature's position in the nanostructured sample.

In Fig. 2.6(e) the base cross talk signal is almost constant until it reaches the avoidance area. The avoidance areas of the different signals, as it was pointed out, contain no meaningful data. It it worth mentioning that artifacts presented in mapped images by AFM [108] or single aperture SNOM [109] could also appear in the topography and the near field intensity measured using the dual-tip SNOM and should be taken into account during image processing.

The measurements stability of the dual-tip SNOM is determined by some parameters that are set in the controller before near-field measurements. It is crucial to optimize these parameters to ensure robust measurements. In Chapter 3, I will investigate the parameters of the SNOM controller that influence the robustness of the automated dual-tip SNOM measurements. All the measurements in this thesis have been carried out using the automated dual-tip SNOM. Only in Section 6.2 the collection mode SNOM will be employed to map the near-field intensity of metasurfaces excited from the far field.

3 Automated dual-tip SNOM stability assessment

Reliable and reproducible near-field measurements using the automated dual-tip SNOM require the robust performance of the setup. In addition to low-noise electronics, some parameters related to the automated scan procedure must be optimized to achieve robust measurements. For automated scanning, the most important parameter to be optimized is crosstalk signal.

In this chapter, the parameters that determine the stability of the automated dual-tip SNOM are investigated. Section 3.1 describes the mathematical model for tuning forks as weakly coupled oscillators to find out the parameters related to the crosstalk signal. We will observe that the oscillation amplitude of the excitation tip and the avoidance threshold are two crucial parameters that must be optimized before performing the measurements. In Section 3.2 the stability of the automated scan by changing the oscillation amplitudes of the excitation tip are explored. The effect of varying the avoidance threshold on a robust measurement is presented in Section 3.3. In Section 3.4, the possibility to apply a collision prevention scheme for combinations of different excitation and detection tips is discussed [1].

3.1 Tuning forks as weakly coupled osicllators

A mathematical description of the crosstalk signal can be obtained when the excitation and detection tuning forks are viewed as weakly coupled oscillators [100]. Only the fundamental resonance frequencies f_e and f_d of the tuning forks are used to implement the automated collision prevention scheme. Thus, the respective deflection of the excitation and detection tuning forks, x_e, x_d is described by the following equations

[1] Parts of the results of this chapter have been published in reference [107].

[100],

$$\ddot{x}_d + 2\Gamma_d \dot{x}_d + \omega_d^2 x_d + \sigma_{ed} x_e = F_d e^{i\omega_d t}, \tag{3.1}$$

$$\ddot{x}_e + 2\Gamma_e \dot{x}_e + \omega_e^2 x_e + \sigma_{ed} x_d = F_e e^{i\omega_e t}, \tag{3.2}$$

where Γ_d and Γ_e are damping constants, and ω_e and ω_d are (angular) eigenfrequencies of excitation and detection tuning forks, respectively. The coupling constant between the excitation and detection tips' tuning forks is σ_{ed}. The amplitudes of the external driving forces applied to the detection and excitation tuning forks are F_d and F_e, respectively. We can solve the system of the two coupled resonators by the ansatz

$$x_d = Be^{i\omega_e t} + Ce^{i\omega_d t}, \tag{3.3}$$

$$x_e = De^{i\omega_e t} + Ee^{i\omega_d t}, \tag{3.4}$$

where B and C are oscillation amplitudes of the detection tuning fork at the angular frequencies ω_e and ω_d, respectively. Likewise, D and E are the oscillation amplitudes of the excitation tuning fork at the angular frequencies ω_e and ω_d. In the collision prevention scheme, the crosstalk signal A_{CT} measured by the lock-in amplifier is proportional to the oscillation amplitude B of the detection tip at the resonance frequency f_e of the excitation tip. Hence, a mathematical expression for the crosstalk signal is achieved,

$$A_{CT} \approx B \approx \left| \frac{\sigma_{ed} D}{2\Gamma_e \omega_e} \right|. \tag{3.5}$$

Equation 3.5 implies that the increase of the crosstalk signal is proportional to the oscillation amplitude D of the excitation tip at resonance frequency f_e. As a result, the effect of changing the oscillation amplitudes of the excitation tip on the crosstalk signal A_{CT} and, in turn, on the measurements robustness should be investigated. In doing so, the parameters of the LIA should be optimized, since they influence the speed and accuracy of the LIA to recover a desired weak signal from high background noise. As long as, the fundamental frequencies of the tips are close, correctly set LIA parameters is critical for robust measurements.

For the low-pass filter of the LIA, the roll-off rate (i.e., the steepness of the transition between the pass-band and stop-band of the low pass filter) and the bandwidth should be set properly according to the resonance frequency of the excitation and detection tips. In the controller, the maximum value of 48 dB/oct for the roll-off and a bandwidth between 10 mHz to 100 kHz can be selected to optimize the response time of the LIA. Finding the optimal value of the filter roll-off and the bandwidth is challenging when a difference between the oscillation frequency of a reference signal

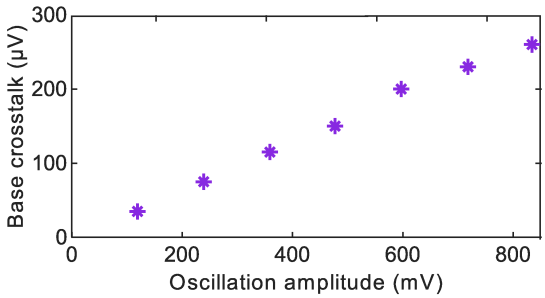

Figure 3.1: Base crosstalk signal as a function of the oscillation amplitudes of the excitation tip.

and the oscillation frequency of the LIA input signal is less than 1 kHz. For instance, for the resonance frequency of the excitation and detection tip $f_e = 34.96$ khz and $f_d = 40.52$ kHz, the low-pass filter was set to the roll-off 30 dB/oct and bandwidth of 200 Hz. During the stability assessment, these paramteres were set for the low-pass filter and did not change during the entire measurements.

3.2 Investigation of the oscillation amplitude of the excitation tip

In this section, the effect of changing the oscillation amplitude of the excitation tip on the robustness of the measurements will be discussed. For the stability investigation of the dual-tip SNOM measurements, a flat silicon wafer with an almost defect-free surface was used as a sample. The excitation tip was driven by a voltage of $10 - 70$ V with the step of 10 V, led to oscillation amplitudes of the excitation tip between 120 mV $< D <$ 860 mV. It is important to note that the electrical readout of the software is in volts; thus, a unit of volt was used to describe the strength of the oscillation amplitude of the excitation and detection tip. Each time the detection tip scanned the same area of 10×10 µm^2 on the silicon surface. The oscillation amplitude of the detection tip $C = 280$ mV was kept constant during entire measurements. It should be pointed out that the oscillation amplitude of the detection tip should be chosen according to the properties of the sample under investigation to prevent any damage to the sample surface or to the detection tip. The standard deviation of height was calculated for the mapped topographies in order to investigate the instability of the automated detection tip. Since the surface of the sample was flat, any significant variation of the standard deviation is attributed to the instability of the automated dual-tip SNOM at the corresponding oscillation amplitude. Increasing the oscillation amplitude of excitation or detection tip leads to the increase of a base crosstalk signal

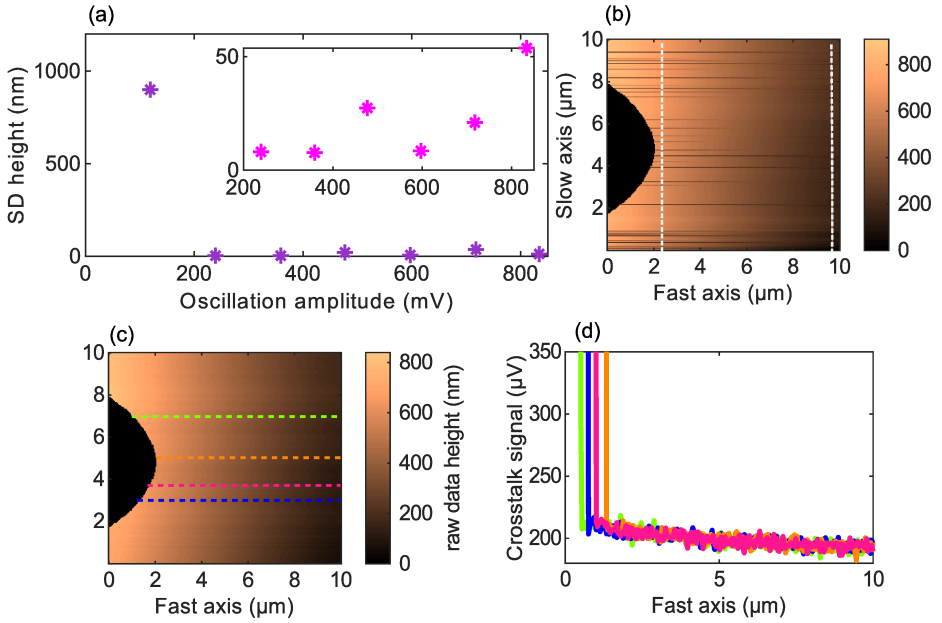

Figure 3.2: (a) Standard deviation (SD) of the height calculated from mapped topographies plotted as a function of different oscillation amplitudes of the excitation tip. The standard deviation was calculated for the corrected height in the area between the white dashed lines in (b). The inset shows the zoomed-in region of the data for the oscillation amplitudes of the excitation tip between 215 mV $< D <$ 860 mV. (b) Topography of a raw data of height, mapping for a silicon wafer for the oscillation amplitude of the excitation tip $D = 840$ mV, (c) $D = 600$ mV. The black parabolic region is the avoidance area. (d) Crosstalk signals are corresponding to colored dashed lines in (c).

A_{base}. Thus, the avoidance threshold should be set considering the base crosstalk signals for different oscillation amplitudes of the excitation tip. Figure 3.1 shows the increase of measured base crosstalk signals for the oscillation amplitudes 120 mV $< D <$ 860 mV.

The maximum oscillation amplitude of the excitation tip $D = 860$ mV gives rise to the largest value of the base crosstalk signal $A_{base} = 280$ µV. It is expected that the avoidance threshold can be set to any value larger than the respective base crosstalk signal $A_{base} = 280$ µV. However, for avoidance threshold values between 280 µV $< A_{threshold} <$300 µV the detection tip did not move. The detection tip behaves in such a way when the crosstalk signal meets the avoidance threshold due to intrinsic electrical noise instead of proximity to the excitation tip. Hence, the avoidance threshold was set to $A_{threshold} = 300$ µV for the measurements with oscillation amplitudes between 120 mV $< D <$ 860 mV.

Figure 3.2(a) shows the standard deviation of height for seven values of oscillation amplitudes between 120 mV $< D <$ 840 mV. The standard deviation of the corrected

heights for all mapped topographies was calculated in the area marked by the white dashed lines in Fig. 3.2(b). The corrected height is calculated by subtracting a fitted paraboloid from the raw data. The subtraction of fitted paraboloid from the raw data eliminates a tilt of the piezoelectric scanner relative to the sample and the scanner bow during the scan. The following formula calculates the standard deviation σ of the corrected height,

$$\sigma = \sqrt{\frac{\sum_{x=1}^{M}\sum_{y=1}^{N}\left(h(x,y)-\overline{h}\right)^2}{MN}}. \tag{3.6}$$

Here, h is the corrected height, and $\overline{h}$ is the average of the corrected heights. M and N are the number of pixels along the width and length of the area within the dashed lines in Fig. 3.2(b). In Fig. 3.2(a), the values of standard deviation look almost constant except for $D = 120$ mV. The reason for the significant increase of the standard deviation of the height for $D = 120$ mV is attributed to the low value of the base crosstalk signal of $A_{CT} = 35$ µV. Here, the base crosstalk signal is much smaller than the avoidance threshold $A_{threshold} = 300$ µV. Therefore, by the time the crosstalk signal reached the avoidance threshold, the tips had already collided and lost contact with the sample. The collision effect appears as an increase in the topography height. Consequently, a much larger value was observed for the standard deviation of the mapped topography for $D = 120$ mV oscillation amplitude of the excitation tip. The inset of Fig. 3.2(a) shows a zoom-in of the standard deviation for the oscillation amplitude of the excitation tip between 215 mV $< D <$ 860 mV. For the oscillation amplitude between 215 mV $< D <$ 860 mV the standard deviation is the largest for $D = 840$ mV. Fig. 3.2(b) shows the raw data for the mapped topography for $D = 840$ mV, the oscillation amplitude of the excitation tip. Instability in the topography map is observed as uncompleted scan lines. The reason is related to the small difference between the base crosstalk signal $A_{base} = 280$µV and the avoidance threshold value $A_{threshold} = 300$ µV. As the detection tip scans the sample, crosstalk is fictitiously triggered by electronic noise and not due to the actual closeness of the excitation and detection tip. As a result, the detection tip did not finish scanning the corresponding line, and the remaining pixels are filled in a very short time with the data from the last scanned pixel. The small differences in the standard deviations for oscillation amplitudes between 215 mV $< D <$ 720 mV are caused by the instability of the feedback loop to adjust the detection tip height.

Figure 3.2(c) shows a mapped topography of a robust automated scan when the excitation tip oscillates with the amplitude $D = 600$ mV. A crosstalk signal is also

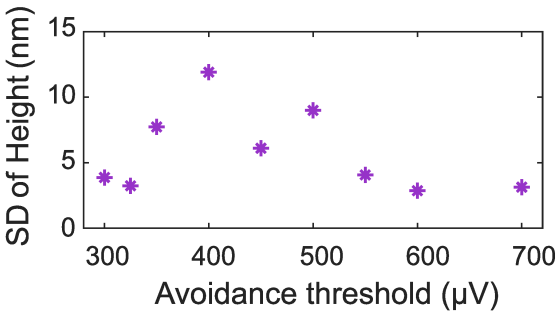

Figure 3.3: Standard deviation of the height calculated for the topography data measured for different avoidance thresholds. The oscillation amplitude of the excitaion and detection tips are corresponding to $D = 600$ mV and $B = 280$mV.

mapped concurrently with topography. To investigate the behavior of the crosstalk signal, some scan lines are selected from the topography image. Fig. 3.2(d) depicts the corresponding crosstalk signal of the selected lines in Fig. 3.2(c). Due to mechanical coupling effect, the base crosstalk signal increases smoothly as the detection tip approaches the excitation tip. The sudden increase of the crosstalk signals occurs when the crosstalk signals exceed the avoidance threshold value. for robust measurements, the oscillation amplitude of the excitation tip should be selected with care. Nevertheless, the robustness of the automated dual-tip SNOM measurements can be obtained for a rather wide range of oscillation amplitudes of the excitation tip.

3.3 Investigation of the avoidance threshold

Thus far, we have seen that the base crosstalk signal is proportional to the oscillation amplitude of the excitation and detection tips (Fig. 3.1). The avoidance threshold has to be set according to the base crosstalk signal. The avoidance threshold is another parameter that affects the overall stability of the measurements if it is not properly set. In this regard, we examine the effects of varying the avoidance thresholds on the robustness of the automated dual-tip SNOM measurements. In the corresponding experiment, the excitation and detection tip were oscillating with the amplitude of $D = 600$ mV and $B = 280$ mV respectively, resulting in the base crosstalk signal of $A_{base} = 205$ µV. The minimum avoidance threshold was set to $A_{threshold} = 300$ µV to prevent the artifact that was observed in Fig. 3.2(a) for the oscillation amplitude of $D = 840$ mV, due to the small difference between the base crosstalk signal and avoidance threshold. The oscillation amplitudes of the excitation and detection tips and the base crosstalk signal remained unchanged during the measurements. Figure

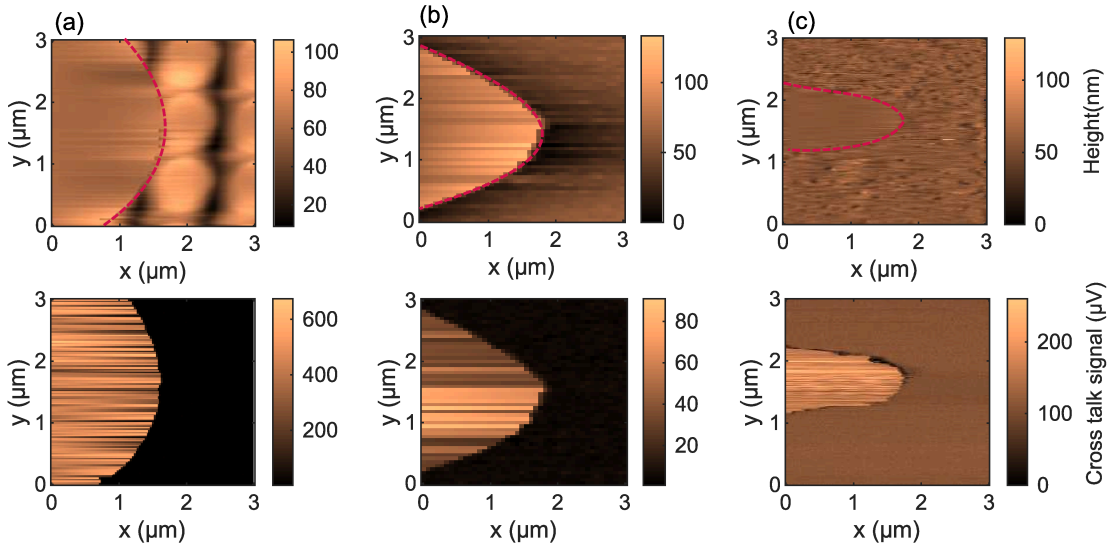

Figure 3.4: Mapped topography for different combinations of the excitation and detection tips when (a) excitation and detection tips are aperture fiber tips, (b) the excitation tip is an uncoated fiber tip and the detection tip is an aperture tip, and when (c) both excitation and detection tips are AFM tips.

3.3 displays the calculated standard deviation of height for the same area of the sample when the avoidance threshold was set to different values. For avoidance thresholds between 300 µV $< A_{threshold} <$700 µV, the measurements were robust, and no collision of the tips was observed during mapping the topography by the detection tip. For the same scan area, the instability of the feedback loop again causes a slight variation in the standard deviation of heights. For the avoidance threshold of $A_{threshold} > 700$ µV, due to the large difference between the avoidance threshold and the base crosstalk signal, the crosstalk signal reached the set value of the avoidance threshold only after a collision between two tips. This effect is similar to what was observed in Fig. 3.2(a) for the oscillation amplitude of $D = 120$ mV. In conclusion, the automated scan procedure is not robust for any arbitrary values of the avoidance threshold larger than the base crosstalk signal. However, as a rule of thumb, a difference of about 100 µV between the avoidance threshold and base crosstalk signal $A_{threshold} - A_{base} = 100$ µV lead to the stable automated scan by the detection tip.

3.4 Automated dual-tip scheme for different types of tips

The collision prevention scheme of the dual-tip aperture SNOM can be used in various types of scanning probe microscopes to explore the properties of a surface. In order to test the feasibility of the automated dual-tip scheme for different kinds of tips,

various combinations of SPM probes have been employed for the automated dual-tip scan.

Figure 3.4(a) is the topography of a dielectric metasurface mapped by a metal-coated aperture tip when the excitation tip was also a metal-coated aperture tip. Figure 3.4(b) shows the topography map of the gold film when an uncoated fiber probe was used as an excitation tip and a metal-coated aperture tip as a detection tip. The size of the avoidance area depends on the size of the excitation and detection tips' apex, which is smaller when an uncoated fiber tip is used as an excitation tip in Fig. 3.4(b). In Fig. 3.4(c), both excitation and detection tips are AFM tips, made of fused silica, with an apex of a few tens of nanometers. The avoidance area is the smallest compared to Fig. 3.4(a) and (b). Moreover, different avoidance areas indicate the change of the minimum distance of different pairs of excitation and detection tips. For instance, if a quantum emitter is grafted on the apex of an uncoated tip, the detection tip can be brought even closer to the excitation point. Both mapped topographies and crosstalk signals for different combinations of excitation and detection tips denote the stability of the automated scan with the detection tip regardless of the tip type. Finally, a well-defined border of the avoidance areas corroborates the versatility of the automated collision prevention scheme to be implemented for various types of SPM tip combinations.

4 Dipolar emission from aperture tip

Aperture tips as optical near-field antennas enable the excitation and detection of evanescent waves [110]. The geometry and material properties of a SNOM tip apex determines the electromagnetic field distribution from its aperture at the apex (illumination mode) and its detection sensitivity to electric and magnetic fields (collection mode) [30, 111].

In the dual-tip SNOM, prior knowledge about the polarization of the emission from excitation aperture tips is critical to investigate the polarization-sensitive near-field phenomena [112–114]. Different models have been suggested to describe the emission from aperture SNOM tips. The Bethe-Bouwkamp model is the most well-known model [21, 22]. The model was first proposed to explain the diffraction of light through a subwavelength aperture in an infinite conducting plane. According to this model, the emission from the subwavelength aperture in an infinite conducting plane corresponds to the radiation of an in-plane magnetic dipole and an out-of-plane electric dipole located at the center of the aperture. The electric dipole appears in the model when a plane wave illuminates the aperture at an oblique angle.

The near-field distribution from an aperture tip was mapped for the first time using dye molecules [39]. Dye molecules behave like electric dipoles. When illuminated with the aperture tip, the emission pattern of the dye molecule corresponds to the electromagnetic field distribution from the aperture tip, projected along the molecular dipole moment. The Bethe-Bouwkamp model properly described the measured electric field distribution detected by dye molecules in the near-field of the aperture tip. However, the far-field angular measurements of the transmitted light through the aperture tip could not be explained by the Bethe-Bouwkamp model [23, 24]. The discrepancy was raised from different boundary conditions for the conical geometry

of the aperture tip compared to the aperture in an infinite metallic plane. Drezet developed a model that applies the effective electric and magnetic dipoles with different orientations to fulfill the boundary conditions imposed by different conical geometries of aperture SNOM tips [28]. Furthermore, the emission from an aperture SNOM tip can be assumed as the radiation of a nanoantenna whose emission pattern can be described by a multipole expansion method [115]. Typically, a combination of the electric and magnetic dipole is sufficient to describe the angular field distribution from the aperture tips. If the electric and magnetic dipoles cannot describe the emission pattern, the contribution of higher-order multipoles should be considered [25].

Image formation is also non-trivial when aperture SNOM tips are used in the collection mode. Greffet explained the equivalence of the collection and illumination modes based on the reciprocity of electromagnetic fields [5]. The reciprocity links the detected signal to the geometry as well as the near field of the sample [116]. The apex geometry of SNOM tips determines the dominant excited dipole moments from the aperture. Likewise, when aperture SNOM tips are used for detection according to the reciprocity of electromagnetic fields, induced dipole moments due to scattered electric or magnetic field distributions rely on the geometry of the aperture tip [30, 73, 74, 117, 118]. For instance, fiber tips with the apex plane parallel to a sample [119, 120] and hollow pyramid probes exhibited higher sensitivity to the in-plane magnetic field [121, 122]. A split ring tip detects out-of-plane magnetic field components [123]. Aperture tips have shown sensitivity to both electric and magnetic fields [124]. In the case of a gold-coated aperture tip (similar to aperture tips used in dual-tip SNOM measurements in this thesis), if the thickness of a coating enables the excitation of circularly symmetric plasmon modes, the detected signal is the magnetic field intensity [27, 30, 125]. The detection sensitivity of the aperture tip can be tuned to either electric or magnetic fields, if the thickness of the metallic rim is altered [29, 120]. Recently, an imaging theory based on the reciprocity of the electromagnetic field and multipole expansion method was proposed to design SNOM tips with predefined sensitivity to the electric or magnetic field [126].

The emission from aperture fiber tips can be characterized through the near-field pattern of SPPs at an air-gold interface. In this regard, the polarization and the shape of the dipolar emission from the excitation tip can be deduced from the mapped SPPs pattern at air-gold interface by the detection tip. An unstructured monocrystalline gold platelet ensures that any asymmetry of the mapped SPPs pattern is only due to the emission from the aperture fiber tip. However, it should be noted that the

avoidance area does not allow access to an entire near-field pattern, which is one of the shortcomings of the dual-tip SNOM measurement technique. Therefore, the conclusions that are drawn from near-field measurements should be supported by numerical simulations.

The structure of this chapter is as follows: Section 4.1 explains the fundamentals of surface plasmon polaritons. In Section 4.2, the results of the first successful near-field measurements using automated dual-tip SNOM to excite and detect SPPs waves on a gold film at visible and near-infrared wavelengths are presented. The automated dual-tip SNOM was operated at a near-infrared wavelength for the first time. I will show that the measured near-field pattern of the SPPs can be fitted to a polar equation. From the fitting parameters, the propagation length of the SPPs will be attained. In Section 4.3, I will discuss the polarization properties of the bent fiber aperture tip that behaves as a near-field polarization filter. Section 4.4 describes the effect of a bent aperture SNOM tip with a tilted aperture plane at its apex on the electromagnetic field's excitation and detection mechanism.

In Section 4.5 to study the near-field emission from aperture tips, the near-field pattern of SPPs on a gold film will be calculated considering the Bethe-Bouwkamp model and truncated cone model, representing the real aperture fiber tip. We will see that the Bethe-Bouwkamp model is sufficient to describe the SPP near-field pattern mapped by the detection tip.

Finally, in the last section, I will discuss the measured emission patterns from three different pairs of excitation and detection tips. The near-field emission patterns will be compared with numerical simulations applying the Bethe-Bouwkaump model. We will see that the geometry of the bend and the plane of the aperture will affect the emission from the excitation aperture tip and correspondingly the excited SPPs pattern. Due to its geometry at the tip's apex, the emission from one of the investigated aperture tips satisfied the first Kerker condition. As a result, a directional propagation of the SPPs was observed. To the best of our knowledge, it was the first directional SPPs excited and detected in the near field using an aperture tip SNOM. [1]

4.1 Fundamentals of surface plasmon polaritons

Scanning near-field optical microscopy and plasmonics share a long history that dates back to the early days of both research fields [128]. Intriguing optical properties at an air-metal interface are due to surface plasmons, i.e., a collective oscillation of the

[1] Parts of the results of this chapter have been published in [127].

free electrons at a dielectric-metal interface. Electromagnetic waves coupled to surface plasmons turn it into the surface plasmon-polaritons (SPPs). SPPs are confined electromagnetic waves propagating typically over tens of micrometers along an interface determined by the excitation wavelength. However, they decay in the direction normal to an interface within the optical near-field region. The subwavelength nature of SPPs allows manipulating light propagation below the diffraction limit, enabling many promising applications [129–132].

Applying suitable boundary conditions to the Maxwell's equations for an infinite dielectric-metal interface leads to the dispersion relation of SPPs [19],

$$k_{\mathrm{SPP}} = \frac{2\pi}{\lambda_0}\sqrt{\frac{\epsilon_d \epsilon_m}{\epsilon_d + \epsilon_m}}, \tag{4.1}$$

where k_{SPP} is a propagation constant of SPPs wave, λ_0 is the wavelength of an incident electromagnetic wave in free space, ϵ_d and ϵ_m are the dielectric constants of a dielectric medium and a metal, respectively. Eq. 4.1 indicates that the magnitude of SPP's wave vector is larger when it is compared with an incident wave vector $\frac{2\pi}{\lambda_0}$ in free space. In other words, the SPPs have larger momentum than that of an incident beam. Thus, to excite the SPPs, a momentum matching scheme is required to enable coupling electromagnetic waves from free space to surface plasmons. Different schemes have been utilized to excite the SPPs [19]. In this thesis, the SPPs are always excited on an air-gold interface by aperture fiber tips. The emission from a subwavelength aperture tip contains evanescent waves with wave vectors larger than the wave vector of surface plasmons. Thus, the momentum matching condition is fulfilled. Moreover, the excitation aperture tip as a point source of light allows sample illumination without any background signal from the far field.

One of the most important quantities for plasmonic waveguides is the propagation length of the SPPs which is defined as a distance that SPPs can propagate before their amplitudes drop to $1/e$ of their initial value. The propagation length L_{SPP}, at the excitation wavelength λ_0 for an infinitely thick plasmonic film is calculated with the following expression,

$$L_{\mathrm{SPP}} = \frac{1}{2\,\mathrm{Im}(k_{\mathrm{SPP}})}, \tag{4.2}$$

where $\mathrm{Im}(k_{\mathrm{SPP}})$ is the imaginary part of SPPs' propagation constant. Since different techniques were suggested to enhance the propagation length of SPPs [133–135], the direct and accurate measurement of SPPs' propagation length is crucial for applications of plasmonic waveguides.

4.2 Excitation of SPPs by aperture SNOM tips

The first application of the dual-tip SNOM was to measure the propagation length of SPPs on a gold stripe waveguide [92]. Thus far, near-field measurements by dual-tip SNOM have been carried out only for visible wavelengths using a detection tip that was not automated. A user had to stop a detection tip manually to prevent a collision with an excitation tip. Because of the early stop of the detection tip, the near-field optical response around the excitation tip could not be mapped accurately. The aperture SNOM tip acts as a point source dipole. Therefore, the near-field emission pattern from the aperture tip can be characterized through the map of SPPs at an air-gold interface. The near-field pattern of SPPs excited by the aperture tip mimics the near-field pattern observed when SPPs are excited by in-plane electric or magnetic dipoles. Thus, the resulting SPP's pattern features two lobes similar to in-plane dipole radiation at an air-gold interface. The polarization of the electric field, at the aperture plane, can be deduced from the orientation of SPP near-field pattern [119].

As a proof of principle, the automated dual-tip SNOM was utilized to measure the near-field pattern of the SPPs excited at wavelengths, $\lambda_0 = 633$ nm and $\lambda_0 = 1550$ nm on a polycrystalline gold film with a thickness of 225 nm. The gold film thickness is larger than the gold skin depth at a respective excitation wavelength [19]. The automated detection tip maps the entire near-field distribution around the excitation tip. Figure 4.1(a) and (b) are the measured near-field patterns of SPPs for excitation wavelengths $\lambda_0 = 633$ nm and $\lambda_0 = 1550$ nm.

A simplified expression for the intensity of the SPPs due to in-plane dipole excitation follows the expression [136],

$$I(\mathrm{r}, \varphi) \propto \frac{1}{\mathrm{r}} \exp\big(-2\,\mathrm{Im}\{k_{\mathrm{SPP}}\}\mathrm{r}\big) \cos^2(\varphi), \tag{4.3}$$

where $I(\mathrm{r}, \varphi)$ is the intensity of SPPs in a polar coordinate (r, φ). The measured near-field intensity in Figs. 4.1(a) and (b) were fitted to Eq. (4.3). From the fitted parameters, the propagation length of SPPs can be obtained. The propagation length of SPPs at an air-gold interface depends only on the illumination wavelength (Eqs. 4.1 and 4.2).

Typically, the symmetry line along the propagation direction of SPPs is selected to calculate the propagation length. The intensity line profile is fitted to an exponentially decaying function, and from the fitting parameter, the propagation length is calculated. However, when the near-field pattern of the excited SPPs is available, the initial position of the excitation aperture tip can be found more accurately. Thus,

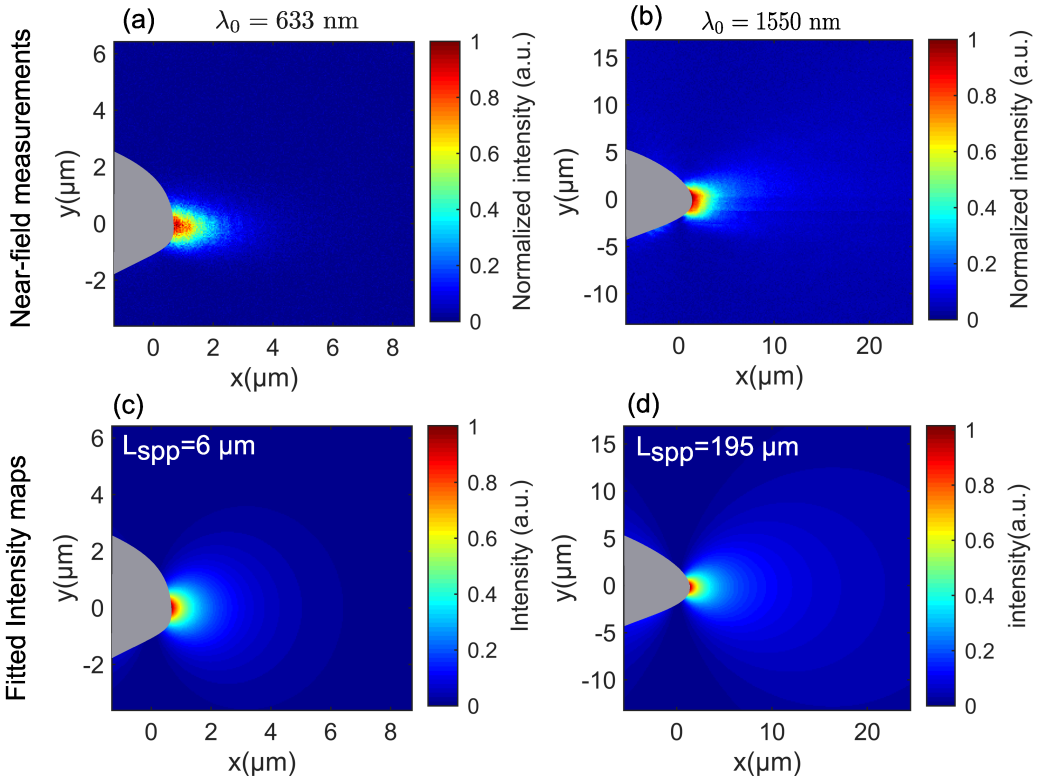

Figure 4.1: Near-field patterns of SPPs on a gold film excited by the aperture SNOM tip at wavelengths (a) $\lambda_0 = 633$ nm and (b) $\lambda_0 = 1550$ nm. (c) and (d) are fitted intensity maps to Eq. (4.3) using the data of SPPs near-field intensity patterns in (a) and (b) respectively. The coordinate of the aperture tip position is set to $(0, 0)$. The gray parabolic-like region is the avoidance area.

the SPPs pattern is fitted to Eq. (4.3) to extract the propagation length of SPPs. Figures 4.1 (c) and (d) are calculated intensities based on the fitted parameter obtained from the measured intensities in Figs. 4.1 (a) and (b), using Eq. (4.3). The imaginary part of k_{SPP} is calculated from the fitted intensity maps in Fig. 4.1 (c) and (d). The intensities values within the avoidance area (gray areas) in Figs. 4.1 (c) and (d) are set to zero, enabling the comparison of the simulation results with the near-field measurements in (a) and (b). For the dual-tip SNOM measurement at a wavelength $\lambda_0 = 633$ nm the propagation length $L_{\mathrm{SPP}} = 6$ µm is attained. If Eqs. (4.1) and (4.2) are applied to calculate the propagation length of excited SPPs at a wavelength $\lambda_0 = 633$ nm with a dielectric constant $\epsilon_m = -11.75 + 1.25i$, the resulting propagation length of the SPPs is $L_{\mathrm{SPP}} = 9.8$ µm.

In the case of the excitation wavelength $\lambda_0 = 1550$ nm, the obtained propagation length from the fitted function in Eq. (4.3) is $L_{\mathrm{SPP}} = 195$ µm. The calculation of propagation length using Eqs. (4.1) and (4.2) for the dielectric constant $\epsilon_m = -115.13 + 11.25i$ leads to $L_{\mathrm{SPP}} = 290$ µm. The observed discrepancy in propagation

length of the calculated values and the ones derived from the near-field measurements can be attributed to the roughness of the gold film that causes SPPs to scatter, which, in turn, results in a shorter propagation length [137].

Ohmic losses of metallic films have been the main obstacle to integrate plasmonic waveguides into photonic circuits. One approach to increase the propagation length in metallic structures such as gold is to reduce the ohmic losses by manipulating intrinsic structural and material properties to enhance whose surface roughness [138–140]. Compared to polycrystalline gold, monocrystalline gold platelets have stronger plasmonic resonances and a longer propagation length [141, 142].

In the next sections, for the characterization of emission from aperture SNOM tips through the near-field pattern of SPPs, a monocrystalline gold platelet was utilized as one of the main platforms for future quantum plasmonic [143].

4.3 Polarization characteristic of bent aperture fiber tips

The optical response of most photonic systems is polarization-dependent. Therefore, in far-field optical microscopy, the polarization of an incident beam is determined before an experiment. Likewise, polarization-resolved measurements in the near field, using aperture SNOM tips, require knowledge of the polarization of the emitted light from the apertures [48]. The aperture SNOM tip with a bent fiber is one of the commonly used aperture probes for near-field measurements. Moreover, the bent fiber tip is instrumental in implementing the dual-tip SNOM configuration. However, determining the polarization of the emission from a bent aperture tip is non-trivial. Since the polarization of a laser coupled to a bent fiber tip is not always preserved, it is necessary to determine the polarization of the light emitted from an aperture before carrying out polarization-resolved near-field measurements. Far-field measurements have already been performed to study the polarization of the emission from bent fiber tips [48, 144–146]. It was shown that the symmetry break induced by the bend along the fiber tips leads to the polarization-dependent losses in the fiber aperture tips [48, 146].

A study of the polarization sensitivity of single-mode (SM) and multi-mode (MM) fibers found that either transverse electric (TE) or transverse magnetic (TM) modes experience greater losses based on the radius of a bend [147]. Nevertheless, MM fiber aperture tips with larger numerical aperture showed less polarization sensitivity than SM fiber aperture tips. Based on these findings, in the dual-tip SNOM measurement in this thesis, SM mode fiber aperture tips are always used as excitation tips, and

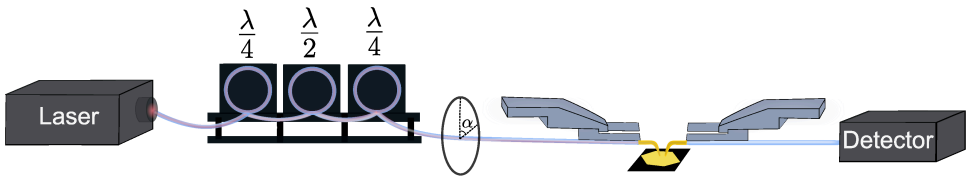

Figure 4.2: Dual-tip SNOM setup for characterizing the polarization of the emission from excitation aperture tips. The laser beam with a polarization angle α is coupled to the end of the fiber tip. The emission from the aperture tip at its apex excites the SPPs on a monocrystalline gold platelet. The detection tip maps the near-field pattern of SPPs that reflects the properties of the emission from the excitation tip.

MM fiber aperture tips that are less polarization-sensitive are employed as detection tips. Before polarization-resolved near-field measurements, the characterization of both SM and MM fiber aperture tips in the far field is required, which is a demanding and time-consuming task. The far-field characterization of aperture SNOM tips at near-infrared wavelengths is even more challenging than at visible wavelengths. Moreover, the distribution of electromagnetic fields in the near field of the aperture tip cannot be determined simply from far-field characterization. Nevertheless, the detection tip of the automated dual-tip SNOM measures the emission from an aperture fiber tip through SPP near-field pattern at an air-gold interface. The polarization of the emission from the excitation tip can be determined, according to the near-field pattern of SPPs.

In the experiment, SPPs were excited at a wavelength of 1550 nm at an air-gold interface. A detection tip mapped the corresponding near-field pattern of SPPs. The sample under investigation consists of a truncated triangle monocrystalline gold platelet, with an area of 100 μm^2 and a thickness of 225 nm. The excitation tip was placed roughly in the middle of the gold platelet. It should be noted that the light coupled to a bent fiber tip, at the wavelength 1550 nm, is linearly polarized when it reaches the aperture with a diameter smaller than 1 µm [146]. Thus, the orientation of the SPP near-field pattern indicates the polarization of the electric field at the aperture plane of an excitation tip after passing through the bend of the fiber tip [20, 48, 148].

Figure 4.2 shows the dual-tip SNOM setup used to characterize the polarization of the emitted light from a bent SM fiber aperture tip. A fiber polarization controller changes the angle of a polarized light coupled to the fiber end. Figure 4.3(a-d) depicts the mapped near-field intensity of SPPs for different input polarization angles α, coupled to the fiber end (Fig. 4.2). The input power was kept constant during the

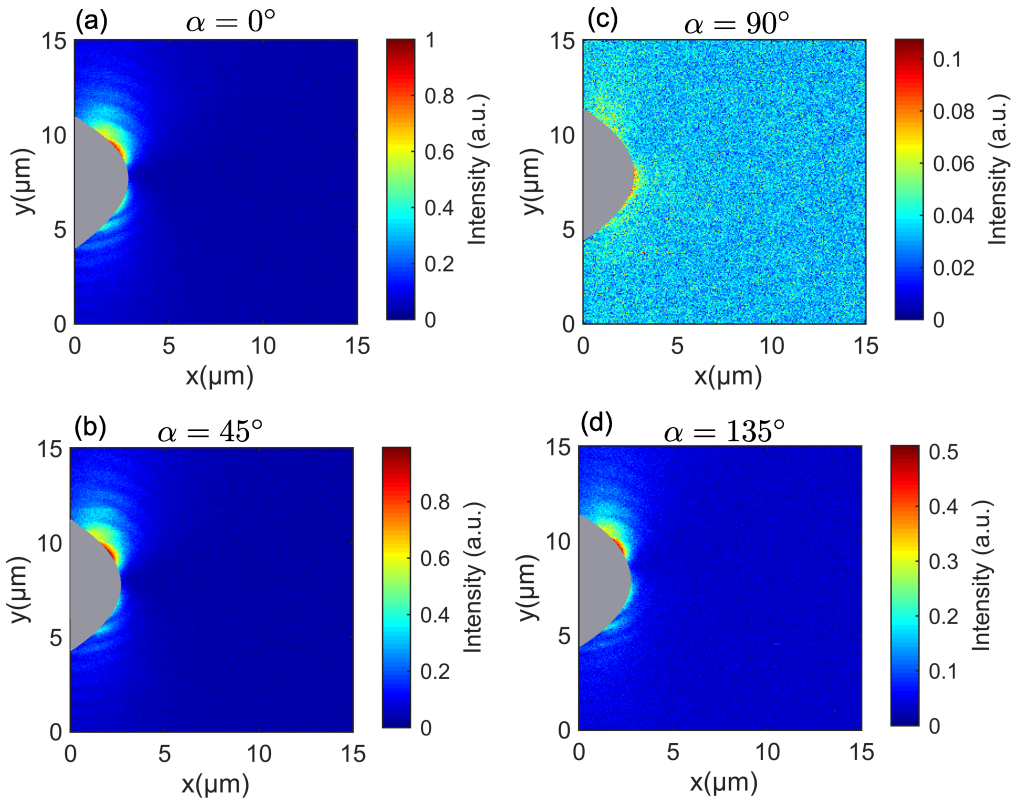

Figure 4.3: SPPs near-field patterns mapped by a detection tip when they were excited with different polarization angles (α) coupled to the excitation tip (a) $\alpha = 0$ (b) $\alpha = 45°$ (c) $\alpha = 90°$ (d) $\alpha = 135°$. The gray region shows the avoidance area.

measurements. The expected near-field pattern of SPPs with two lobes is observed in Fig. 4.3(a-d) for the emission from a subwavelength aperture with a diameter of 250 nm. The orientation of SPPs near-field maps for all input polarizations is along the y-axis but with different maximum intensities. The same propagation direction of SPPs and different maximum intensities implies that the polarization of the coupled laser beam is not preserved, and the fiber bend acts as a polarization filter for the electric field component along the x-axis. In Fig. 4.3(a), the maximum intensity was mapped for $\alpha = 0°$ where the polarization of a laser beam coupled to the fiber aperture tip is along the y-axis. Comparing with the maximum intensities measure in Figs. 4.3(b-d), it is observed that the electric field polarization of a fiber mode arriving at the aperture plane is also along the y-axis. In other words, the y-polarized light coupled to the end of the fiber tip, reaches the aperture without experiencing substantial losses due to the bend.

On the other hand, the lowest values of the mapped intensities were observed for an input angle of $\alpha = 90°$ in Fig. 4.3(c), where the polarization of a laser beam coupled to the fiber end of the excitation tip was along the x-axis. From the mapped

near-field intensity by the detection tip, it is apparent that the bent geometry of the fiber tip was responsible for the maximum bending losses of an input laser beam with polarization along the x-axis.

In Fig. 4.3(a-d), the maximum normalized intensities have changed for different input polarization angles. Figures 4.3(b) and (d) are the mapped intensities for the input polarization angles $\alpha = 45°$ and $\alpha = 135°$, respectively. As a result of the polarization-dependent losses of a bent fiber, the maximum value of the mapped intensities was reduced for these two input polarization angles due to the loss of the polarized electric field along the x-axis. Nevertheless, near-field maps of SPPs patterns remained unchanged. These observations agree with the results of far-field polarization sensitivity measurements of bent fiber tips, corroborating the fact that a bent aperture fiber tip serves as a near-field polarization filter. The polarization sensitivities mostly along the polarization angles $\alpha = 0°$ or $\alpha = 90°$ were observed in the far-field polarization characterization of different bent aperture fiber tips [48].

The asymmetry of SPPs patterns in Fig. 4.3(a-d) could be attributed to a rotational asymmetry of the fiber tip's aperture plane around its center or a tilt of the aperture plane that would lead to the asymmetry of SPPs pattern. Fringes in the mapped near-field patterns resulted from the interference between the excited SPPs at the aperture position with SPPs reflected from the edges of the gold platelet. The dual-tip SNOM provides a convenient and reliable method to characterize the polarization of SM or MM fiber tips. Since detection tips fabricated from MM fibers might also exhibit some degree of polarization sensitivity, it is recommended to use the same pair of excitation and detection tips to perform polarization-resolved near-field measurements.

4.4 Excitation and detection through tilted aperture fiber tips

We have seen that the bent of a SM fiber tip leads to the polarization filtering of the emission from its aperture. This bend also leads to a tilt of the aperture plane . As a result, the aperture plane is no longer parallel to the sample surface (see Fig. 4.4).

Figure. 4.4(a) illustrates both excitation and detection tips making an angle (θ') with the surface normal. In the next section, we will see that the emission from an aperture fiber tip can be described by the radiation of a magnetic dipole located at the center of the aperture [4]. In Fig. 4.4(a), the magnetic dipole is depicted with a green double arrow parallel to the aperture plane of the excitation tip. In Fig. 4.4(b), xyz displays the sample coordinate with the magnetic dipole at the polar angle (θ)

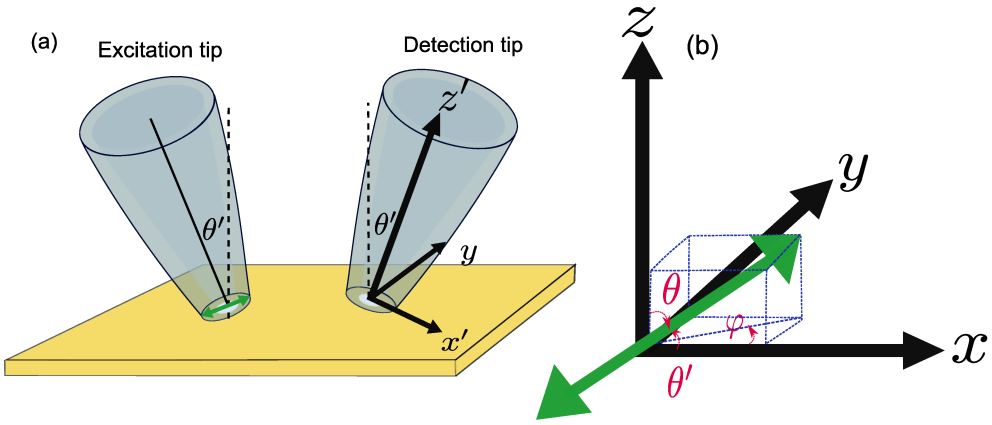

Figure 4.4: (a) Excitation and detection tip with an angle θ' relative to the surface normal. The coordinate system of the detection tip $x'yz'$ is obtained by rotating the sample coordinate system xyz around the y axis with an angle θ'. (b) Green double arrow denotes a magnetic dipole with azimuthal φ and polar θ angles.

and the azimuthal angle (φ). The angle θ is obtained from the tilt angle (θ') of the aperture tip ($\theta+\theta' = 90°$), and the angle φ is determined according to the orientation of near-field pattern of SPPs mapped by a detection tip.

When using an aperture tip with a tilt for near-field detection, the detection plane is not parallel to the sample surface. Hence, the numerically calculated components of the electromagnetic field in a plane parallel to the sample should be rotated around the y-axis by the angle $-\theta'$ to represent the electromagnetic field in the coordinate of a detection tip $x'yz'$ [101]. The electric field components in the $x'yz'$ coordinate are calculated with the following relations,

$$\begin{aligned} E_{x'} &= E_x \cos\theta' - E_z \sin\theta', \\ E_{y'} &= E_y, \\ E_{z'} &= E_x \sin\theta' + E_z \cos\theta' \end{aligned} \tag{4.4}$$

Likewise, the magnetic field components are transformed to the coordinate of the detection tip. Typically the angle θ' is slightly different for excitation and detection tip. According to Eq. (4.4) both E_x and E_z components contribute to the mapped intensity of E'_x and E'_z. However, when the aperture plane is parallel to the sample surface, only electromagnetic field components parallel to the sample surface can be mapped by the detection tip [117]. When the tilt of the apex plane is negligible or the electric field component E_x is an order of magnitude larger than E_z, it is not required to calculate the mapped intensity in the coordinate system of a detection tip.

Another important issue concerning the geometry of the aperture tip's apex is the angle of the aperture plane relative to surface plane that is not always equal to θ'.

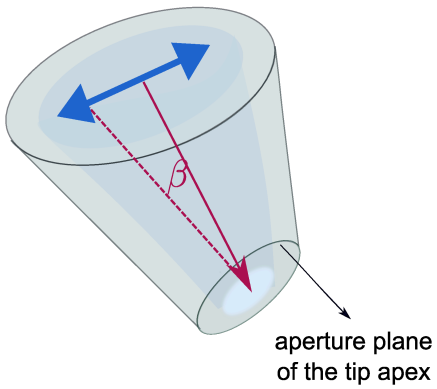

Figure 4.5: Schematic of an aperture tip whose aperture plane at the apex is tilted relative to an incident beam (red vector). The incident beam makes an angle β relative to the aperture plane normal (red dashed line). The blue double arrow represents an electric dipole.

Figure. 4.5 demonstrates the aperture fiber tip whose aperture plane normal (surface normal) is not along the fiber axis. The tilt of an aperture plane relative to the fiber axis leads to the oblique angle of an incidence beam at the aperture plane. Thus, the electric field has vertical and tangential components. The result of this condition on SPPs radiation pattern will be discussed in Section 4.6.

4.5 Modeling the emission from an aperture tip

Before characterizing the emission pattern from different aperture tips, we need to find a proper model to calculate the emission pattern numerically. Several models can account for the emission pattern from aperture tips including the Bethe-Bouwkamp model [22], a metallic ring [13] and also a truncated cone [28]. A comprehensive model to describe the emission from the aperture tip involves rigorous numerical calculations, considering the effect of a tip's geometry, the coating thickness, and the material composition of the coating [29, 30, 120].

We examine the applicability of two models describing the emission from an aperture tip. The first model is a magnetic dipole based on the Bethe-Boukamp model and the second, more comprehensive model is a truncated cone representing a real aperture tip with the metallic coating.

In this regard, SPPs patterns were calculated at an air-gold interface, first for an in-plane magnetic dipole excitation (Fig. 4.6(a)) and then a truncated cone with a symmetry axis normal to the surface (Fig. 4.6(b)). However, the excitation aperture tip used in dual-tip SNOM measurements forms an angle with the surface normal.

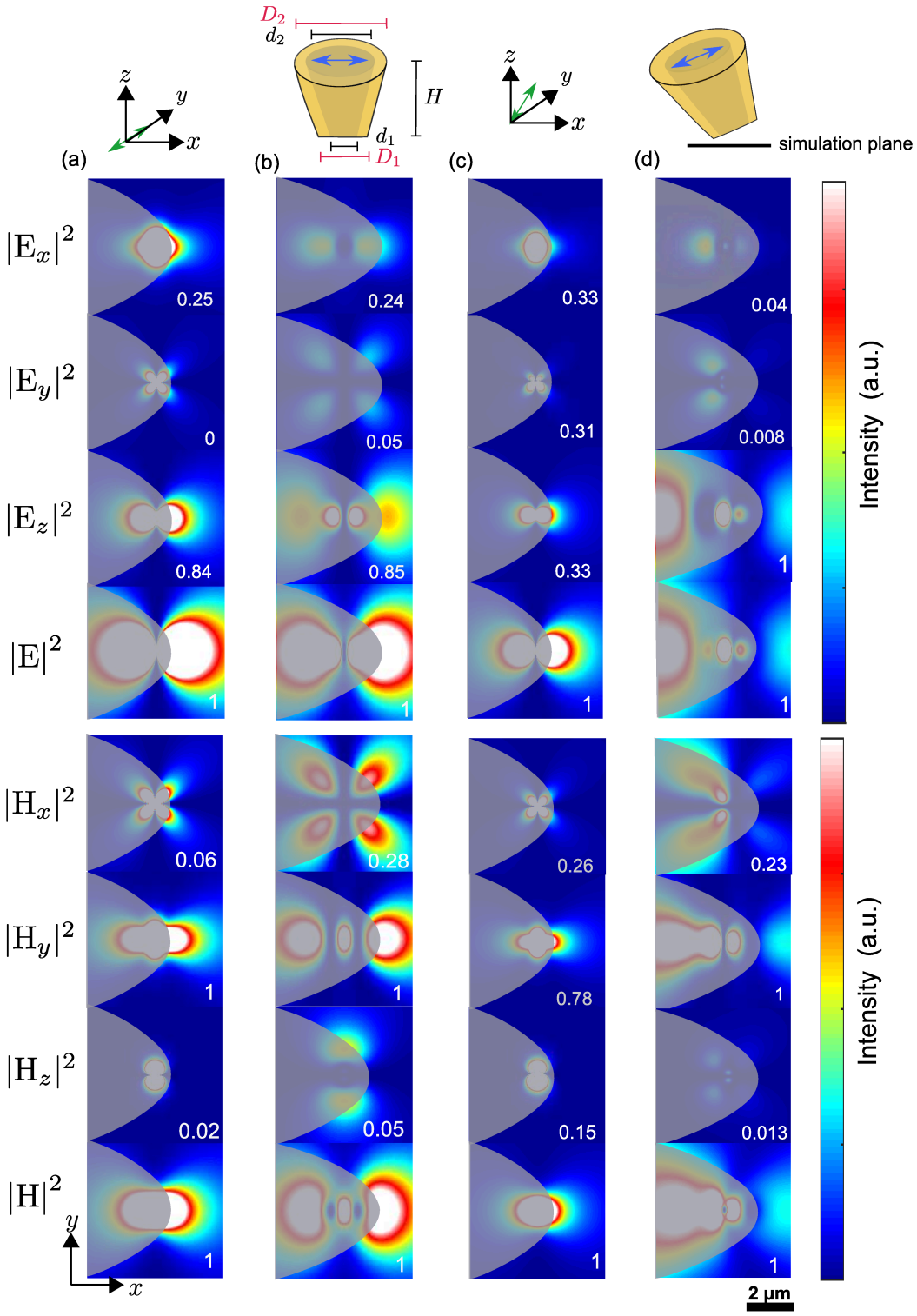

Figure 4.6: Numerically calculated intensity maps of electric and magnetic field components of SPPs in a plane 15 nm above a gold film when the excitation plane is 30 nm above the gold film.(a) Magnetic dipole (the green double arrow) with angles $\theta = 90°$ and $\varphi = 90°$.(b) Truncated cone with a symmetry axis normal to the surface. The blue double arrow is an electric dipole. (c) Tilted magnetic dipole with $\theta = 60°$ and $\varphi = 90°$. (d) Truncated cone with a symmetry axis making an angle $\theta' = 30°$ with respect to the surface normal. To normalize the intensity of electric (magnetic) field components, they were divided by the maximum intensity of the total electric (magnetic) field. The value on the corner of each panel shows the maximum normalized intensity of the respective component.

Therefore, to consider the effect of a tilted aperture fiber tip on the near-field patterns of SPPs, the SPPs were also excited by a tilted magnetic dipole (Fig. 4.6(d)) and a tilted aperture tip (Fig. 4.6(e)).

Using the FDTD Solver Lumerical, we performed numerical calculations of the intensity components of SPPs in a plane 15 nm above the gold film; when the plane of the excitation source, illuminating at a wavelength $\lambda = 1550$ nm was located 30 nm above the gold film. Figure 4.6(a) depicts the intensity of electric and magnetic field components of the excited SPPs by a magnetic dipole with angles $\theta = 90°$ and $\varphi = 90°$. Fig. 4.6(b) shows a real geometry of the aperture tip (truncated cone) with an opening angle of 15° and a symmetry axis normal to the sample surface. The numerical calculation was carried out for silica as a tapered fiber (inner part of the truncated cone) and gold as the coating of a fiber tip (outer part of the truncated cone). The diameters of the aperture and the apex plane, $d_1 = 300$ nm and $D_1 = 750$ nm are consistent with the average aperture tip size used in dual-tip SNOM measurements. The height of the truncated cone was taken as $H = 1$ µm. According to the opening angle of the truncated cone and its height, the diameters of $d_2 = 485$ nm and $D_2 = 975$ nm were obtained for its base plane used in the numerical simulation.

Figure. 4.6(c) visualizes the intensity of electromagnetic field components of SPPs excited by a tilted magnetic dipole with angles $\theta = 60°$ and $\varphi = 90°$. Figure. 4.6(d) shows the intensity of the electromagnetic field components when the symmetry axis of the aperture tip in Fig. 4.6(b) is tilted with an angle $\theta' = 30°$ relative to the surface normal. To investigate the contribution of each component of electric (magnetic) field intensity in the mapped near-field pattern, they were normalized to the maximum calculated intensity of all the electric (magnetic) field components. The value at the corner of each panel denotes the maximum normalized intensity of the corresponding component. After normalization, a parabolic region equivalent to an avoidance area was set to zero for the sake of comparison with measured intensities by the detection tip.

The electromagnetic field intensity components of SPPs excited by an in-plane magnetic dipole in Fig. 4.6(a) and the electromagnetic field intensity components of SPPs in Fig. 4.6(b) show similar near-field patterns. Furthermore, in both models, the electric field E_z and the magnetic field H_y have a dominant contribution to the total intensities. These results confirm that the emission from an aperture tip can be described by the radiation pattern of an in-plane magnetic dipole.

When a dipole is tilted relative to the surface normal of a lossy medium, such

as gold, its radiation pattern turns out to be asymmetric. However, the degree of asymmetry in the near-field pattern of mapped SPPs relies on the dipole tilt angle. The maximum degree of asymmetry can only be observed for a particular tilt angle of a dipole source [149]. For the calculated tilt angles $\theta = 60°$ and $\varphi = 90°$ of a magnetic dipole in Fig. 4.6(c), the asymmetry is not apparent when part of the near-field pattern is covered with the avoidance area.

In Fig. 4.6(d), the asymmetry of electromagnetic field distribution of SPPs excited by a tilted aperture tip is more pronounced. It was shown that the SPPs modes are excited at an interface between the tapered fiber and a gold coating of an aperture tip (truncated cone) [125, 150]. Hence, the SPPs modes excited at the apex of an aperture plane enhance the excited SPPs on an air-gold interface when the aperture plane is parallel to the interface. It is worth mentioning that the electromagnetic field intensity components of SPPs are calculated in a plane parallel to the air-gold interface.

However, for the tilted aperture plane of the excitation tip, the effect of the electromagnetic field enhancement is stronger when the lower part of the aperture plane is 15 nm above the gold film, leading to the interference of the SPPs at the aperture plane with the SPPs excited on the gold film. On the other hand, the excited SPPs at the upper part of the aperture plane, which are hundreds of nanometers above the gold interface, do not significantly affect the excited SPPs on the gold film. As a result, the asymmetry is observed in the calculated intensity of electromagnetic field components in Fig. 4.6(d). The comparison between the total electric $|\mathbf{E}|^2$ or magnetic $|\mathbf{H}|^2$ intensities in Figs. 4.6(a-d) reveals the fact that the near-field patterns of SPPs are nearly the same for all suggested models representing an excitation aperture tip.

Nevertheless, the asymmetry in the measured near-field pattern, related to the tilt of the aperture plane at the excitation tip's apex, determines if the magnetic dipole model is sufficient to describe the emission from an aperture fiber tip or the real geometry of the tip should be considered.

4.6 Maps of near-field emission from different aperture tips

The electromagnetic field distribution of the emission from a bent aperture fiber tip depends on the geometric properties of the bend and the geometry of the aperture apex. The geometry of the bend determines the polarization of the fiber mode that reaches the aperture plane [48,146], and the geometry of the aperture apex determines

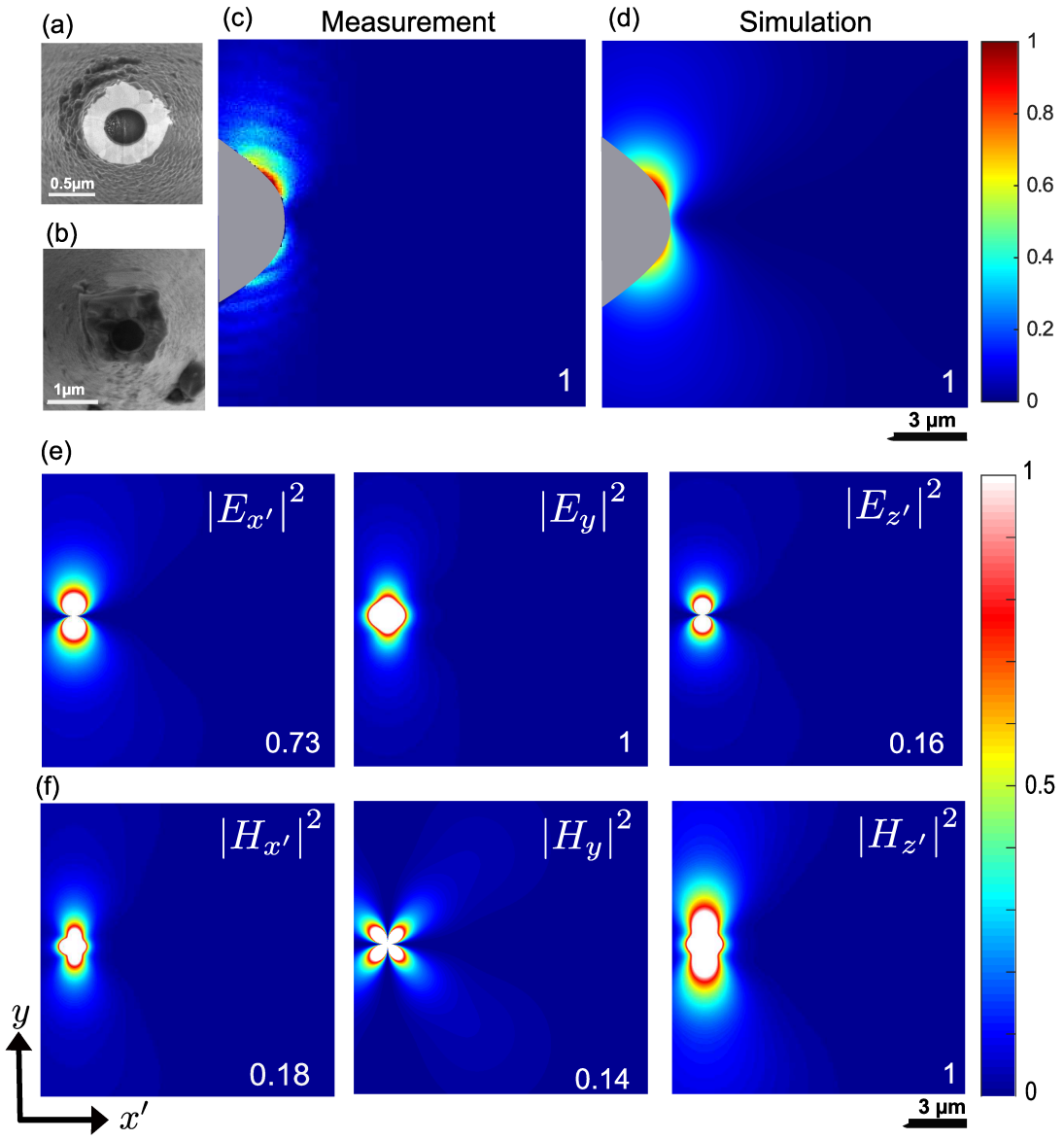

Figure 4.7: SEM images of the (a) excitation and (b) detection tips. (c) Measured near-field intensity pattern of the SPPs generated by the excitation aperture tip near a gold platelet. (d) Corresponding calculated magnetic field intensity (at a distance $z = 30$ nm from the air-gold interface) of the SPPs excited by a magnetic dipole with angles $\theta = 60°$ and $\varphi = 0°$. Numerical simulations of the (e) electric and (f) magnetic field intensity components corresponding to the near-field patterns of the excited SPPs. The number on the lower corners indicates the value of the normalized intensity in each panel. The simulated near-field patterns were calculated in the detection tip coordinates.

the induced dipole moments and, in turn, the electromagnetic field distribution below the aperture [111].

Previously, we explained that SPPs patterns mapped by the detection tip at an air-gold interface could be used to characterize a near-field angular distribution of the

electromagnetic field at the excitation aperture tip. In the near-field measurements to characterize the emission from different excitation tips, the polarization of light coupled to the end of the fiber tips was fixed. The mapped near-field intensities of SPPs excited by different aperture tips typically displayed three different angular patterns. Here, we explore three types of SPPs near-field patterns that were mapped employing different pairs of excitation and detection aperture tips. In doing so, the excitation aperture tip illuminated a monocrystalline gold platelet, with the thickness of 185 nm, at a wavelength of 1550 nm, while a thick polycrystalline gold film was used as a supporting substrate of the monocrystalline gold platelet.

Figures 4.7(a) and (b) are SEM images for the first pair of excitation and detection tips. The aperture plane of the excitation tip shows circular symmetry about the center of its aperture. Figures 4.7(c) and (d) are the mapped angular pattern of the SPPs and the corresponding numerically calculated total magnetic field intensity. The near-field pattern of the SPPs in Fig. 4.7(c) depicts two lobes indicating that the SPPs pattern is similar to the radiation of an in-plane or a tilted dipole. It is worth mentioning that electric or magnetic dipoles in free space have symmetric radiation patterns. However, the radiation pattern of a dipole placed close to an interface depends on its orientation. The radiation pattern of an out-of-plane dipole, i.e., perpendicular to the interface, is circularly symmetric about its origin, whereas an in-plane dipole, parallel to the interface, shows angular dependence (two lobes) [149].

It was shown that the Bethe-Bowkamp model is appropriate for describing the emission pattern from an excitation aperture tip as mapped by the detection tip. For a corresponding numerical simulation, a magnetic dipole with angles $\theta = 60^\circ$ and $\varphi = 0^\circ$ was located in a plane $z = 30$ nm above a gold platelet to consider the tilt of the aperture plane. We used FDTD Solver Lumerical to carry out the numerical calculations. The computation domain was selected as large as the scan area. Therefore, the effect of the gold platelet edges was not considered in the simulations. It should be noted that the angle θ is defined by an aperture plane tilt (Fig. 4.5), and φ is determined based on the orientation of the near-field SPP pattern. According to Fig. 4.6(a) and (c), the direction of a magnetic dipole is perpendicular to the orientation of the SPP near-field pattern. Fringes in the measured SPPs pattern are again due to the interference between excited SPPs at the aperture position and those reflected from the edges of the gold platelet.

The electromagnetic field components were calculated in the same plane $z = 30$ nm and, were rotated to the $x'yz'$ coordinate system to take into account the tilt of the

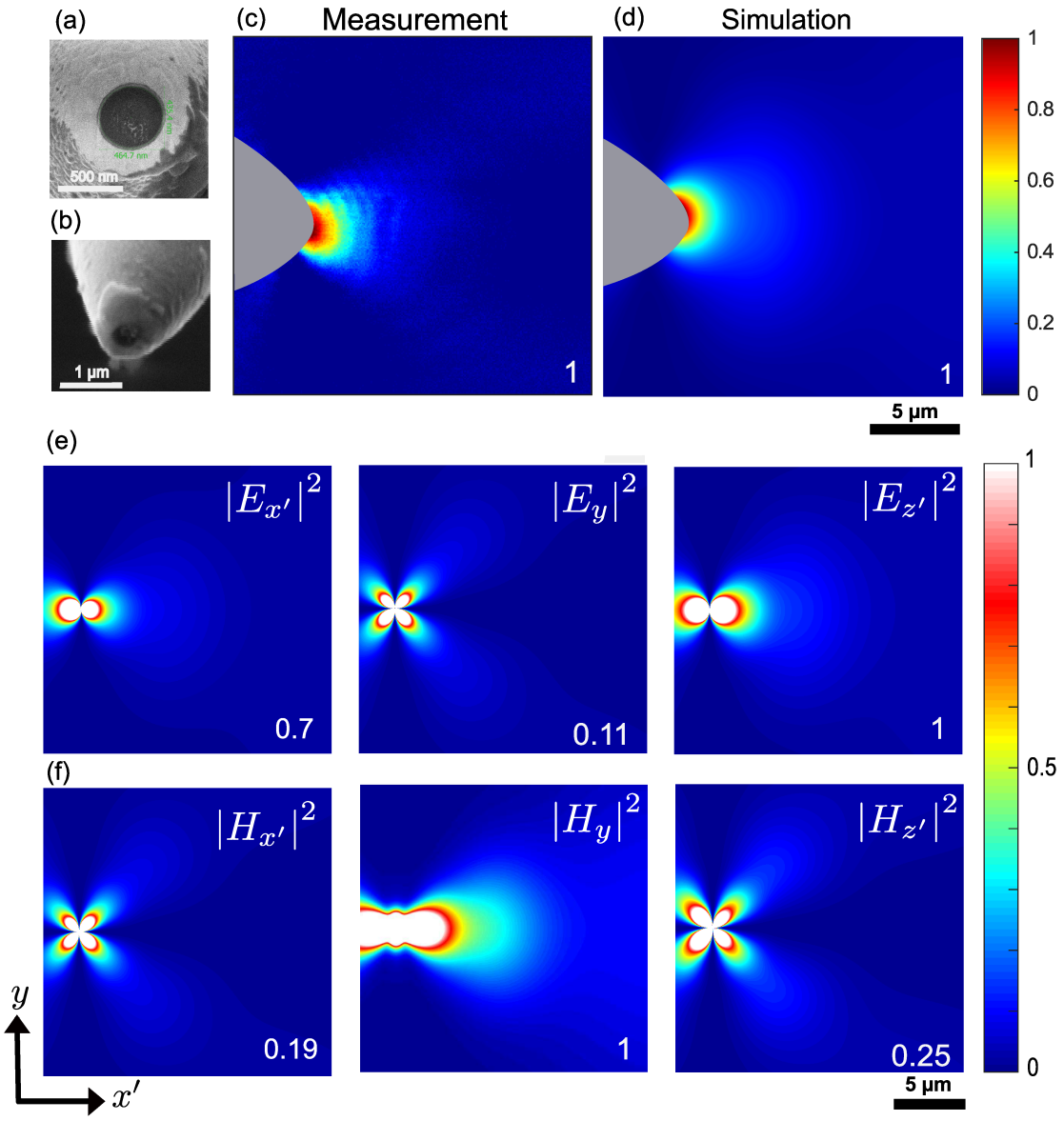

Figure 4.8: SEM images of the (a) excitation and (b) detection tips. (c) Measured near-field intensity pattern of the SPPs generated by the excitation aperture tip near a gold platelet. (d) Corresponding calculated magnetic field intensity (at a distance $z = 30$ nm from the air-gold interface) of the SPPs excited by a magnetic dipole with angles $\theta = 60°$ and $\varphi = 90°$. Numerical simulations of the (e) electric and (f) magnetic field intensity components corresponding to the near-field patterns of the excited SPPs. The number on the lower corners indicates the value of the normalized intensity in each panel. The simulated near-field patterns were calculated in the detection tip coordinates.

detection tip during the collection of the near-field optical signal. The corresponding intensity of electric and magnetic components in the $x'yz'$ coordinate are presented in Fig. 4.7(e) and (f). The total magnetic field intensity is shown in Fig. 4.7(d). Since the measured near-field pattern is similar to both total electric and magnetic

field intensities, it is not possible to argue if the aperture tip was more sensitive to an electric or magnetic dipole just according to the measured near-field pattern. Hence, regardless of the detection tip sensitivity to electric or magnetic field, the total intensity was calculated for the magnetic field $|\mathbf{H}|^2 = |H'_x|^2 + \left|H_y\right|^2 + |H_{z'}|^2$. An identical region to the avoidance area (gray parabolic region) was set to zero in Fig. 4.7(d). Excellent agreement is observed between the measured near-field pattern of SPPs in Fig. 4.7(c) excited by an aperture tip and the corresponding numerical result of total magnetic field intensity of SPP in Fig. 4.7(d).

Figures 4.8(a) and (b) demonstrate the SEM images of the second pair of excitation and detection tips. The aperture plane of the excitation tip shows almost circular symmetry around its center. Figure. 4.8(c) shows the measured near-field pattern of SPPs on the same gold platelet. In the measured near-field intensity, the orientation of the SPPs pattern is along the x-axis, indicating that the electric field with polarization along the x-axis reaches the aperture plane as it was shown in the numerical calculation for the truncated cone in Fig. 4.6(b). However, only one lobe of the SPP near-field pattern is visible, while the avoidance area covers another lobe. Since the input polarization of the beam coupled to the fiber end of the excitation tip did not change, the measured near-field pattern corroborates the fact that the geometry of the bent fiber determines the polarization of propagating modes inside the fiber after passing through the bend. Since fiber modes at the apex of the aperture tip become evanescent, they decay along the fiber and gold interface, resulting in plasmonic modes excited at the aperture.

Figure 4.8(d) exhibits the corresponding total magnetic intensity calculated in the coordinate of the detection tip $x'yz'$. The electromagnetic field components of SPPs were excited by a tilted magnetic dipole with angles $\theta = 60°$ and $\varphi = 90°$ on a plane 30 nm above the gold platelet. In Fig. 4.8(e) the electric field intensity component $|E_{z'}|^2$ makes the most contribution to the total electric field intensity. As a result, the intensity distribution of the total electric field is similar to $|E_{z'}|^2$. In Fig. 4.8(f) the intensity of magnetic field component $\left|H_y\right|^2$ determines the near-field pattern of SPPs mapped by the detection tip. Therefore, in Fig. 4.8(d), the total calculated magnetic field intensity demonstrates the similar near-field pattern as the magnetic field intensity $\left|H_y\right|^2$. For the third pair of excitation and detection tips in Fig. 4.9(a) and (b), the measured near-field angular pattern of SPPs in Fig. 4.9(c) varies from the SPPs patterns excited by an in-plane magnetic dipole. Taking only a tilted magnetic dipole can not describe a directional SPPs pattern. This directional pattern is

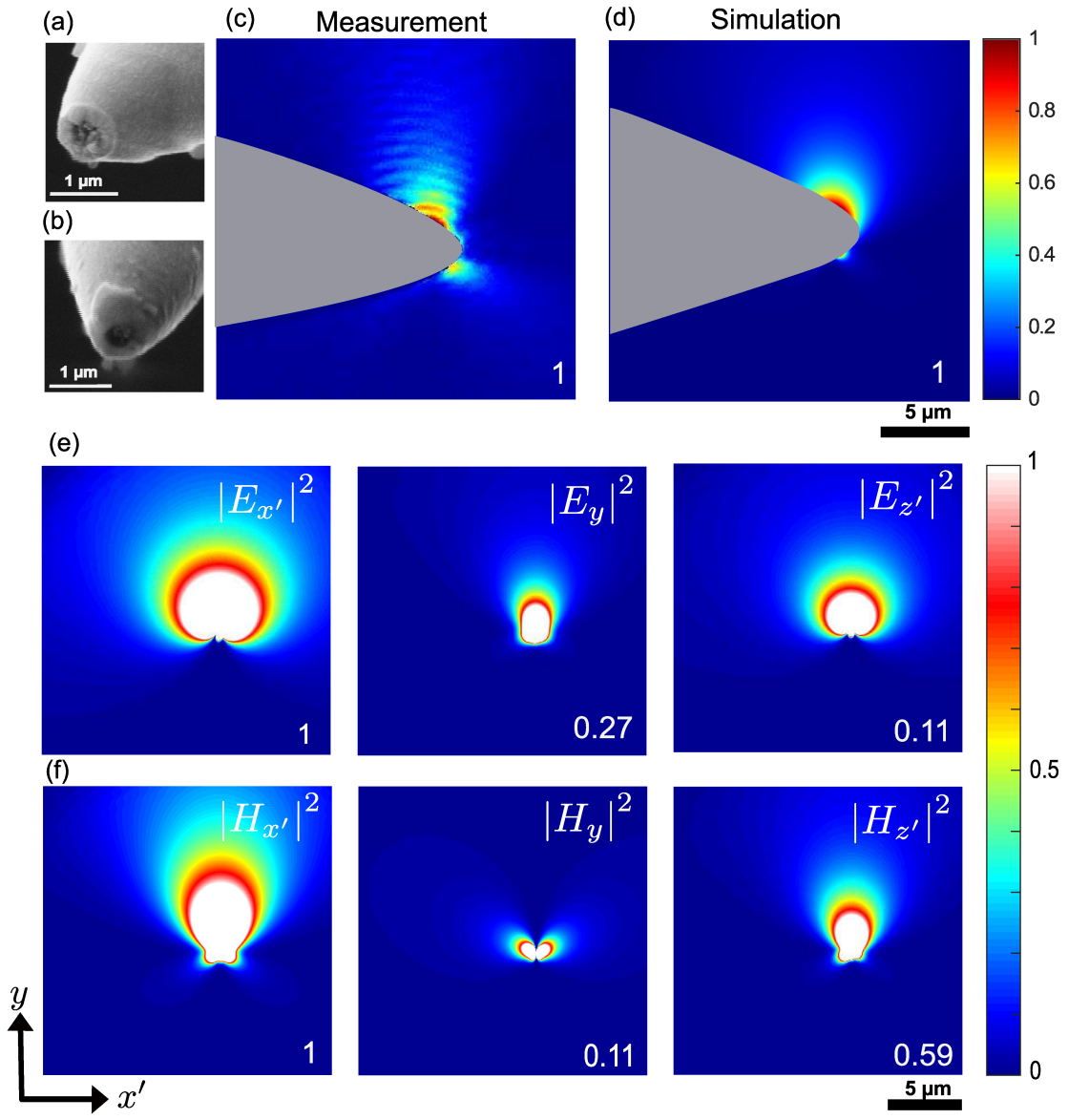

Figure 4.9: SEM images of the (a) excitation and (b) detection tips. (c) Measured near-field intensity pattern of the SPPs generated by the excitation aperture tip near a gold platelet. (d) Corresponding calculated magnetic field intensity (at a distance $z = 30$ nm from the air-gold interface) of the SPPs excited by a magnetic dipole with angles $(\theta_m = 60°, \varphi_m = 0°)$ and an electric dipole with angles $(\theta_e = 30°, \varphi_e = 180°)$. Numerical simulations of the (e) electric and (f) magnetic field intensity components corresponding to the near-field patterns of the excited SPPs. The number on the lower corners indicates the value of the normalized intensity in each panel. The simulated near-field patterns were calculated in the detection tip coordinates.

a characteristic of Kerker's condition and requires the interference of multiple multipoles [151, 152]. According to the first Kerker condition, if electric and magnetic dipoles are located in two planes perpendicular to each other, the interference of their electromagnetic field radiation leads to the suppression of backward scattering and

enhancement of forward scattering [26,153]. Furthermore, the Bethe-Boukamp model also describes the emission pattern for an oblique angle of the incident beam on the aperture in an infinite conducting plane by considering an out-of-plane electric dipole and an in-plane magnetic dipole at the center of the aperture [4]. In Fig. 4.5, it was shown that the tilt of the aperture plane would lead to an oblique angle of incidence relative to the normal to the aperture plane. For the case of the excitation aperture tip in Fig. 4.9(a), although the plane of the apex shows circular symmetry about the center of the aperture, the normal to the apex plane should have been tilted with respect to the fiber axis. This condition could be also compared with the oblique angle of incidence on a slit or a hole on a metallic film. It was shown that the relative phases of the electric and magnetic dipoles, which depends on the relative phases of incident beam and the polarizability of the illuminated geometry determines the asymmetric emission pattern and the corresponding directional SPP propagation [26,153].

In order to create the measured directional SPPs pattern, a magnetic dipole with angles $\theta_m = 60°$ and $\phi_m = 0°$, an electric dipole with angles $\theta_e = 30°$ and $\phi_e = 180°$ excited the SPPs at the aperture tip position. The polar angle θ_e of the electric dipole is determined according to the angle of the magnetic dipole θ_m since they should be perpendicular to each other. The orientation of a directional SPPs pattern corresponds to the azimuthal angle of the electric dipole ϕ_e. The azimuthal angle of the magnetic dipole ϕ_m should be perpendicular to SPPs directional pattern.

Figures 4.9(e) and (f) show the calculated electric and magnetic field components of SPPs. Since the electric and magnetic field components $|\mathrm{E}_{x'}|^2$ and $|H_{x'}|^2$ show higher maximum intensities, total electric and magnetic field intensity patterns are similar to the intensity patterns of $|E_{x'}|^2$ and $\left|H_{x'}^2\right|$. The measured intensity pattern in Fig. 4.9(c) is similar to the magnetic field intensity $\left|H_{x'}^2\right|$ and total magnetic field intensity in 4.9(d). Therefore, the measured near-field SPPs pattern implies that the detection tip was more sensitive to the magnetic fields.

The observed emission patterns from different bent aperture fiber tips corroborated the effects of a bend geometry and the apex geometry on the emission from the aperture. The good agreement between simulations and measurements suggest that the directional SPPs pattern depends on the tilt of the aperture plane with respect to the fiber axis. Therefore, the tilt angle of an aperture plane could be optimized to produce desired directional SPPs propagation. To the best of our knowledge, the measured near-field pattern, fulfilling the first Kerker condition, was the first observation of directional SPPs due to the emission from an aperture fiber tip.

5

Dipolar emission near the edge of a gold platelet

In the previous chapter, in order to characterize the emission pattern from aperture tips, the excitation tip excited the SPPs at the middle of a gold platelet far from its edges to avoid the effect of SPP scattering at edges [154,155]. So far, we have observed the effect of edges only as a modulation of the mapped near-field pattern due to the interference between excited SPPs at the position of the excitation aperture tip, and SPPs reflected from the edges. However, if the excitation aperture tip is close to the edge of a gold platelet, SPP edge diffraction is expected to be present [156].

Far-field illumination is typically used to excite the SPPs on the edge or corners of metallic surfaces to investigate the scattering or interference of the SPP waves [157, 158]. Therefore, the near-field pattern results from the interference between excited SPPs and the far-field illumination. The dual-tip SNOM provides an intriguing technique to study SPP dynamics. Thus far, the dual-tip SNOM was used to measure the near-field interference patterns of excited SPP on plasmonic waveguides [92–94]. Furthermore, a detection tip measured position-dependent near-field patterns of SPPs modes excited on a multimode plasmonic strip waveguide [96]. In previous studies, the detection tip could only scan a sample surface from the opposite direction of the excitation tip, whereas the area of a sample located on the left or right side of the excitation tip could not be measured in one scan. However, the detection tip of the automated dual-tip SNOM can measure the near-field optical response of almost the entire sample surface when the excitation tip is located near the edge or corner.

Different scanning microscopy techniques have been utilized to study SPP modes on the surface of gold platelets. One of the common techniques to study plasmonic

resonance modes for different shapes of gold platelets is a scanning transmission electron microscopy (STEM) in combination with an electron energy loss spectroscopy (EELS) [159–161]. Although this technique offers unprecedented spatial resolution due to the high energy of an electron beam in a vacuum, it is not practical as a characterization technique for on-chip hybrid systems composed of both dielectric and metallic nanostructures.

Scattering SNOM is another well-established microscopy technique that has been used to study SPP near-field pattern on the surface of gold platelets and other 2D materials [143, 162, 163]. Interference patterns of the SPP excited at the corner or next to the edge of a gold platelet are position and polarization-dependent. Changing the position or polarization of an incident beam can be utilized to excite particular SPPs modes and, in turn, different paths for SPP propagation [164]. In scattering SNOM, far-field illumination is used to excite the SPPs. To this end, a sharp tip acts as an electric dipole, exciting SPP point source on the surface of a gold platelet. Electromagnetic fields that are scattered by a sharp tip contain high spatial frequency components that match the wave vector of surface plasmons and enable the excitation of SPPs. [165]. Nevertheless, the far-field illumination always interferes with excited SPPs in the near field, obscuring a near-field pattern due to merely SPP waves interference [157, 158]. A dual-tip SNOM allows point-source excitation at the desired location on a sample eliminating the effect of the far-field illumination on a measured SPP near-field pattern.

This chapter presents the result of the interference pattern of SPPs on a gold platelet due to a dipolar emission from the excitation tip near the edge of a gold platelet. The image dipole method is used to analytically calculate the interference pattern of SPPs on the gold platelet. The corresponding numerical calculation also confirms the accuracy of the image dipole method for calculating a near-field pattern measured by the dual-tip SNOM on planar geometries.[1]

5.1 Dipolar emission at an air-metal interface

Figure 5.1(a) shows an electric dipole $\mathbf{p} = (p_x, p_y, p_z)$, located at distance $z = d$ from a dielectric-gold interface, oscillating with a constant frequency ω which gives rise to an electric field distribution $\mathbf{E}$. The electric field expressed in a cylindrical basis

[1]The results of this chapter have been published in [166].

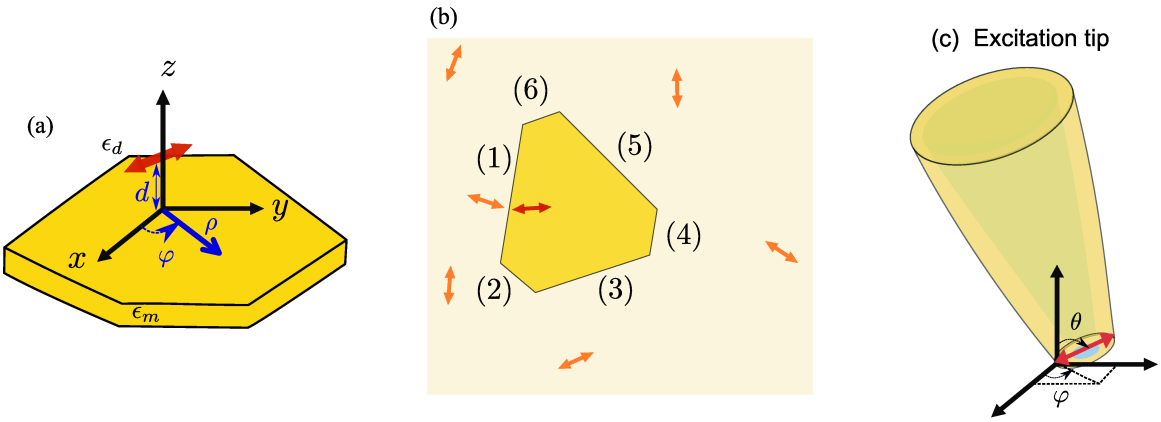

Figure 5.1: (a) Coordinate of a dipole emission above the gold platelet at a height $z = d$. Red double arrow represents an electric dipole. The radial position of the excited SPPs is ρ, and their angular dependence is indicated by φ. (b) Schematic of a image dipole method. The red double arrow shows the position of the in-plane original dipole (emission from the excitation tip) and its orientation. The orange double arrows are images of the original dipole relative to the gold platelet edges. (c) Angles θ and φ of a magnetic dipole that mimics the emission from the excitation aperture tip used in the numerical simulation.

(E_ρ, E_φ, E_z), can be written as [149, 167],

$$\mathbf{E} = 2\,\mathrm{Re}[\frac{\exp(ik_{\mathrm{SPP}}\rho)}{\sqrt{k_{\mathrm{SPP}}\rho}}\exp\big(ik_{z,d}z\big)\exp\big(ik_{z,d}\mathrm{d}\big)\exp(-i\omega t)] \\ \mathrm{M}\vec{v}[p_x\cos\varphi + p_y\sin\varphi + p_z\frac{k_{\mathrm{SPP}}}{k_{z,d}}], \tag{5.1}$$

where $k_{\mathrm{SPP}} = \frac{2\pi}{\lambda_0}\sqrt{\frac{\epsilon_d\epsilon_m}{\epsilon_d+\epsilon_m}}$ is the propagation constant of SPPs with the radiation wavelength λ_0 in free space. The wave vector in vacuum is $k_0 = \frac{2\pi}{\lambda_0}$ and the dielectric constants of the metal and the dielectric correspond to ϵ_m and ϵ_d, respectively. Constants ${k_{z,d}}^2 = {k_0}^2\epsilon_d - {k_{\mathrm{SPP}}}^2$ and ${k_{z,m}}^2 = {k_0}^2\epsilon_m - {k_{\mathrm{SPP}}}^2$ indicating the exponential decay of SPPs from an interface into the dielectric and metal. The constant $\mathrm{M} = -\frac{1}{2}(\frac{k_{z,d}k_{z,m}}{\sqrt{2\pi}\epsilon_0})(\frac{k_{z,d}\epsilon_m - k_{z,m}\epsilon_d}{{\epsilon_d}^2-{\epsilon_m}^2})e^{(-i\pi/4)}$ is called coupling coefficient [149]. The vector $\vec{v} = \hat{\rho} - (\frac{k_{\mathrm{spp}}}{k_{z,d}})\hat{z}$ denotes the polarization of SPP waves.

Figure 5.1(a) shows an oscillating dipole (red double arrow) that is located above the gold platelet at a distance $z = \mathrm{d}$. The angular dependence of SPPs propagation on the xy plane is determined by the angle φ.

The analytical approach based on the image dipole method was proposed to calculate the emission pattern due to excited SPPs by a dipole on planar geometries with edges [168]. In the proposed image dipole method, the SPPs reflected from edges can be substituted by SPPs originating from image dipoles. The positions of the image dipoles are calculated by mirroring the original dipole over all edges. It should be

noted that the second-order images of the image dipoles have been neglected due to the short propagation length of SPPs, leading to their quick decay before multiple reflections from edges.

Figure 5.1(b) illustrates an in-plane electric dipole (red double arrow) and its image dipoles (orange double arrows) relative to the edges of a hexagon-like gold platelet. The position of the original dipole corresponds to the aperture position of the excitation tip of the dual-tip SNOM (Fig. 5.3). The edge next to the excitation tip is numbered (1). The electric field intensity distribution on a plane $z = \mathrm{d}$ above the air-gold interface is calculated using Eq. (5.1). The electric field intensity of SPPs is the result of the interference between the electric field of SPPs generated by the original dipole $\mathbf{p}_0$ and six image dipoles $\mathbf{p}_{1-6}$, is given by,

$$|\mathbf{E}|^2 = C\left|\sum_{n=0}^{6}\frac{\exp(ik_{\mathrm{SPP}}\rho_n)}{\sqrt{k_{\mathrm{SPP}}\rho_n}}\left(p_{(\mathrm{x,n})}\cos\varphi_n + p_{(\mathrm{y,n})}\sin\varphi_n + p_{(z,n)}\right)\left(\frac{k_{\mathrm{SPP}}}{k_{z,d}}\right)\right|^2 \qquad (5.2)$$

where $C = \left|\mathrm{M}\vec{v}\exp\left(2ik_{z,1}d\right)\exp(i\omega t)\right|^2$ and n is the number of the dipoles in the calculations. The vector components of the image dipoles, $p_{(x,n)}$, $p_{(y,n)}$, $p_{(z,n)}$ can be expressed as, $\mathbf{p}_n = \mathbf{p}_0\Gamma\exp(i\delta)$, where Γ is the reflection coefficient of the metal edge and δ is the phase shift between the excited and reflected SPPs. The reflection coefficient and the phase shift should be taken into account since the amplitude and phase of the reflected SPPs change upon the reflection and depend on the dielectric constant of the gold platelet, the surrounding medium, and the incidence angle with which they hit the edges [169]. For normal incidence of the SPPs upon the edges of the gold platelet the reflection coefficient and and the phase shift are $\Gamma = 0.15$ $\delta = 0.35\pi$ respectively [168].

5.2 SPP excitation near the edge of a gold platelet

For a dual-tip SNOM measurement near the edge of a planar geometry, a monocrystalline gold platelet with the thickness of 185 nm with a supporting substrate of polycrystalline gold film with the thickness of 220 nm was used. The excitation tip illuminated the gold platelet at distance about 1 µm away from its edge at a wavelength of $\lambda_0 = 1550$ nm. The artistic view of the dual-tip SNOM configuration is shown in Fig. 5.2. The detection tip automatically maps the near-field pattern of SPPs around the excitation tip over entire area of the gold platelet without any collisions.

Figure 5.3(a) shows the SEM image of the measured monocrystalline gold platelet. Figure 5.3(b) depicts the measured near-field pattern of SPPs by the detection tip.

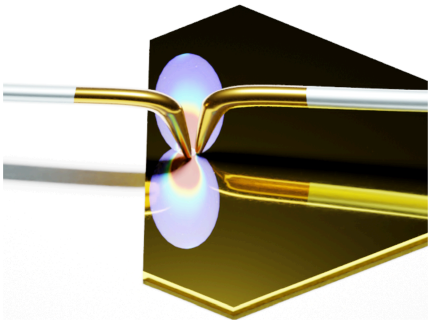

Figure 5.2: Artistic view of excitation and detection aperture fiber tips near the edge of a gold platelet.

When SPPs reach the edges of the gold platelet, they either reflect or scatter to the free space. The interference of the reflected SPPs from the edges with the excited SPPs at the aperture position results in the measured near-field interference pattern. In particular, we can see that the dipolar emission from the excitation aperture near the edge (1) (See Fig. 5.1(b)) leads to the strong intensity along the edge. The edge enhancement of the SPPs was also observed by leakage radiation microscopy [156]. The other edges also show slight enhancement of the near-field intensity, although the SPP waves decays along the propagation direction. This observation can be attributed to the nanoscale lightening rod effect, i.e., the strong electrical potential gradient due to the small surface curvature at the edges [170]. Adjusting the position of the excitation source can be used to alter the near-field pattern and SPP propagation direction [157].

To gain more insights into the measured near-field pattern, we have compared it with numerical simulations and the analytical model introduced in the previous Section. For the simulations, the near-field intensity distribution of the magnetic field, due to a magnetic dipole excitation with azimuthal angle $\varphi = 15°$ and polar angle $\theta = 60°$ (Fig. 5.1(c)), was calculated on a plane 30 nm above the gold platelet using FDTD Solver Lumerical. The angle φ of the magnetic dipole in the simulation and the electric dipole in analytical model was chosen according to the orientation of the SPP pattern of the measured near-field, whereas the angle θ is determined based on the bend angle of the excitation aperture tip. It must be noted that, due to the duality of electric and magnetic fields near planar surfaces, the calculated electric field intensity due to the electric dipole excitation shows a similar field distribution as a calculated magnetic field intensity due to a magnetic dipole excitation [4]. For that reason, we can compare the intensity field distribution of the magnetic field from the numerical

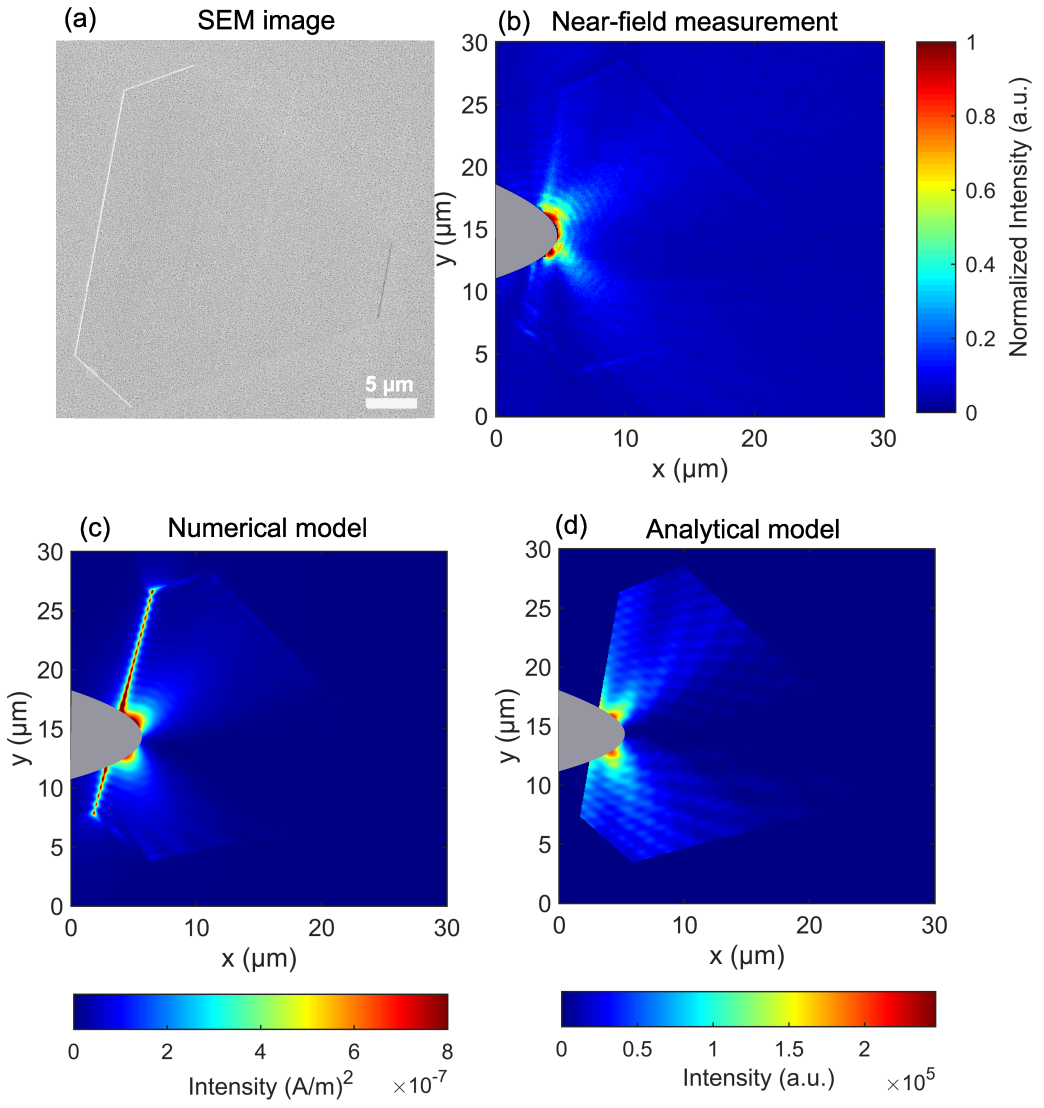

Figure 5.3: (a) SEM image of the measured monocrytalline gold platelet. (b) Measured near-field intensity pattern of SPPs by dual-tip SNOM. (c) Corresponding numerical simulation of the magnetic field intensity pattern due to a magnetic dipole representing the emission from the excitation aperture tip. (d) Analytically calculated electric field intensity of SPPs using the image dipole method. The gray parabolic regions are avoidance areas.

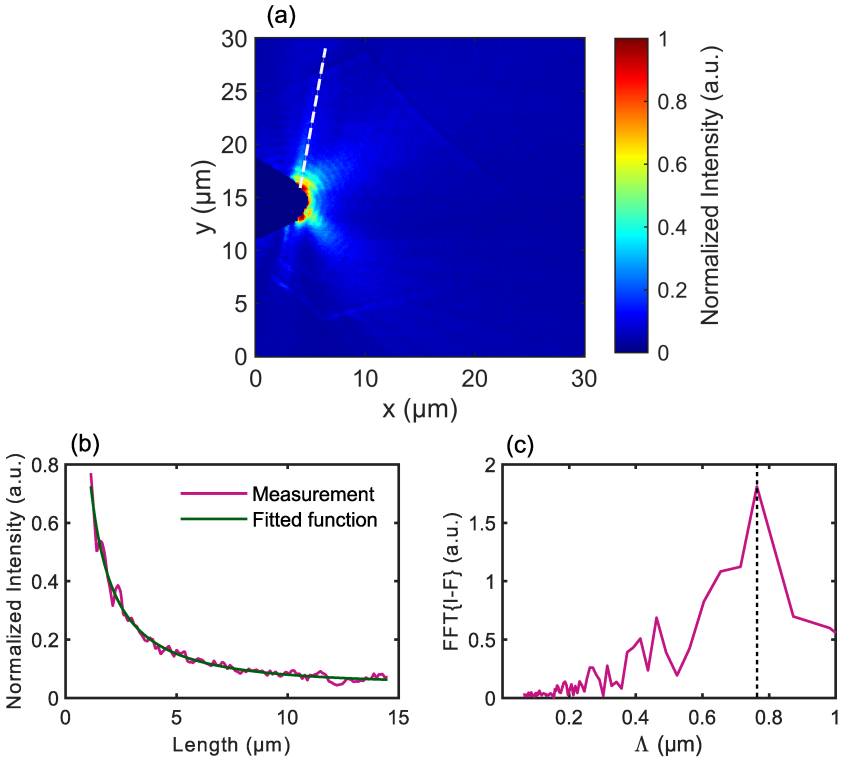

Figure 5.4: (a) Intensity line profile along the edge of the gold platelet selected from the measured near-field intensity pattern of SPPs. (b) The intensity line profile (I) was fitted to $F = \frac{1}{\rho}\exp\big(-2\,\mathrm{Im}\{k_{\mathrm{SPP}}\}\rho\big)$. (b) Fourier transform of the intensity line profile in (b) calculated after subtraction from the fitted function ($I - F$). The maximum of the Fourier transform corresponds to the half of the wavelenght of the SPPs $\Lambda = 0.77$ µm.

calculation with analytically calculated electric field. Figures 5.3(c) and (d) visualize the numerically calculated magnetic field intensity and the analytically calculated electric field intensity, respectively. The agreement between the measured near-field pattern of SPPs with the simulation result and with the analytical model supports our previous assumptions. Therefore, the image dipole method can be used to analytically calculate the electromagnetic field due to a dipole excitation on relatively large planar geometries instead of computationally demanding numerical calculations.

Since no far-field illumination is involved, the dual-tip SNOM measurements ensure that the measured near-field intensity is only the result of the excited SPPs. Therefore, the periodicity of the fringes in the interference pattern should correspond to $\lambda_{\mathrm{SPP}}/2$, when λ_{SPP} is the wavelength of the excited SPPs. Hence, it is possible to extract the wavelength of the SPPs from the measured near-field pattern. In doing so, an intensity line profile is extracted from the measured near-field intensity in Fig. 5.4(a). The intensity line profile is fitted to $\mathrm{F} = \frac{1}{\rho}\exp\big(-2\,\mathrm{Im}\{k_{\mathrm{SPP}}\}\rho\big)$.

To find the periodicity of the interference fringes corresponding to $\lambda_{\mathrm{SPP}}/2$, the fitted exponential function (F) was subtracted from the line intensity profile (I). Then its Fourier transform was calculated [143]. The reason for subtracting the exponential function from the measured intensity is to separate two different parts of the signal containing both exponential decay and oscillatory behavior of the SPP propagation related to the modulation of SPPs standing wave. The peak of the Fourier transform is attained at $\Lambda = 0.77$ µm, resulting in the SPPs wavelength $\lambda_{\mathrm{SPP}} = 1.54$ µm. Moreover, from dispersion relation $k_{\mathrm{SPP}} = \frac{2\pi}{\lambda_0}\sqrt{\frac{\epsilon_d \epsilon_m}{\epsilon_d + \epsilon_m}}$, at the excitation wavelength $\lambda_0 = 1.55$ µm for the dielectric constant of gold $\epsilon_m = -115.13 + 11.25i$, the value of the SPPs wavelength is $\lambda_{\mathrm{SPP}} = 1.54$ µm, which indicates the excellent agreement with the value extracted from the measurements.

In summary, it was shown that the dual-tip SNOM allows near-field excitation and detection of the SPPs on the edge or the corner of plasmonic waveguides. The image dipole model is indeed a proper model to calculate the interference pattern due to the dipole excitation near a planar geometries with edges. The results of this chapter demonstrated the unprecedented capability of the dual-tip SNOM to explore the edge effects in plasmonics and dielectric nanophotonic systems.

6

Dipolar emission near a dielectric metasurface

The dual-tip SNOM setup has been used typically to map guided plasmonic modes sustained by flat or unstructured metallic surfaces [96, 97, 171, 172]. In the previous chapters, the automated dual-tip SNOM was also utilized to map SPP patterns due to the emission from the excitation tip near a planer gold platelet. Although planar waveguides are fundamental components for guiding light, the efficient harnessing of light for different applications requires nanostructured materials. Modern fabrication techniques have made it possible to engineer three-dimensional nanostructures called metamaterials to manipulate subwavelength light-matter interactions [173]. Potential applications, however, are hampered by the complex fabrication process of three-dimensional geometries. However, the reduced dimensionality of metamaterials leads to metasurfaces that are planar arrays of subwavelength nanoantennas. Metasurfaces can substitute bulky optical devices in response to the demand for miniaturization. They are promising platforms for on-chip nanophotonics because of their well-established fabrication process and exceptional abilities to manipulate the amplitude, phase, and polarization of light at nanoscales [174–177]. According to the material they are made of, metasurfaces can be classified as plasmonic or dielectric. Although plasmonic metasurfaces have enabled many optical functionalities [178], their applications are limited due to dissipative losses at optical frequencies.

In plasmonic metasurfaces, inside the nanoantenna the electric and magnetic fields are vanished. On the other hand, inside the dielectric nanoantennas, the incoming oscillating incident light produces a circular displacement current, resulting in a strong magnetic resonance. Nanoantennas of higher refractive index materials, as a building block of dielectric metasurfaces, enable magnetic or electric Mie resonances based on displacement currents [179].

One of the promising applications of metasurfaces is to be a host medium for quantum emitters to enhance their radiated power in order to realize single-photon sources [56, 180]. The radiated power by quantum emitters depends on the emission frequency and their position with respect to a metasurface. The transition dipole moment mimics a classical point dipole oscillation when it interacts with a host medium [64]. In Chapter 4, it was shown that the emission from an aperture tip could also be described with a classical dipole model. When excited modes by a dipolar emission are not guided, they are mostly confined around the excitation position and decay fast. Even if the near-field optical response is confined around the excitation tip position, the automated dual-tip SNOM enables the measurements of the position- and frequency-dependent near-field pattern due to a dipolar emission near desired photonic systems.

In this chapter, the automated dual-tip SNOM was used to study the spatial and spectral response of silicon nanodisk metasurfaces when they are excited in the near field by a dipolar emission from the excitation tip. To understand the underlying physics of this interaction, in Section 6.1, the definition of partial LDOS and its relation with the measured near-field intensity will be explained. Section 6.2 presents the measured near-field patterns for spectral and spatial tuning of the emission from the excitation tip near a silicon nanodisk metasurface. The near-field measurement results, and their corresponding numerical simulations are discussed. In Section 6.3, the relation between the integrated mapped near-field intensity and the enhancement of the radiated power by a dipole in the near field (partial LDOS) is investigated [1]

6.1 Partial local density of optical states

The interaction of quantum emitters as near-field sources with nanostructures and the amount of radiated power is governed by the local density of optical states (LDOS) [4]. For a particular dipole moment orientation, partial LDOS quantifies the number of excitable electromagnetic modes. If partial LDOS is averaged over all orientations of dipole moments, LDOS is obtained [42]. In other words, if a dipole moment randomly oscillates in all directions of space (have no fixed dipole moment orientation), LDOS should be taken into account.

When a dipole is oriented along a unit vector $\mathbf{n}_\alpha$, $\alpha = x, y, z$, its coupling mechanism is quantified by the partial LDOS. Quantum emitters may possess both electric

[1] Parts of the results of this chapter have been published in [181].

and magnetic dipole transitions. For most quantum emitters, electric dipole transitions are dominant. However, magnetic dipoles are dominant transitions for some types of quantum emitters. As a result, for such quantum emitters, both electric and magnetic dipole transitions should be considered to calculate the total partial LDOS. The electric ρ_e and magnetic ρ_m partial LDOS are defined as [182],

$$\rho_e(\mathbf{r}_0,\omega) = \frac{2\omega}{\pi c^2}\left[\mathbf{n}_\alpha \cdot \mathrm{Im}\Big\{\overleftrightarrow{\mathbf{G}_e}\Big\}(\mathbf{r}_0,\mathbf{r}_0;\omega)\cdot\mathbf{n}_\alpha\right], \tag{6.1}$$

$$\rho_m(\mathbf{r}_0,\omega) = \frac{2\omega}{\pi c^2}\left[\mathbf{n}_\alpha \cdot \mathrm{Im}\Big\{\overleftrightarrow{\mathbf{G}_m}\Big\}(\mathbf{r}_0,\mathbf{r}_0;\omega)\cdot\mathbf{n}_\alpha\right], \tag{6.2}$$

here $\mathbf{r}_0$ is a dipole position with oscillation frequency ω. The speed of light in free space is denoted by c. The imaginary part of the dyadic Green's function $\mathrm{Im}\Big\{\overleftrightarrow{\mathbf{G}}\Big\}$ is a linear response function at position $\mathbf{r}$ due to a dipole excitation at position $\mathbf{r}_0$. The first, second, and third columns of $\overleftrightarrow{\mathbf{G}}$ correspond to the electromagnetic fields of a dipole oriented along the x-, y- or z-axis, respectively. According to Eqs. (6.1) and (6.2), the electric and magnetic partial LDOS can be determined by the imaginary part of electric and magnetic Green's functions.

The partial LDOS also determines if the radiated power by a dipole is enhanced or suppressed when placed in a medium. In a weak coupling regime, the enhancement of dipole radiation power $\frac{P}{P_0}$ in the classical picture is the same as the enhancement of the decay rate $\frac{\gamma}{\gamma_0}$ of two-level quantum emitters and is given by [4],

$$\frac{\gamma}{\gamma_0} = \frac{P}{P_0} = \frac{6\pi \mathrm{c}}{\omega}\left[\mathbf{n}_\alpha \cdot \mathrm{Im}\Big\{\overleftrightarrow{\mathbf{G}}(\mathbf{r_d},\mathbf{r_d};\omega)\Big\}\cdot\mathbf{n}_\alpha\right]. \tag{6.3}$$

γ_0 and P_0 are respectively the spontaneous decay rate and the power emitted by the dipole in a homogeneous medium. It can be observed from Eq. (6.3) that the decay rate enhancement or power enhancement known as Purcell factor are proportional to the partial LDOS at the position of a quantum emitter [183]. Moreover, the partial LDOS and the Purcell factor are determined by the imaginary part of the Green's function. In this regard, if a photonic system has no dissipation, the imaginary part of the Green function can be described as a superposition of normal modes. For instance, the imaginary part of the magnetic Green's function due to a magnetic dipole transition takes the form [4],

$$\mathrm{Im}\Big\{\overleftrightarrow{\mathbf{G}_m}(\mathbf{r}_0,\mathbf{r}_0,\omega)\Big\} = \frac{\pi c^2}{2\omega}\sum_n \mathbf{H}^*{}_n(\mathbf{r}_0,\omega)\mathbf{H}_n(\mathbf{r}_0,\omega), \tag{6.4}$$

where $\mathbf{H}_n(\mathbf{r}_0,\omega)$ indicates the nth excited magnetic mode at the position $\mathbf{r}_0$. Given that the modes of a photonic system are orthogonal, according to Eqs. (6.2) and (6.4) a magnetic partial LDOS is defined as,

$$\rho_m(\mathbf{r}_0,\omega) = \sum_n [\mathbf{n}_\alpha.\mathbf{H}_n^*(\mathbf{r}_0,\omega)\mathbf{H}_n(\mathbf{r}_0,\omega).\mathbf{n}_\alpha]. \tag{6.5}$$

The magnetic dipole oriented along the x-axis can be assumed to understand the relation between the measured near-field intensity and the partial LDOS. The partial magnetic LDOS $\rho_{mx}(\mathbf{r}_0,\omega)$ of a photonic system at position r_0 and excitation frequency ω can be written as [42],

$$\rho_{mx}(\mathbf{r}_0,\omega) = \sum_n |\mathrm{H}_{xn}(\mathbf{r}_0,\omega)|^2. \tag{6.6}$$

According to Eq. (6.6), for the magnetic dipole oriented along the x axis, the partial magnetic LDOS ρ_{mx} is determined by the superposition of the magnetic field intensity $\mathrm{H_x}$ of all n modes available at the position of a dipole excitation.

Since the emission from the excitation tip mimics the radiation of an in-plane magnetic dipole at a particular emission wavelength, all available modes should be excited. If the detection tip is sensitive to magnetic fields, the corresponding detected signal should be related to the partial magnetic LDOS according to Eq. (6.6). Therefore, the partial LDOS is relevant for analyzing mapped near-field intensities using the dual-tip SNOM.

Based on Eq. (6.3), the enhancement of the radiated power by a dipole is calculated for a volume surrounding the dipole and the sample. However, the measured near-field intensity by the detection tip allows access only to the power in the plane parallel to the sample surface. Both Eqs. (6.3) and (6.6) are proportional to partial LDOS. Thus, it is expected that the power enhancement of a dipole and the integrated mapped intensities measured in the near-field of the metasurface follow the same trend of behavior which is investigated in Section 6.3.

6.2 Spatial and spectral near-field measurements near a metasurface

In the previous section, we have seen that the partial LDOS, a characteristic of photonic systems, is frequency and position-dependent. In practice, the map of partial LDOS provides information about a frequency or a position where the radiated power by a quantum emitter is enhanced. Measurements of LDOS or spontaneous decay rate of quantum emitters have been performed with different microscopy techniques [31,45,184,185]. The most conventional technique to map LDOS was developed by integrating fluorescence lifetime imaging with a scanning probe optical microscope where a fluorescence molecule was attached to the extremity of a tip [31]. In this

technique, the emitter lifetime, which is inversely proportional to LDOS, is mapped as a function of its position relative to a nanostructure [32, 55, 186].

Scanning near-field optical microscopy (SNOM) was the first proposed technique to measure the LDOS. The capability of the SNOM to map the partial LDOS was demonstrated theoretically and experimentally [43, 45, 187]. If the illumination mode SNOM is used to measure the partial LDOS, the details of partial LDOS maps are determined by the amount of evanescent waves collected in the far field depending on a collection angle of an objective [44]. However, the partial LDOS was mapped using a particular configuration of an illumination SNOM, the so-called forbidden light SNOM [188]. In the forbidden light SNOM, propagating components of the electromagnetic fields are filtered, and the evanescent waves are converted into traveling waves detected in the far field below a sample [45], similar to a leakage radiation microscopy [136]. In the forbidden light SNOM, evanescent waves are collected only in half-space beneath the sample. In contrast to the forbidden light SNOM, the detection tip of the dual-tip SNOM can directly map the evanescent waves in the near-field of a sample. Thus, changes of an integrated measured near-field intensity are also expected to be consistent with the modification of partial LDOS at different excitation aperture tip positions. None of the mentioned measurement techniques can provide information regarding the spatial distribution of electromagnetic fields in the near field when a single emitter interacts with nanostructures. Here, the results of the position- and wavelength-dependent near-field intensity patterns due to the dipolar emission from the excitation tip near the silicon metasurface are presented. According to Eq. (6.3), the transition frequency or the position of a quantum emitter relative to a metasurface affects the number of excited modes and, in turn, the electromagnetic field distribution in the near-field of a metasurface. Figure 6.1 demonstrates the artistic view of the excitation and detection tips on a nanodisk silicon metasurface. The metasurface was excited at different illumination wavelengths for frequency-dependent near-field measurements. The excitation tip position relative to the metasurface was fixed. During position-dependent measurements, the illumination wavelength of the excitation tip remained constant, while the position of the excitation tip relative to the metasurface was changed.

6.2.1 Near-field pattern spectral dependence

Silicon nanodisks are regarded as promising building blocks of dielectric metasurfaces. Tailoring the geometrical parameters of silicon nanodisks including diameter [189],

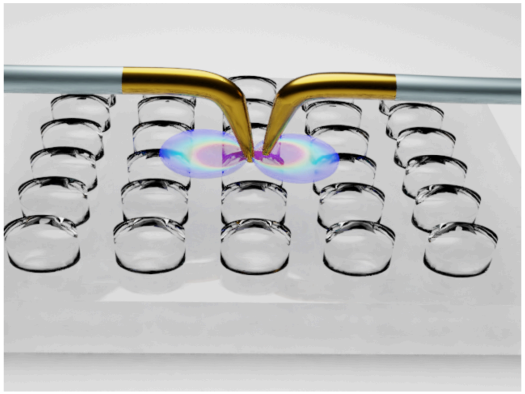

Figure 6.1: Artistic view of the near-field measurement of a silicon nanodisk metasurface using the dual-tip SNOM.

height [190] and their arrangement [191] gives rise to different electric dipole (ED) and magnetic dipole (MD) resonances frequencies. A dielectric sphere is the only geometry for which the resonance modes can be calculated analytically [192]. For numerical calculations the FDTD Solver Lumerical was used to optimize the geometry parameters of a nanodisk, including the diameter, height, and lattice constant, such that the transmission spectrum of the metasurface exhibits ED and MD resonances in the wavelengths range of $1.4 - 1.65$ µm.

The frequency-dependent near-field measurements were performed for a metasurface, showing the magnetic dipole resonance at a wavelength $\lambda_0 = 1.6$ µm. The metasurface was composed of nanodisk arrays with a radius $r = 325$ nm, a height of $H = 235$ nm and a lattice constant $L = 1020$ nm in a cubic lattice (See Fig. 6.2(c)).

Before performing the frequency-dependent near-field measurements, the transmittance spectrum of the metasurface for normally incident light was measured in a far-field spectroscopy setup. Figure 6.2(a) depicts both measured and computed transmittance spectra of the metasurface which are in very good agreement. A small difference between the minimum value of the transmittance spectra originates from imperfections imposed during the fabrication process. The minimum transmittance corresponds to the MD resonance wavelength $\lambda = 1.6$ µm. Figure 6.2(b) presents the in-plane components of the electric and magnetic intensities calculated on a plane above a nanodisk when illuminated from below with the y-polarized plane wave. Since the detection tip mostly collects in-plane electromagnetic fields, only the in-plane intensity components are shown in a plane $z = 20$ nm above the nanodisk. Figures 6.2(c-d) depict the SEM images of the silicon nanodisk metasurface, excitation, and detection tips utilized in spectral-dependent near-field measurements.

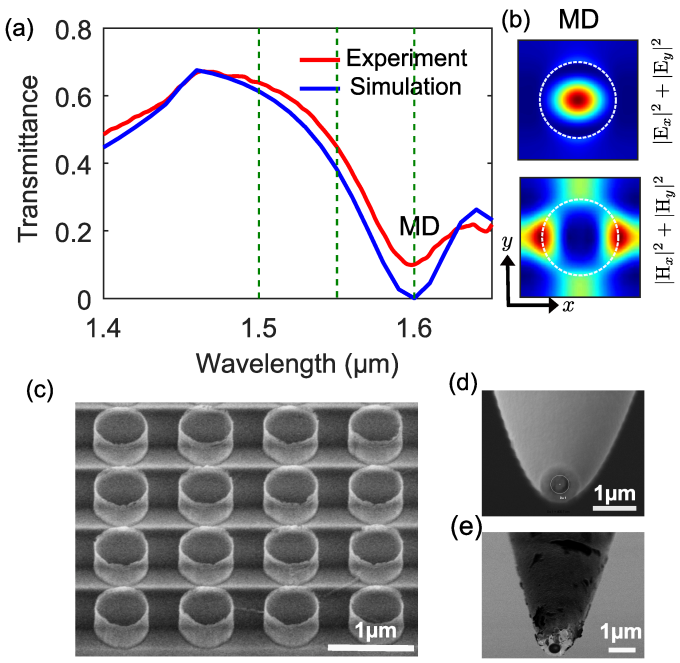

Figure 6.2: (a) Transmittance spectrum of the silicon nanodisk metasurface used in spectral dependence near-field measurement. Green dashed lines denote the excitation wavelengths in the near-field measurements. Only the magnetic dipole resonance (MD) is observed within the range of the measured wavelengths. (b) In-plane components of the electric and magnetic intensity calculated for one lattice constant when it was illuminated by y-polarized plane wave at the MD resonance wavelength. SEM images of (c) the metasurface, (d) excitation tip, and (e) detection tip used in the spectral-dependent near-field measurements.

During the experiment, the excitation tip and the metasurface were stationary. The detection tip mapped the near-field intensity distribution for three different excitation wavelengths shown by green dashed lines in Fig. 6.2(a). Figure 6.3(a) displays the measured near-field intensity by the detection tip at illumination wavelengths written on top of each panel.

For the respective numerical simulations in Fig. 6.3(b), the magnetic dipole oriented along the y-axis was located in the plane $z = 20$ nm above the metasurface at the position of the aperture tip's center. A perfectly matched layer (PML) truncated the computational region to minimize the reflections of the incident light from the boundaries. The in-plane components of the electric field intensity were calculated in the same plane as an excitation dipole. The intensity values corresponding to the avoidance area (gray region) were set to zero to compare the simulations with measured near-field intensities. The electric field intensities were calculated in numerical simulation because the detection tip is expected to show higher sensitivity to electric

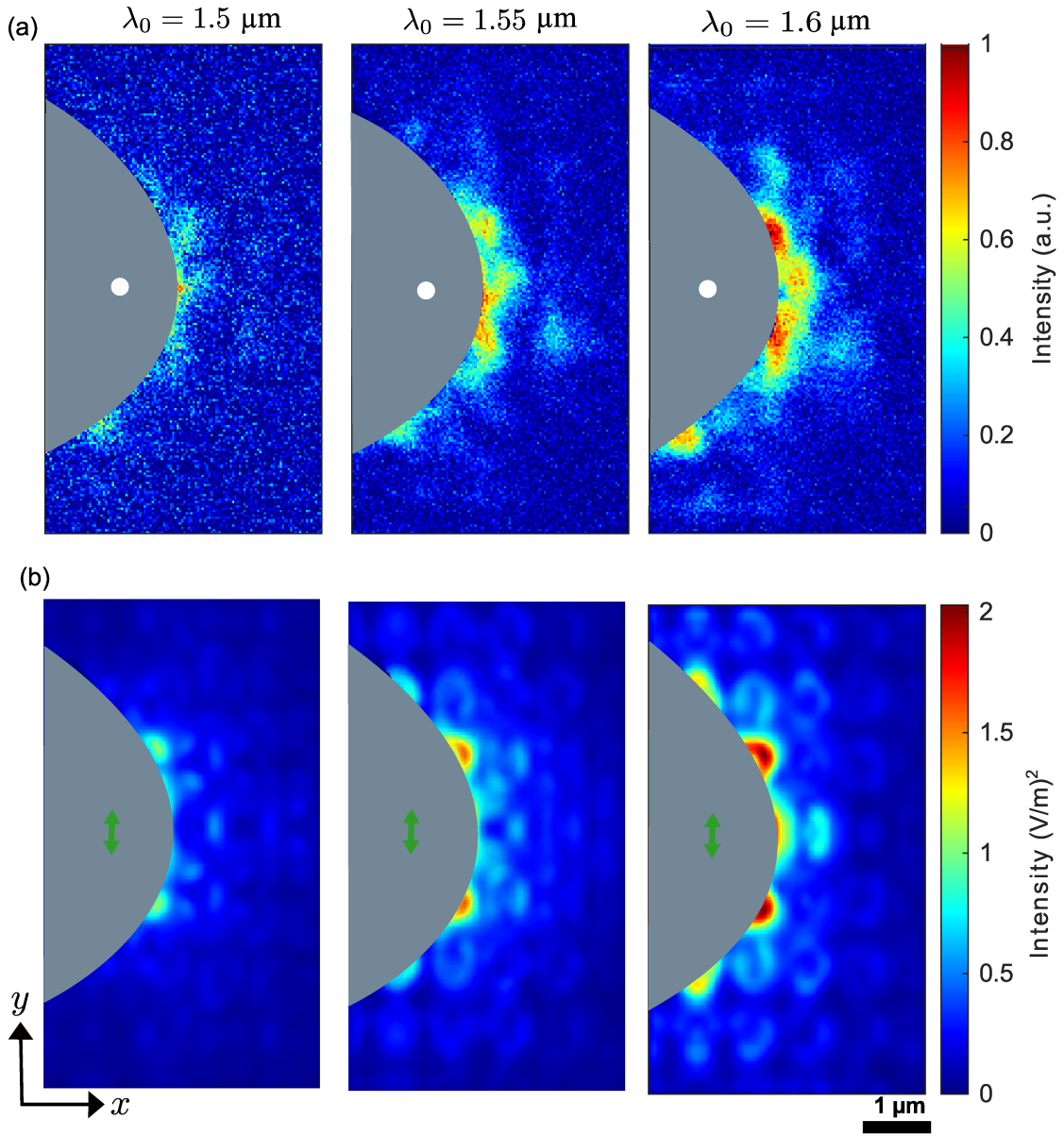

Figure 6.3: (a) Experimental results of wavelength-dependent near-field distribution on top of the nanodisk metasurface. Illumination wavelengths of the excitation tip are written on top of the panels. The white circle shows the position of the excitation tip's aperture. (b) Corresponding numerical simulations for the in-plane electric field intensity while the intensity values within the avoidance area (gray-region) were set to zero. Green double arrows show the position and direction of the magnetic dipole placed at the position of the aperture center.

fields. In Chapter 4, it was discussed that one of the factors to determine the higher sensitivity of the aperture tip to either electric or magnetic fields is the thickness of the aperture rim relative to the aperture diameter [119]. The detection tip in Fig. 6.2(e) shows a rim thickness that is smaller than the aperture diameter. Hence, the aperture tip used in the measurement is expected to be more sensitive to electric

fields. The excellent agreement between the measured near-field intensities and the numerically calculated electric field intensities in Fig. 6.3 corroborates the assumption of the detection tip's sensitivity to electric fields.

In spectral-dependent near-field measurements, the partial LDOS at the position of the excitation tip determines the amount of light that is scattered from or transmitted through the metasurface [42]. Since the position of the excitation tip is stationary, the modification of LDOS can be observed only by changing the illumination wavelength. In Fig. 6.3(a) a near-field pattern at the excitation wavelength $\lambda = 1.5$ µm shows the lowest maximum intensity compared to near-field patterns at other excitation wavelengths. The detection tip maps the scattered light in the near field of the metasurface. According to the transmittance spectra in Fig. 6.2(a) at illumination wavelength $\lambda = 1.5$ µm, most of the light is transmitted through the metasurface, and the amount of scattered light is not significant. For $\lambda = 1.55$ µm, the lower transmittance corresponds to the stronger scattering by nanodisks at this wavelength. The mapped near-field intensity is also stronger than at $\lambda = 1.5$ µm since the higher partial LDOS results in stronger scattering and coupling between the nanodisks. Finally, the near field of the metasurface was mapped at the magnetic dipole resonance wavelength $\lambda = 1.6$ µm. The strong near-field is due to magnetic dipoles induced in the nanodisks at the illumination wavelength $\lambda = 1.6$ µm. The magnetic dipole radiation enhanced the scattered light from the metasurface enabling the excitation of the magnetic dipoles in the adjacent nanodisks. In Section. 6.3 the calculation of partial LDOS at the excitation wavelengths will confirm the assumption of the largest partial LDOS at the MD resonance wavelength. Furthermore, the relation between the integrated mapped near-field intensity and the radiated power of a dipole for the spectral-dependent near-field measurements is discussed.

6.2.2 Near-field pattern spatial dependence

The previous section discussed the spectral-dependent near-field patterns of a metasurface. However, from an application perspective, to enhance or suppress the radiated power by quantum emitters, the radiation frequency related to the energy states can not be changed because it is an intrinsic property of a quantum emitter. Thus, the only approach to modifying the quantum emitters' decay rate is to change their position in a host medium.

For the position-dependent near-field measurements, a silicon nanodisk metasurface featuring two distinct electric and magnetic resonances at wavelengths $\lambda_{\mathrm{MD}} =$

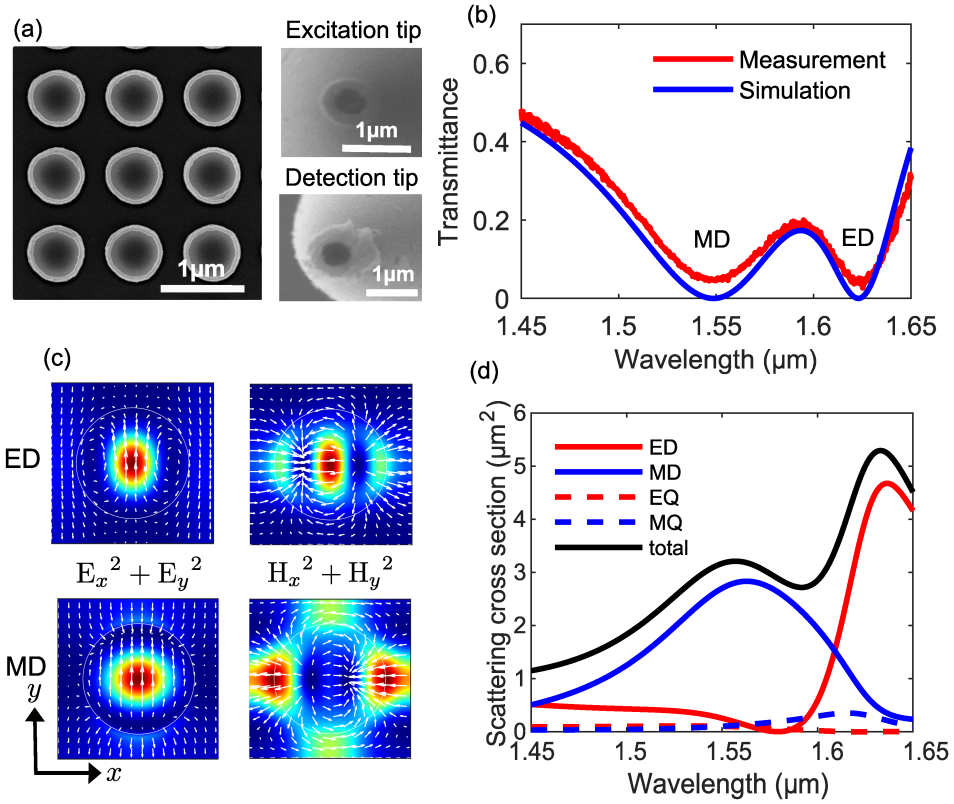

Figure 6.4: (a) SEM images of a silicon nanodisk metasurface, excitation, and detection tips used in the position-dependent near-field measurements. (b) Transmittance spectrum of the metasurface in (a) with $L = 915$ nm. Two minima correspond to the magnetic dipole (MD) and electric dipole (ED) resonance at illumination wavelengths $\lambda_{\mathrm{MD}} = 1550$ and $\lambda_{\mathrm{ED}} = 1624$ nm. (c) Calculated electric and magnetic field intensity at ED and MD resonance wavelengths for a plane wave excitation with y-polarized electric field shown for one lattice constant. (d) Total scattering cross-section of a silicon nanodisk and the individual multipole contributions from electric dipole (ED), magnetic dipole (MD), electric quadrupole (EQ), and magnetic quadrupole (MQ).

1550 nm and $\lambda_{\mathrm{ED}} = 1624$ nm was selected. The metasurface consists of silicon nanodisks with a radius of $r = 318$ nm and a height of $H = 237$ nm, arranged in a square lattice with a lattice constant of $L = 915$ nm on a glass substrate.

Figure. 6.4(a) displays SEM images of the measured metasurface, excitation and detection tips used in the spatial-dependent near-field measurements. The transmittance spectrum of the metasurface in Fig. 6.4 (b) demonstrates two resonance dips corresponding to a MD resonance wavelength $\lambda_{\mathrm{MD}} = 1550$ nm and the ED resonance wavelength $\lambda_{\mathrm{ED}} = 1624$ nm. Due to fabrication errors, the measured spectrum shows slightly higher transmittance than the simulations.

Figure 6.4(c) visualizes the calculated electric and magnetic field intensity patterns of a nanodisk at ED and MD resonance wavelengths. For numerical calculations, a

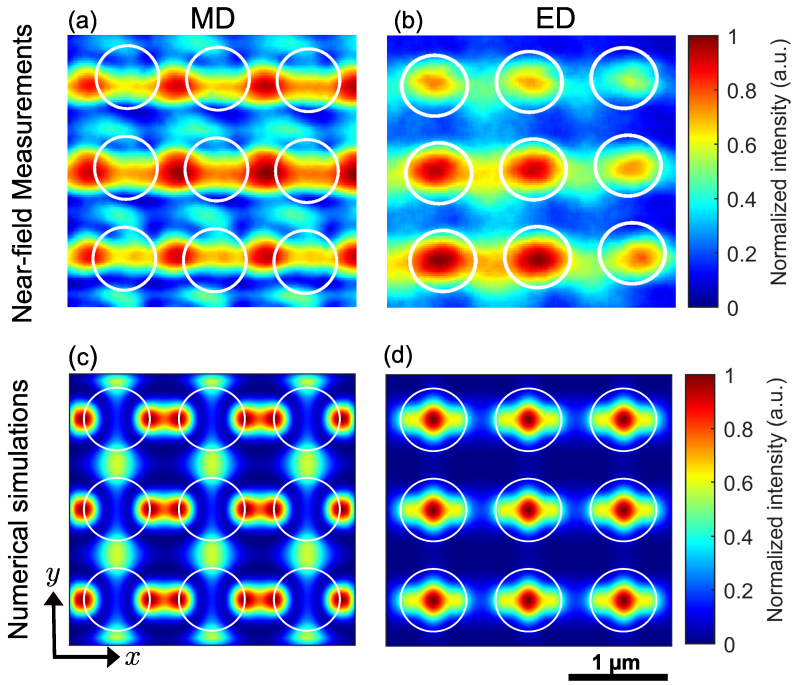

Figure 6.5: Mapped near-field distribution measured by the collection mode SNOM. The illumination wavelengths are (a) MD resonance wavelength $\lambda_{MD} = 1550$ nm and (b) ED resonance wavelength $\lambda_{ED} = 1624$ nm. (c) and (d) corresponding calculated in-plane magnetic intensity for MD and ED resonance, respectively.

plane wave with the y-polarized electric field illuminated a nanodisk at ED and MD resonance wavelengths. The respective in-plane electric and magnetic near-field patterns were monitored in a plane z = 20 nm above the single nanodisk. White arrows indicate the in-plane polarization vectors of the electric and magnetic fields. Figure 6.4(d) shows the scattering cross-section of a single nanodisk indicating multipolar modes that are scattered at different wavelengths. Since the strongest scattering occurs at the ED resonance wavelength, the ED resonance wavelength was used as illumination wavelength by the excitation tip for the position-dependent near-field measurement.

Before performing near-field measurements with the dual-tip SNOM, the detection tip was used in the collection mode to determine the sensitivity of the detection tip to the electric or magnetic fields. In doing so, the path B of the optical setup in Fig. 2.2 was used to illuminate the metasurface from the far field. A laser beam with a polarization along the y-axis was focused on the metasurface after passing through a polarizer and a half-wave plate. The laser wavelength was tuned to the ED and MD resonances and the corresponding near-field intensity patterns, shown in Figs. 6.5(a) and (b), were mapped by the detection tip. Figures 6.5(c) and (d) demonstrate the

corresponding numerical simulations of the in-plane magnetic intensity in the near field of the metasurface for a y-polarized plane wave illumination. Comparing the calculated intensity of the electric and magnetic fields with the measured near-field intensities in the collection mode it can be concluded that the detection tip detected the magnetic fields more efficiently. The mapped near-field intensity and the simulated in-plane magnetic field intensities show nearly the same near-field patterns. However, the measured near-field intensity by the aperture tip could not reveal features of the intensity distribution that are smaller than the aperture tip's resolution, which is limited to its diameter of 350 nm.

In order to perform position-dependent near-field measurements, the excitation tip illuminated the metasurface at the ED resonance wavelength $\lambda = 1624$ nm. The excitation tip was stationary throughout the measurements. A nanopositioning piezoelectric stage displaced the metasurface with respect to the excitation tip. Figures 6.6(a-d) and 6.7(a-e) exhibit the near-field intensity patterns mapped by the detection tip for successive displacements of the metasurface along the x- and y-axis, respectively. The initial position of the excitation tip relative to the metasurface in Fig. 6.6(a), $\Delta x = 0$ and in Fig. 6.7(a), $\Delta y = 0$ was selected arbitrarily. The metasurface displacements Δx and Δy from the initial position are shown on top of each column. The total displacement of the metasurface was roughly one lattice constant. The excitation tip position showed the error of ± 0.05 µm in its position due to mechanical and thermal drifts. There is also the error of ± 0.1 µm to determine the absolute initial position of the excitation tip's aperture with respect to the metasurface. Even though it was possible to use smaller displacement steps to cover one lattice constant, using more steps was avoided to prevent the drift of the excitation tip caused by a longer measurement time.

In the numerical simulations, an in-plane magnetic dipole oriented along the y-axis represents the emission from the excitation aperture tip. White dots with green double arrows denote the excitation aperture tip position and the magnetic dipole, respectively. The white circles mark the edges of the nanodisks. Figures 6.6(i-l) and 6.7(k-o) show the simulation results of the in-plane magnetic field intensity distributions monitored in a plane 20 nm above the metasurface when it is excited by a magnetic dipole in the same plane. The metasurface was displaced in simulations with corresponding retrieved displacements from experiments. In Figs. 6.6(i-l) and 6.7(k-o), the simulated results are plotted with the same scale to increase the visibility of features in the near-field intensity patterns. For the sake of comparing the

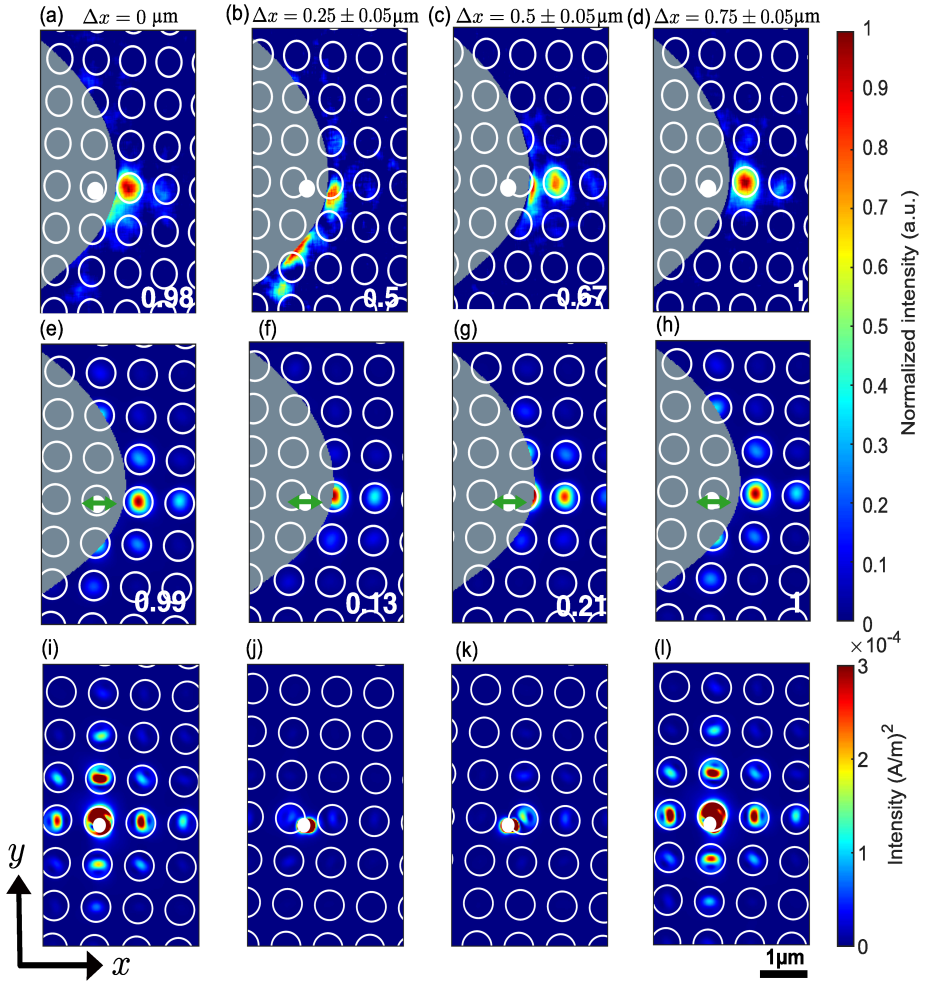

Figure 6.6: (a-d) Measured near-field intensity distributions by the dual-tip SNOM when the metasurface is moved by a displacement of Δx along the x-axis. The initial position is $\Delta x = 0$ where the respective error is ± 0.05 μm due to uncertainty in finding the excitation tip's drifts during the measurements in (b-d). White dots indicate the aperture position of the excitation tip in the measurements. For data normalization, the measured near-field intensities in (a-d) were divided by the maximum measured intensity of all panels. (e-h) Numerical simulations for in-plane components of the magnetic field intensity for the metasurface displacements in (a-d). The gray parabolic-like regions represent the avoidance area. Green double arrows show the position and direction of the magnetic dipole used in the simulations. The simulated intensities with the avoidance area are also normalized after setting the intensities inside the avoidance area to zero to the maximum calculated intensity in (e-h). Panels (a-d) and (e-h) share the common color scale, while the numbers on the right bottom corners are the maximum normalized intensities in each panel. (i-l) Corresponding simulation results of in-plane magnetic field intensities were plotted for the same maximum value to increase the visibility of the near-field pattern.

simulations and near-field measurements in Figs 6.6(i-l) and 6.7(k-o), the calculated intensities corresponding to the avoidance area (gray parabolic-like region) were set to zero. Therefore, Figs. 6.6(e-h) and 6.7(f-j) show simulation results with zero intensities within the avoidance area. The number on the right bottom corner of each panel denotes the maximum normalized intensity in the corresponding panel calculated by dividing the intensities in each panel by a maximum intensity calculated or measured for displacements along the same direction.

In Fig. 6.6(a), the excitation aperture tip is located on top of a nanodisk, and the strong near-field intensity is observed on the nanodisk next to the excitation tip position. The mapped near-field pattern is mainly due to the scattering of nanodisk modes when excited by the emission from the aperture tip. The corresponding simulated near-field intensity considering the avoidance area in Fig. 6.6(e) is in excellent agreement with the experimentally mapped intensity in Fig. 6.6(a).

However, Fig. 6.6(i), the simulation result without setting the avoidance area to zero shows strong intensities in both x and y directions. The radiation of a magnetic dipole (or emission from the aperture tip) oriented along the x axis, positioned close to the center of the nanodisk, efficiently excited the ED mode. The enhanced scatterings from the nanodisk are coupled to neighboring nanodisks along the x- and y-axis and less efficiently in diagonal directions according to the angular radiation of a dipole (or emission from the excitation tip). The coupled field decays fast since the metasurface could not support guided modes. The reason why the mapped near-field intensity in Fig. 6.6(a) is stronger along the x-axis is attributed to the asymmetry of the avoidance area. Due to the particular parabolic shape of the avoidance area, the nearest measurable point along the y-direction is further away than along the x-direction. Moreover, as the intensity decays rapidly from the excitation point, a lower intensity was mapped in the y-direction.

The excitation tip was placed above the edges of a nanodisk for the displacements in Figs. 6.6(b-c). At the edges of the nanodisks, the ED mode is not excited efficiently. Therefore, the near-field patterns show weaker intensity patterns compared to Fig. 6.6(a). The corresponding simulations with the avoidance area in Figs. 6.6(f-g) also confirms the decrease of the maximum intensities. The slight difference between the measured near-field pattern in Fig. 6.6(b) and simulated near-field intensity in Fig. 6.6(f) could be the result of the error in retrieving the exact position of the excitation tip on the metasurface, or it could be attributed to the low signal-to-noise ratio of the detection tip. In Fig. 6.6(j-k), we show the simulations excluding the avoidance

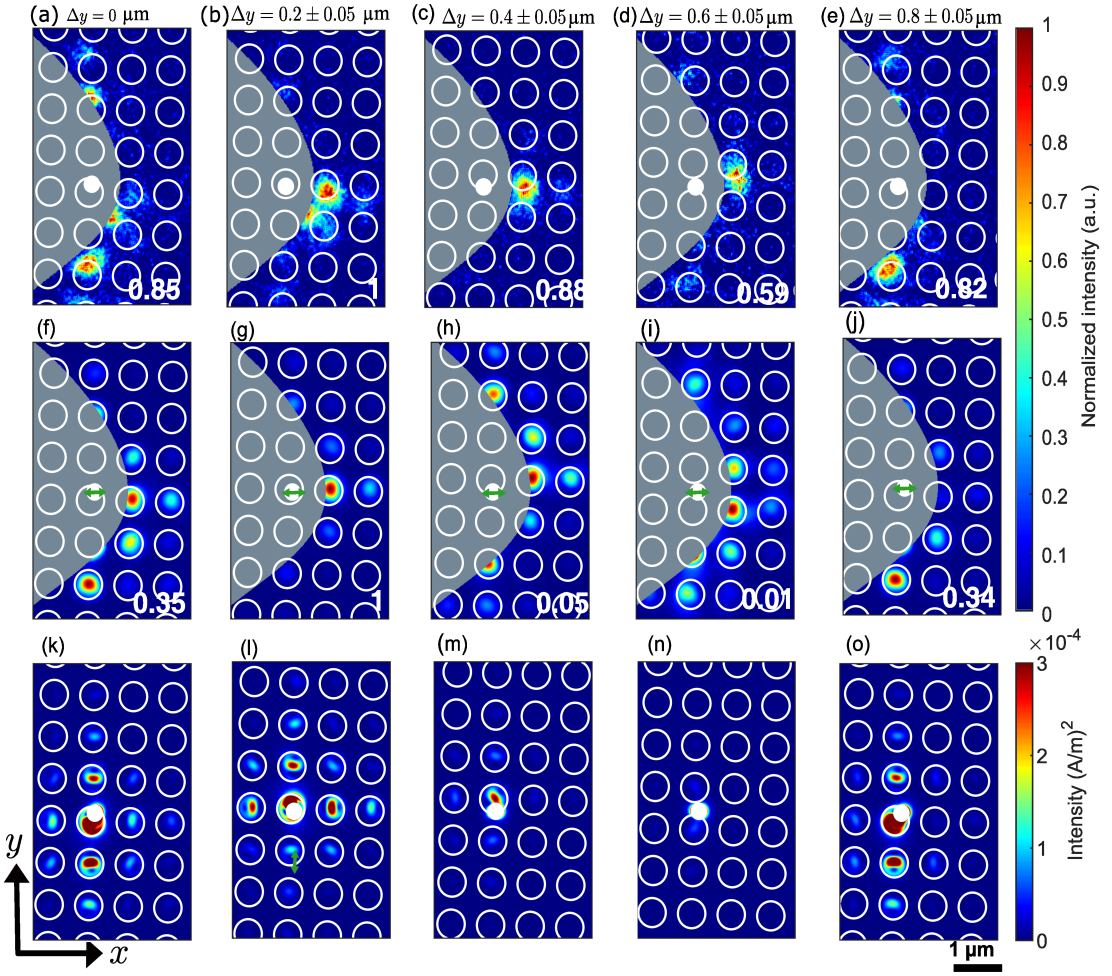

Figure 6.7: (a-e) Measured near-field intensity distributions for the metasurface displacements Δy along the y-axis. The initial position is $\Delta y = 0$. White dots indicate excitation aperture tip positions in the measurements. ± 0.05 µm is the error in the displacements (b-e) due to drifts of the excitation tip during the measurements. (f-j) Numerical simulations of the in-plane magnetic field intensity components for the metasurface displacements (a-e). (k-o) Simulation results in (f-j) without setting the avoidance area to zero. The simulation results share the same color scale to increase the visibility of the near-field patterns. Panels (a-e) and (f-j) share the common color scale. Numbers on the right bottom corners are the maximum normalized intensities in each panel. After setting the intensities inside the avoidance areas to zero, the simulated (measured) intensities were normalized by dividing by the maximum calculated (measured) near-field intensity in all panels for the respective displacements. The gray parabolic-like region is the avoidance area. The green double arrow denotes the magnetic dipole direction and position in the simulations.

area. The weaker near-field intensities also indicate the lower coupling efficiencies of the emission from the excitation tip to modes of the metasurface.

For the metasurface displacement of about one lattice constant from the initial position due to the periodic arrangement of the nanodisk, the near-field distribution

is expected to show a similar pattern as the mapped intensity in Fig. 6.6(a). Similar patterns are observed in the measured near-field intensity in Fig. 6.6(a),(d) and the corresponding simulated intensities in Fig. 6.6(e), (h). Although simulated near-field patterns in Figs. 6.6(i) and (l) are not identical they still display very similar near-field distribution for the displacement of roughly one lattice constant.

A displacement of the metasurface along the y-axis also leads to different coupling efficiencies, resulting in distinct intensity patterns in the near field of the metasurface. Figures 6.7(a-e) exhibit the measured near-field intensity pattern when the metasurface is displaced along the y-axis. In Fig. 6.7(a), the aperture tip's initial position on the upper edge of the nanodisk results in the higher intensity along the y-axis. It is evident that the excitation tip position relative to a nanodisk of the metasurface determines the scattering direction and, in turn, the excited modes, which is consistent with the behavior of partial LDOS at different positions. The simulated near-field pattern in Fig. 6.7(f) shows good agreement with the mapped intensity in Fig. 6.7(a). The simulated near-field intensity in Fig. 6.7(k) also reveals modes coupling due to scattering mainly along the y-axis.

In Fig. 6.7(b), the excitation tip is placed almost in the middle of the nanodisk. The mapped intensity is, therefore, stronger along the x-axis similar to Fig. 6.6(a). The numerical result at the corresponding position in Fig. 6.7(g), considering the avoidance area, verifies the measured near-field distribution pattern in Fig. 6.7(b). The asymmetry of the avoidance area explains the stronger near-field intensity along the x-axis. Nevertheless, the simulation of the near-field intensity without avoidance area (Fig. 6.7(l)) shows the coupling of modes in all directions.

In Figs. 6.7(c) and 6.7(d), the excitation tip is positioned on the inner edge of the nanodisk and in between the nanodisks, respectively. The maximum intensity is lower when the excitation tip is located in between the nanodisks, which indicates a less efficient coupling of the excitation tip's emission to the modes of the metasurface. In other words, the number of available modes that the dipolar emission can couple into is lower when the excitation tip is on the edge of a nanodisk or between nanodisks.

The details of the simulated near-field patterns in Figs. 6.7(h) and 6.7(i) are not observed in the mapped near-field intensities in Figs. 6.7(c) and 6.7(d). The reason is the low signal-to-noise ratio of the detection tip. The corresponding simulations without avoidance area in Fig. 6.7(m-n) also indicate that the emission from the excitation tip was not efficiently coupled to the modes of the metasurface. Therefore, no details are observed in simulated near-field intensity patterns.

In Fig. 6.7(e), the excitation tip is placed nearly at a distance of one period from its initial position, i.e., in the upper edge of the nanodisk. The mapped near-field pattern shows mode coupling due to emission scattering from the excitation tip along the y-axis. The near-field pattern is also similar to the intensity distribution obtained for the excitation at the initial position of the tip (Fig. 6.7(a)), indicating that the displacement along the y-axis corresponded to almost one lattice constant. The simulation in Fig. 6.7(j) shows a good agreement with the measurement result in Fig. 6.7(e), which also displays the more efficient excitation of modes and their longer decay length along the y-axis. Moreover, in Fig. 6.7(o), the result of the simulation without avoidance area also shows a higher intensity along the y-axis.

Remarkably, the results of position-dependent near-field patterns measured by the dual-tip SNOM are in good agreement with the numerical simulations. The small discrepancies between the measurements and simulations can be explained as follows. The slight broadening of the measured near-field intensity patterns, as compared with the simulations, is due to the limited resolution of the detection tip defined by its aperture diameter. The detection tip cannot resolve features of the near-field intensity that are smaller than the size of its aperture [4]. Hence, it averages over small features during the detection of the optical near-field signal. Furthermore, the map of the near-field optical signal and topography signal (white circles on the measured near-field intensities) experienced different offsets next to the boundary of the avoidance area arising from the asymmetric coating geometry of the excitation and detection tips. Thus, the interpretation of near-field intensity according to the topography signal becomes more difficult for the measured near-field next to the avoidance area.

6.3 Integrated measured near-field intensity and partial LDOS

When it comes to a dipole excitation near a photonic system and the respective near-field distribution, the role that the change of partial LDOS plays in measured near-field patterns should be discussed. When a classical magnetic dipole is placed near a nanostructure, the magnetic partial LDOS (Eq. 6.5) quantifies the number of excited modes at the position of a magnetic dipole according to the strength of the polarization vectors of magnetic fields projected along the direction of the magnetic dipole [42]. To elaborate on the definition of the magnetic partial LDOS, consider the example of the magnetic field intensity and the in-plane polarization vectors of the ED mode in Fig. 6.4(c). The maximum contribution of the ED mode to the partial LDOS is obtained for a magnetic dipole polarized along the x-axis and placed

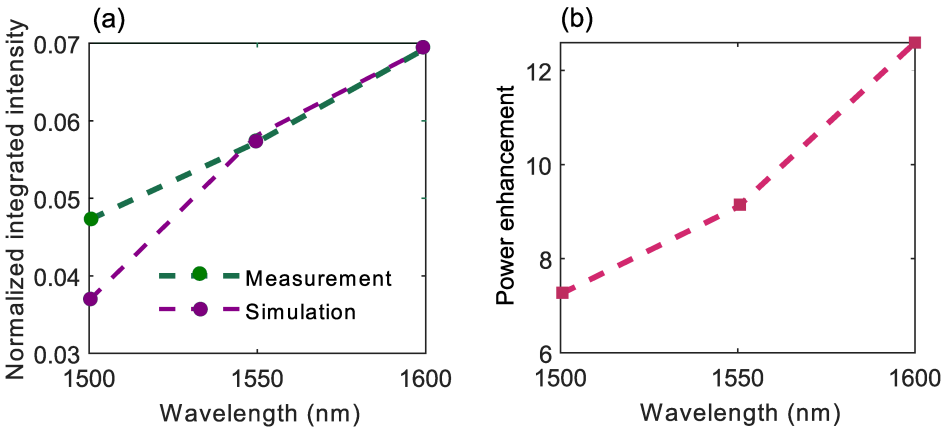

Figure 6.8: (a) Normalized integrated intensities for the measurements in Fig. 6.3(a) and simulations in Fig. 6.3(b) for three different excitation wavelengths. (b) Corresponding normalized radiative power of the magnetic dipole. The integrated measured intensities were scaled to the maximum integrated intensity from simulations.

at the position where the magnetic field also has the polarization vector along the x-direction, with the maximum intensity strength. Although the partial LDOS takes into account the contribution of all available modes, and not only a single mode, at the ED resonance wavelength of (λ = 1624 nm), the excited modes are dominated by the ED contribution. The maximum contribution of ED modes is observed in the multipolar decomposition of the scattering cross-section for a single nanodisk in Fig. 6.4(d). A similar argument can explain the behavior of the mapped near-field intensity distributions. The polarization of the dipolar emission from the excitation tip remained constant during dual-tip SNOM measurements. However, since the partial LDOS is a function of position, changing the excitation tip position relative to the metasurface gives rise to different excited modes.

Although the dual-tip SNOM configuration cannot measure the near-field exactly at the aperture tip position, changes of partial LDOS are reflected in distinct near-field intensity patterns mapped by the detection tip around the excitation tip. In other words, different measured near-field intensity distributions arise from changes of the scattering due to modification of partial LDOS at different excitation tip positions. It should be noted that changes of the partial LDOS cannot be inferred only according to different near-field patterns. LDOS modifications require changes in the power of scattered light at the excitation tip position. Hence, to verify the partial LDOS modification, the mapped near-field intensity was integrated within the scan window. The integrated intensity means that the near-field intensities of all pixels mapped by

the detection tip are summed up within the scan windows as follows,

$$\sum_{x=1}^{M}\sum_{y=1}^{N} I(x,y). \tag{6.7}$$

Here, $I(x,y)$ is the intensity at pixel position (x,y). The number of pixels along the width and length of the scan window is M and N, which are equal in dual-tip SNOM measurements. For intensities within the avoidance area, $I(x,y) = 0$. It is useful to consider Eq. (6.6) to elaborate the relation between the integrated intensity and the partial LDOS. According to Eq. (6.6), the mapped near-field intensity is related to the partial LDOS when the excitation tip is described as a magnetic dipole oriented along x or y direction. If the integrated near-field intensity changes, it indicates the partial LDOS modification at the excitation tip position [42]. Furthermore, referring to Eq. (6.3) where the power enhancement is proportional to partial LDOS, in the rest of the chapter, the relation between the integrated measured near-field intensities in the spectral and spatial near-field measurements and the power enhancements at the excitation tip position will be discussed.

The radiated power of a magnetic dipole P_{rad}, at the position of the excitation tips in the near-field measurements, was calculated using Lumerical FDTD solver. Calculations were carried out inside the volume enclosing the entire metasurface. P_0 denotes the power radiation of a dipole on a glass substrate without silicon nanodisks. The dipolar emission is coupled to radiative and non-radiative modes. The radiative P_{rad} and non-radiative P_{loss} power emitted from a magnetic dipole, located at $z = 20$ nm above the metasurface was calculated for the excitation wavelengths in the near-field measurements. As expected, the losses are negligible in the analyzed spectral range of the silicon metasurface; thus, all the emission corresponds to radiative power.

To compare the integrated measured near-field intensity and power enhancement by a dipole, the normalized power was numerically calculated for both spectral (Fig. 6.3) and spatial (Figs. 6.6 and 6.7) near-field measurements. Figure 6.8(a) shows the integrated intensity calculated from near-field measurements (Fig. 6.3(a)) and corresponding simulations in Fig. 6.3(b). The intensity values are integrated over the scan window, excluding the avoidance area. The integrated intensity values from the measurements were normalized to the maximum integrated intensity calculated by numerical simulations. Figure 6.8(b) shows the normalized power (power enhancement) radiated by a magnetic dipole. The normalized radiated power was simulated for excitation wavelengths of the near-field spectral-dependence measurements. It is evident from Figs. 6.8(a) and (b) that changes of integrated intensities (in-plane

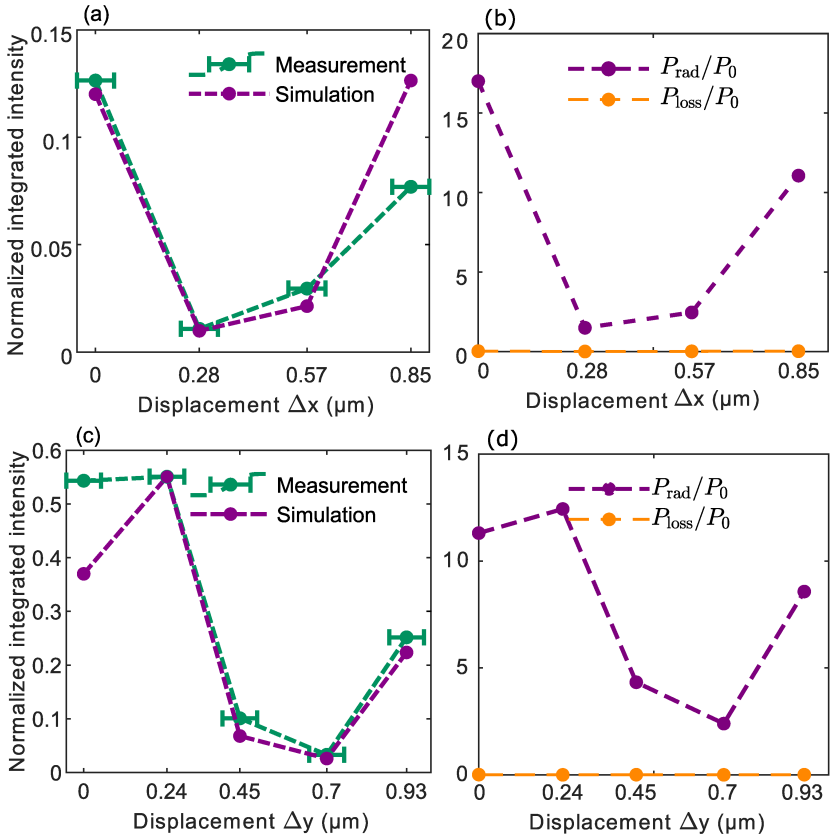

Figure 6.9: (a) Normalized integrated intensities for the measurements in Fig. 6.6(a-d) and simulations in Fig. 6.6(d-h) for Δx displacements. The error bar only shows the error in finding displacements due to the drift of the excitation tip during the measurements (b) Corresponding power enhancement and the power loss of the magnetic dipole radiation (c) Normalized integrated intensities for the measurements in Fig. 6.7(a-e) and simulations in Fig. 6.7(h-j) for Δy displacements. (d) Corresponding power enhancement and power loss of the magnetic dipole for the same Δy displacements. To normalize the integrated intensity of the measurements, they were scaled to the maximum value of the integrated intensity in the simulations

power) and power enhancement at different measured wavelengths follow the same behavior.

For the position-dependent near-field measurements, the power enhancement of a magnetic dipole was also calculated and compared with the integrated measured near-field intensities.

Figure 6.9(a) shows the normalized integrated intensity calculated from the mapped intensity patterns in Figs. 6.6(a-d) (measurement) and Figs. 6.6(e-h) (simulation) for the metasurface displacements along the x-axis. The intensity values are integrated over the scan window, excluding the avoidance area. Likewise, Fig. 6.9(c) exhibits the normalized integrated mapped near-field intensities in Figs. 6.7(a-e) (measurement) and Figs. 6.7(f-j) (simulation) for the metasurface displacements along the y-axis. In

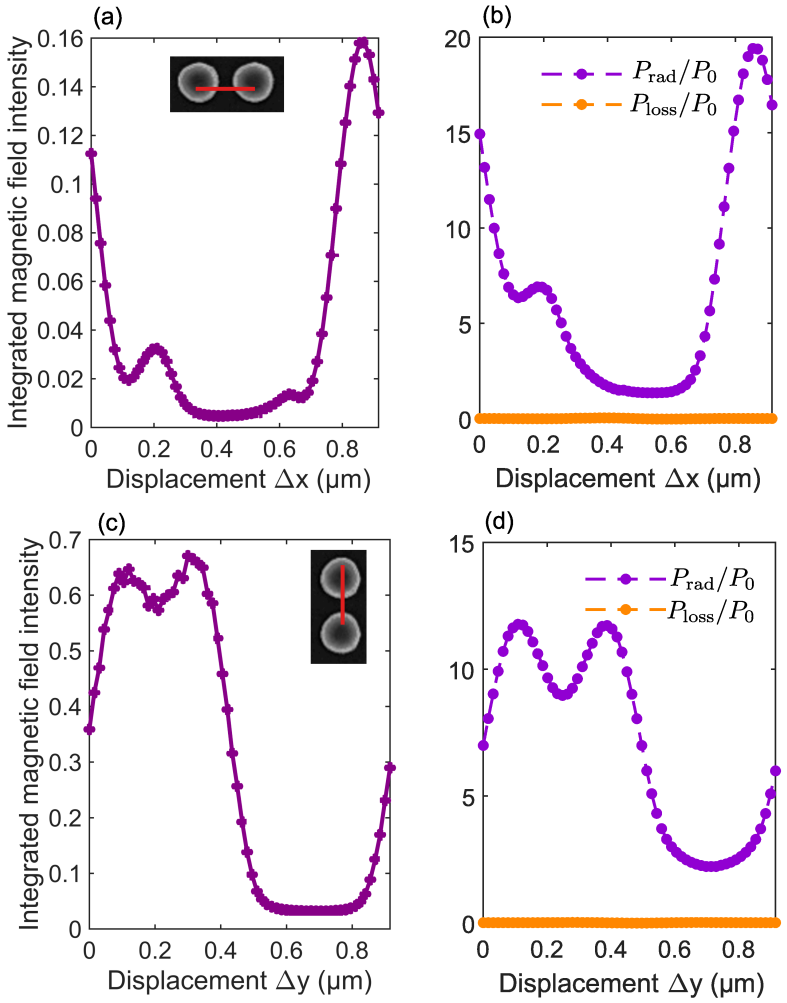

Figure 6.10: (a) and (c) Numerically calculated integrated near-field intensity for displacements of the metasurface along the x- and y-axis equal to one lattice constant ($L = 915$ nm). The increment of the metasurface displacement between consecutive simulations is 15 nm. (b) and (d) Corresponding normalized radiative power and the power loss of the dipole for the same displacements of the metasurface as in (a) and (c), respectively. The insets are two nanodisks of the metasurface with red line equal to $L = 915$ nm denotes the initial and final position of the magnetic dipole relative to the metasurface.

Figs. 6.9(a) and (c), raw data of the measured integrated near-field intensities, after subtracting the constant value due to the measurement noise, were scaled to the maximum value of the integrated intensities in the simulations. In Figs. 6.9(a) and 6.9(c), horizontal error bars represent the error in determining the displacement of the metasurface along the x- and y-axis due to drifts of the excitation tip during measurements. This error could be one reason for the observed difference between the integrated near-field intensities of the measured and calculated data. Moreover, the influence of two tips when they are laterally close within the region of shear forces could be another

reason for the observed discrepancy in the measured near-field intensities compared with simulations. Figures 6.9(b) and 6.9(d) show the power enhancement P_{rad}/P_0 and power loss P_{loss}/P_0 for the metasurface displacements Δx and Δy. Comparing the integrated intensity and power enhancement again corroborates that integrated measured position-dependent near-field intensities using the dual-tip SNOM and the corresponding calculated power enhancement of a dipole show the same change of behavior. It should be emphasized that the integrated near-field intensity can only determine the relative changes of partial LDOS for different excitation positions.

To further support the argument that near-field measurements using dual-tip SNOM can predict the partial LDOS behavior, the electromagnetic near-field distribution for metasurface displacements along the x- and y-axis relative to a magnetic dipole were numerically calculated for one lattice constant $L = 915$ nm (red lines in the insets of the Fig. 6.10) with an increment of 15 nm. Numerical simulations were carried out for a magnetic dipole with the orientation along the x-axis. The initial magnetic dipole positions relative to the metasurface were chosen according to the initial position of the excitation tip relative to the metasurface for position-dependent near-field measurements with displacements along the x- and y-axis.

Figures 6.10(a) and 6.10(c) show the results of the integrated near-field intensity in a plane $z = 20$ nm above the metasurface after setting the intensity data of the avoidance area to zero. The power enhancement P_{rad}/P_0 and power loss P_{loss}/P_0 of the dipole are plotted in Figs. 6.10(b) and 6.10(d). Despite excluding the avoidance area, the integrated intensities appear to behave in much the same way as power enhancement P_{rad}/P_0. Thus, we can argue that observed changes in the integrated near-field intensities indicate the partial LDOS modifications.

In conclusion, near-field measurements using the automated dual-tip SNOM showed that the mapped near-field patterns due to dipolar emission from an excitation aperture tip vary at different excitation frequencies and dipole positions relative to the silicon metasurface. Moreover, the extent and direction of the mapped near-field intensity patterns highly depend on the position and the orientation of a dipole. More strikingly, it was verified that the integrated mapped near-field intensity, despite the inaccessibility of optical near-field data within avoidance area, can predict the behavior of the partial LDOS at different excitation positions.

7 Summary and outlook

The main goal of this thesis was to realize a fully automated and robust dual-tip SNOM and demonstrate its capabilities to characterize nanophotonic systems. The distinct advantage of the dual-tip SNOM is the excitation and detection of evanescent waves in the near field of the sample, accessing optical information that is hard to attain with other super-resolution microscopy techniques. Despite the versatility of dual-tip SNOM to perform a wide variety of near-field measurements, thus far, only a few measurements have been reported using the dual-tip SNOM. The primary reason that dual-tip SNOM has not attracted much attention so far was the lack of a reliable method to control the distance between the excitation and detection tips and prevent their collision and damage during near-field measurements.

In this thesis, I realized the first fully automated dual-tip SNOM, where the detection tip automatically scans the entire area surrounding the excitation tip without any collision. The instabilities encountered in a previous attempt to realize the automated detection tip were overcome by using a digital SNOM controller capable of simultaneously controlling excitation and detection tips.

Implementing a collision prevention scheme based on weakly coupled oscillators (tuning forks) to automate the detection tip scan was thoroughly investigated. The relevant parameters such as excitation tip position and the minimum distance between the excitation and detection tip were introduced. The stability and robustness of the automated dual-tip SNOM were explored for a wide range of oscillation amplitudes of the excitation tip and avoidance threshold signals, as the main parameters affecting the stability of the automated scan procedure.

Once the automated dual-tip SNOM was successfully implemented, it was used to measure the near field of different photonic systems. Since most photonic systems

are polarization-sensitive, it is essential to characterize the emission polarization from excitation aperture tips. I have investigated the polarization characteristic of the emission from bent fiber aperture tip through exciting SPPs on an air-gold interface. The results of the near-field SPP patterns verified that the bent aperture tips, depending on their specific geometry, allow only particular polarizations to pass through the bend and arrive at the aperture plane. Furthermore, a comparison between the emission pattern from the real geometry of the excitation tip and the radiation pattern of a magnetic dipole was performed. It was shown that the Bethe-Bouwkamp model, which describes the emission from a subwavelength aperture in an infinite conducting plane, is a good approximation for describing the emission from an excitation tip with a subwavelength aperture. Since the dual-tip SNOM has facilitated the characterization of the emission from the aperture tip, the emission patterns of different aperture tips were investigated through the near-field angular distribution pattern of the SPPs. The field distribution of excited SPPs gives information about both the polarization and the angular emission from the excitation aperture tip. In this regard, a directional pattern of the SPPs was mapped by a detection tip for the emission from one of the excitation tips, indicating the excitation of both electric and magnetic dipole moments when the fiber mode was incident on the aperture plane at an oblique angle. Thus, the near-field pattern of SPPs provides a way to determine the electric and magnetic dipole moments that could be excited at the apex of the aperture tip according to its geometry. Next, I wanted to demonstrate the unique applicability of the dual-tip SNOM by locally excite nanostructured photonic systems at their specific geometric features and map the corresponding near-field distribution. As a first step in this direction, I conducted experiments when the excitation aperture tip illuminated the edge of a gold platelet and excited SPP waves on the edge. The detection tip mapped a complex near-field pattern due to the excited SPPs and reflected SPPs from edges of a hexagon-like monocrystalline gold platelet. To the best of our knowledge, it was the first measured near-field interference pattern of SPPs due to the edge excitation and detection merely in the near field. In similar near-field measurements, the far-field illumination always used to excited the SPP waves on the edge. The dipolar emission from the aperture tip close to the edge of the gold platelet allowed the image dipole method to calculate the near-field distribution of the SPPs interference pattern analytically. Comparing the numerical calculation of the SPP interference pattern on the gold platelet with the analytical model showed the

relevance of the image dipole method to calculate the interference pattern measured by a dual-tip SNOM on metallic surfaces with edges.

The ability of the automated dual-tip SNOM to examine nanostructured samples was further verified by a robust automated scan performed by a detection tip on a silicon nanodisk metasurface. In this regard, the dual-tip SNOM measured the spectral- and spatial-dependent near-field patterns above a nanodisk metasurface. For spectral-dependent near-field measurements, the excitation tip illuminated the silicon metasurface at different wavelengths. Furthermore, in position-dependent near-field intensity measurements, the excitation wavelength remained unchanged at the electric dipole resonance of the metasurface while the excitation tip position relative to the metasurface was changed. The changes of integrated measured near-field intensity maps were shown to be correlated to the partial LDOS of the metasurface at the position of the excitation tip. The integrated intensity was larger for positions where e.g. the larger partial LDOS was expected. Numerical calculations also corroborated that the integrated intensity of a near-field pattern mapped by a detection tip is related to the partial LDOS of the nanodisk metasurface at the respective excitation position.

Prospectively, the automated dual-tip SNOM as a novel near-field measurement technique has great potential to study near-field optical phenomena in various nanophotonic systems. Apart from metasurfaces, photonic crystals, and waveguides, investigation of topological photonics can profit from the dual-tip SNOM where the measurements of bound states in the continuum are of great interest [193]. The cross density of states (CDOS), indicating the correlation between the excitation and detection points in complex [87, 194] and disordered photonic systems [195], can be also measured using the dual-tip SNOM.

The dual-tip SNOM can systematically characterize the emission pattern from SNOM tips with different apex geometry. However, future research should replace aperture tips which have rather low transmission and resolution, with other SNOM tips such as plasmonic tips to enhance the excitation and detection efficiencies, and the spatial resolution of obtained images [196].

The automated dual-tip SNOM can also interface a quantum emitter with a photonic system. In doing so, the quantum emitter can be located at the desired position, and the detection tip can map a corresponding near-field optical response due to the interaction of a dipole moment transition with the surrounding medium. The most practical tip could be a quantum emitter grafted at the apex of the uncoated fiber tip

allowing both electric and magnetic dipole transition [38]. Furthermore, spin-orbit interaction [197] phenomena could be investigated in the near field using circularly polarized light emitted from an excitation tip, while a detection tip measures the near-field distribution in chiral quantum photonic systems [64, 198]. Moreover, the highest efficiency of quantum emitter coupling to a nanophotonic system can be achieved if the dipolar emission of the quantum emitter is coupled to the mode of a resonator with a similar field distribution. Using the dual-tip configuration to identify the emission pattern of a point source, such as the aperture tip, fluorescent molecule, or quantum dot, could therefore provide better control of quantum emitter coupling to nanophotonic systems.

Moreover, it was shown that the integrated intensity of a near-field map is correlated to the partial LDOS for a particular excitation position. Hence, if the far-field measurement is integrated into the automated dual-tip SNOM setup, the partial LDOS behavior can be investigated simultaneously with both illumination SNOM and dual-tip SNOM. As a result, the radiative and nonradiative parts of the scattered near field could be determined.

However, one of the most challenging and intriguing applications of the dual-tip SNOM that is still ahead of us would be measuring the dyadic Green function of photonic systems for a dipolar excitation at visible and near-infrared wavelengths. The automated dual-tip setup can only map the near-field intensity. If an interferometric phase-detection setup is integrated into the dual tip SNOM, the amplitudes and phases of the in-plane electric and magnetic fields can be measured. Consequently, all electromagnetic field components can also be retrieved if only in-plane electric and magnetic field components are measured [199]. In addition to the complexities that a single aperture tip caused in the near-field measurements [4, 116, 200], extra challenges particular to the automated dual-tip SNOM should be addressed to enable the dyadic Green's function measurement. Currently, the automated dual-tip SNOM suffers from thermal and mechanical drift after long hours of measurements, and this issue should be addressed to increase the precision of measurement results. Moreover, the perturbation of the near-field distribution due to two SNOM tips and their influence on image formation when two tips are laterally close should be investigated with rigorous numerical calculations. Nevertheless, the automated dual-tip SNOM is still in its infancy and has great potential to develop further and investigate the unknown aspects of near-field phenomena in a nanoscale world.

A

Zusammenfassung

Das Hauptziel dieser Doktorarbeit war die Realisierung eines vollautomatischen und robusten optisches Rasternahfeldmikroskop (SNOM) mit Doppelspitzen ermöglicht. Dieses den Zugang zu optischen Informationen, die mit anderen superauflösenden Mikroskopietechniken nicht einfach zu erreichen sind. Der entscheidende Vorteil des Doppelspitzen-SNOM ist die Anregung und Detektion von evaneszenten Wellen im Nahfeld der Probe. Es fehlte jedoch eine zuverlässige Methode, um den Abstand zwischen den Anregungs- und Detektionsspitzen zu kontrollieren, um deren Kollision und Beschaedigung während der Nahfeldmessungen zu verhindern. Beim vollautomatischen Doppelspitzen SNOM tastet die Detektionsspitze automatisch den gesamten Bereich um die Anregungsspitze herum ab, ohne dass es zu Kollisionen kommt. In dieser Arbeit wurde die Implementierung eines Kollisionsverhinderungsschemas auf der Grundlage schwach gekoppelter Oszillatoren (Stimmgabeln) zur Automatisierung der Abtastung der Detektionsspitze eingehend erläutert. Nach erfolgreicher Implementierung des automatisierten Doppelspitzen-SNOM wurde der Aufbau zur Messung des Nahfelds verschiedener photonischer Materialien verwendet. Zunächst wurde das Doppelspitzen-SNOM verwendet, um die Polarisationscharakteristik der Emission von der gebogenen Faseraperturspitze durch Anregung von Oberflächenplasmonenpolaritonen (SPPs) an einer Luft-Gold-Grenzfläche zu untersuchen. Darüber hinaus zeigte ein Vergleich zwischen dem Emissionsmuster der realen Geometrie der Anregungsspitze und dem Strahlungsmuster eines magnetischen Dipols, dass das Bethe-Bouwkamp-Modell eine gute Annäherung ist, um die Emission von der Subwellenlängen-Apertur einer Faserspitze zu beschreiben. Darüber hinaus wurde mit einer Detektionsspitze eine gerichtete Feldverteilung der SPPs für die Emission von einer Anregungsspitze gemessen. Die gerichtete SPP-Feldverteilung deutet

auf die Anregung sowohl elektrischer als auch magnetischer Dipolmomente hin, wenn die Fasermode in einem schrägen Winkel auf die Aperturebene trifft. Eine weitere einzigartige Anwendung des Doppelspitzen-SNOM ist die lokale Anregung des Randes oder der Ecke eines photonischen Systems und die Abbildung der entsprechenden Nahfeldverteilung. Die automatisierte Detektionsspitze bildete auch ein komplexes Nahfeldmuster ab, das auf die angeregten SPPs und die reflektierten SPPs von den Kanten des hexagonal-ähnlichen monokristallinen Goldplättchens zurückzuführen ist. Die dipolare Emission von der Aperturspitze in der Nähe der Kante des Goldplättchens ermöglichte es mit dem Bild-Dipol-Modell die Nahfeldverteilung des SPP-Interferenz analytisch zu berechnen. Die herausragendste Fähigkeit des in dieser Arbeit gezeigten automatisierten Doppelspitzen-SNOM sind spektral- und ortsabhängige Nahfeldmessungen einer Nanodisk-Metasurface als nanostrukturierte Probe. Bei den spektralabhängigen Nahfeldmessungen beleuchtete die Anregungsspitze die Silizium Metasurface bei unterschiedlichen Wellenlängen. Bei den spektralabhängigen Nahfeldmessungen wurde eine feste Anregungswellenlänge verwendet, um die positionsabhängigen Nahfeldintensitäten zu messen, wenn die Metasurface relativ zur Anregungsspitze verschoben wurde. Es konnte gezeigt werden, dass die integrierten gemessenen Nahfeldintensitäten durch das Doppelspitzen-SNOM mit der partiellen lokale Zustandsdichte der Metasurface an der Position der Anregungsspitze korreliert sind.

B

Publications

Journals articles

- N Abbasirad, A Barreda, D Arslan, M Steinert, Y Chen, J Huang, I Staude, F Setzpfandt, and T Pertsch. Near-field interference map due to a dipolar emission near the edge of a monocrystalline gold platelet. *Journal of Optics* 24.12 (2022): 125001.

- N Abbasirad, A Barreda, Y Chen, J Huang, I Staude, F Setzpfandt, and T Pertsch. Near-field launching and mapping unidirectional surface plasmon polaritons using an automated dual-tip scanning near-field optical microscope. *Photonics Research* 10.11 (2022): 2628-2641.

- N Abbasirad, A Barreda, D Arslan, M Steinert, S Fasold, C Rockstuhl, I Staude, F Setzpfandt, and T Pertsch. Investigation of dipole emission near a dielectric metasurface using a dual-tip scanning near-field optical microscope. *Nanophotonics*, 10.18 (2021): 4511-4522.

- N Abbasirad, J Berzins, K Kollin, S Saravi, N Janunts, F Setzpfandt, and T Pertsch. A fully automated dual-tip scanning near-field optical microscope for localized optical excitation and detection in the visible and near-infrared. *Review of Scientific Instruments*, 90.5 (2019): 053705

Conference proceedings

- N Abbasirad, D Arslan, S Fasold, I Staude, F Setzpfandt, and T Pertsch. Position-dependent measurement of the near-Field coupling in silicon nanodisc

arrays by dual-tip scanning near-field optical microscope. *NFO 16, the 16th International Conference on Near-Field Optics, Nanophotonics and Related Techniques*, Victoria,Canada, 17-21 August 2020, online oral presentation.

- N Abbasirad, D Arslan, J Berzins, S Fasold, I Staude, F Setzpfandt, and T Pertsch. Mapping the near-field interaction of silicon nanodisc arrays by automated dual-tip scanning near-field optical microscopy. *2019 Conference on Lasers and Electro-Optics Europe European Quantum Electronics Conference (CLEO/Europe-EQEC), IEEE*, 2019, oral presentation.

- N Abbasirad, D Arslan, J Berzins, S Fasold, I Staude, F Setzpfandt, and T Pertsch. Fully automated dual-probe SNOM for near-field excitation and characterization of nanodiscs arrays. *The 15th International Conference on Near-Field Optics, Nanophotonics and Related Techniques*, Troyes, France, 26-31 August 218, poster presentation.

- N Abbasirad, D Arslan, J Berzins, S Fasold, I Staude, F Setzpfandt, and T Pertsch. Study of nanophotonic systems by dual-probe SNOM. *The 21th Non-Contact Atomic Force Microscopy*, Porvoo, Finland, 17-21 September 2018, poster presentation.

- N Abbasirad, D Arslan, S Fasold, I Staude, F Setzpfandt, and T Pertsch. Dual-probe SNOM for the near-field study of nanostructures. *2018 Photonics North (PN). IEEE*, 2018, oral presentation.

- N Abbasirad, K Kollin, N Janunts, F Setzpfandt, and T Pertsch. A Fully Automated Dual-Probe Scanning Near-Field Optical Microscopy Technique. *Laser Science. Optical Society of America*, 2017, poster presentation.

C

Acknowledgement

While pursuing my Ph.D., I had the privilege of collaborating and receiving support and help from many people to whom I am indebted and grateful. First and foremost, I am deeply grateful to my supervisor Prof. Dr. Thomas Pertsch, for giving me the opportunity to become a member of his group and for the immense guidance and support that he offered me during my Ph.D. I benefited significantly from his insightful comments and valuable suggestions. My sincere gratitude goes to Dr. Frank Setzpfandt for his precious involvement in my research. His patience during long hours of discussion and insightful questions always provided me with new perspectives. I appreciate the time that you have spent polishing all my writings.

I would like to thank Dennis Arslan and Dr. Angela Barreda for fruitful discussions and exchanging ideas concerning my measurements and also for sharing their knowledge and deep understanding of the theoretical models and numerical simulations, Mohamadreza Younsei, who always had creative ideas in programming, and Dr. Jonas Berzin for being helpful with my questions about numerical simulations. My special thanks go to Michael Steinert for his patience while characterizing many SNOM tips and retrieving many of them with perfect Focus Ion Beam cuts and Stefan Fasold for fabricating silicon nanodisk metasurfaces. Without Daniel Füßel, the Nano and Quantum Optics group would be dysfunctional. I would like to thank him for supporting me with many technical issues which could not have been solved without his help.

I would like to extend my sincere gratitude to Adam Kollin for accepting the challenge of developing a customized controller for automating dual-tip SNOM measurements, Kenneth Kollin, and Dr. Stefan Porthun for developing the automated

scan's algorithm and willingly applying my suggestions to improve the overall performance of the automated scan. The accomplishment of this work would not have been possible without the constant support that I received from the RHK company as a first customer of the dual-tip SNOM controller. Thank you for inviting me to visit the company and making my stay a wonderful experience.

I am very grateful to Dr. Franz Löchner, Dr. Angela Klein, Dr. Bita Malekian, and Dr. Marjan Famili for proofreading different parts of my dissertation. The comments and input you provided were always constructive and helped me improve the flow and readability of my writing.

All my colleagues in the quantum and nano-optics group deserve a huge appreciation for the wonderful environment they have created. I appreciate the openness that you always offered for scientific and nonscientific discussions. Furthermore, I was fortunate to have Anna Fedottova and Dr. Franz Löchner as my office mates. Beyond the empathy and support you have given me during the challenging moments, you have been part of many pleasant life-lasting memories for me.

It took more than academic support to get through my academic journey from the beginning. I would like to express my gratitude to Dr. Dorit Schmidt, Dr. Anna Späthe, and Dr. Christian Helgert. I cannot imagine a better executive team for Abbe School of Photonics. Your tremendous support and help throughout all bureaucratic issues and personal challenges I have faced since my arrival in Germany are priceless.

Last but not least, I would like to acknowledge my family and friends; without their unconditional love and support, I would not have accomplished this thesis. I am so lucky that beyond endless support and encouragement from my parents, my siblings have been a source of inspiration and joy throughout my life.

D

Ehrenwörtliche Erklärung

Ich erkläre hiermit ehrenwörtlich, dass ich die vorliegende Arbeit selbständig, ohne unzulässige Hilfe Dritter und ohne Benutzung anderer als der angegebenen Hilfsmittel und Literatur angefertigt habe. Die aus anderen Quellen direkt oder indirekt übernommenen Daten und Konzepte sind unter Angabe der Quelle gekennzeichnet.

Bei der Auswahl und Auswertung folgenden Materials haben mir die nachstehend aufgeführten Personen in der jeweils beschriebenen Weise unentgeltlich geholfen:

1. Die Silizium-Metasurfaces wurden von Dennis Arslan entworfen, und er führte die Berechnung des Scattering cross section in Kapitel 6 durch.

2. Stefan Fasold stellte die Nanoplatten-Metasurfaces her.

3. Michael Steinert nahm die REM-Bilder der SNOM-Spitzen auf und behandelte sie mit dem Focused Ion Beam.

4. Yu-Ju Chen vom Leibniz-Institut für Photonische Technologien stellte die Goldplaettchen her.

Weitere Personen waren an der inhaltlich-materiellen Erstellung der vorliegenden Arbeit nicht beteiligt. Insbesondere habe ich hierfür nicht die entgeltliche Hilfe von Vermittlungs- bzw. Beratungsdiensten (Promotionsberater oder andere Personen) in Anspruch genommen.

Niemand hat von mir unmittelbar oder mittelbar geldwerte Leistungen für Arbeiten erhalten, die im Zusammenhang mit dem Inhalt der vorgelegten Dissertation stehen.

Die Arbeit wurde bisher weder im In- noch im Ausland in gleicher oder ähnlicher Form einer anderen Prüfungsbehörde vorgelegt. Die geltende Promotionsordnung der Physikalisch-Astronomischen Fakultät ist mir bekannt.

Ich versichere ehrenwörtlich, dass ich nach bestem Wissen die reine Wahrheit gesagt und nichts verschwiegen habe.

Jena, 29.03.2022 Najmeh Abbasirad

Bibliography

[1] Lukas Novotny. The history of near-field optics. *Progress in optics*, 50:137, 2007.

[2] Marcel A Lauterbach. Finding, defining and breaking the diffraction barrier in microscopy–a historical perspective. *Optical nanoscopy*, 1(1):1–8, 2012.

[3] Lord Rayleigh. Xv. on the theory of optical images, with special reference to the microscope. *The London, Edinburgh, and Dublin Philosophical Magazine and Journal of Science*, 42(255):167–195, 1896.

[4] Lukas Novotny and Bert Hecht. *Principles of Nano-Optics*. Cambridge University Press, 2012.

[5] Jean Jacques Greffet and Rémi Carminati. Image formation in near-field optics. *Progress in Surface Science*, 56(3):133–237, 1997.

[6] EdwardH Synge. Xxxviii. a suggested method for extending microscopic resolution into the ultra-microscopic region. *The London, Edinburgh, and Dublin Philosophical Magazine and Journal of Science*, 6(35):356–362, 1928.

[7] Y Kuk and PJ Silverman. Scanning tunneling microscope instrumentation. *Review of scientific instruments*, 60(2):165–180, 1989.

[8] Dieter W Pohl, Winfried Denk, and Mark Lanz. Optical stethoscopy: Image recording with resolution $\lambda/20$. *Applied Physics Letters*, 44(7):651–653, 1984.

[9] A. Lewis, M. Isaacson, A. Harootunian, and A. Muray. Development of a 500 Å spatial resolution light microscope. I. light is efficiently transmitted through $\lambda/16$ diameter apertures. *Ultramicroscopy*, 13(3):227–231, 1984.

[10] Bert Hecht, Beate Sick, Urs P. Wild, Volker Deckert, Renato Zenobi, Olivier J.F. Martin, and Dieter W. Pohl. Scanning near-field optical microscopy with aperture probes: Fundamentals and applications. *Journal of Chemical Physics*, 112(18):7761–7774, 2000.

[11] Marek W Kowarz. Homogeneous and evanescent contributions in scalar near-field diffraction. *Applied Optics*, 34(17):3055–3063, 1995.

[12] J. Michaelis, C. Hettich, J. Mlynek, and V. Sandoghdar. Optical microscopy using a single-molecule light source. *Nature*, 405(6784):325–328, 2000.

[13] Aurélien Drezet, Aurélien Cuche, and Serge Huant. Near-field microscopy with a single-photon point-like emitter: Resolution versus the aperture tip? *Optics Communications*, 284(5):1444–1450, 2011.

[14] Dmitri K. Gramotnev and Sergey I. Bozhevolnyi. Plasmonics beyond the diffraction limit. *Nature Photonics*, 4(2):83–91, 2010.

[15] Mark S Tame, KR McEnery, ŞK Özdemir, Jinhyoung Lee, Stefan A Maier, and MS Kim. Quantum plasmonics. *Nature Physics*, 9(6):329–340, 2013.

[16] A Femius Koenderink, Andrea Alu, and Albert Polman. Nanophotonics: Shrinking light-based technology. *Science*, 348(6234):516–521, 2015.

[17] Wyatt Adams, Mehdi Sadatgol, and Durdu Ö Güney. Review of near-field optics and superlenses for sub-diffraction-limited nano-imaging. *AIP Advances*, 6(10):100701, 2016.

[18] Paul Bazylewski, Sabastine Ezugwu, and Giovanni Fanchini. A review of three-dimensional scanning near-field optical microscopy (3d-snom) and its applications in nanoscale light management. *Applied Sciences*, 7(10):973, 2017.

[19] Stefan Alexander Maier. *Plasmonics: fundamentals and applications*. Springer Science & Business Media, 2007.

[20] B Hecht, H Bielefeldt, L Novotny, Y Inouye, and DW Pohl. Local excitation, scattering, and interference of surface plasmons. *Physical Review Letters*, 77(9):1889, 1996.

[21] Hans Albrecht Bethe. Theory of diffraction by small holes. *Physical Review*, 66(7-8):163, 1944.

[22] CJ Bouwkamp. On bethe's theory of diffraction by small holes. *Philips Research Reports*, 5:321–332, 1950.

[23] Christian Obermüller and Khaled Karrai. Far field characterization of diffracting circular apertures. *Applied Physics Letters*, 67(23):3408–3410, 1995.

[24] C Obermüller, K Karrai, G Kolb, and G Abstreiter. Transmitted radiation through a subwavelength-sized tapered optical fiber tip. *Ultramicroscopy*, 61(1-4):171–177, 1995.

[25] DJ Shin, A Chavez-Pirson, SH Kim, ST Jung, and Yong-Hee Lee. Diffraction by a subwavelength-sized aperture in a metal plane. *JOSA A*, 18(7):1477–1486, 2001.

[26] N Rotenberg, TL Krijger, B Le Feber, M Spasenović, F Javier Garcia de Abajo, and L Kuipers. Magnetic and electric response of single subwavelength holes. *Physical Review B*, 88(24):241408, 2013.

[27] Eloïse Devaux, Alain Dereux, Eric Bourillot, Jean-Claude Weeber, Yvon Lacroute, Jean-Pierre Goudonnet, and Christian Girard. Local detection of the optical magnetic field in the near zone of dielectric samples. *Physical Review B*, 62(15):10504, 2000.

[28] A Drezet, JC Woehl, and S Huant. Extension of bethe's diffraction model to conical geometry: Application to near-field optics. *EPL (Europhysics Letters)*, 54(6):736, 2001.

[29] Dilip K. Singh, Jae Sung Ahn, Sukmo Koo, Taehee Kang, Joonyeon Kim, Sukho Lee, Namkyoo Park, and Dai-Sik Kim. Selective electric and magnetic sensitivity of aperture probes. *Optics Express*, 23(16):20820, 2015.

[30] S Schmidt, AE Klein, T Paul, H Gross, S Diziain, M Steinert, AC Assafrao, T Pertsch, HP Urbach, and C Rockstuhl. Image formation properties and inverse imaging problem in aperture based scanning near field optical microscopy. *Optics Express*, 24(4):4128–4142, 2016.

[31] Martin Frimmer, Yuntian Chen, and A. Femius Koenderink. Scanning emitter lifetime imaging microscopy for spontaneous emission control. *Physical Review Letters*, 107(12):1–5, 2011.

[32] V. Krachmalnicoff, D. Cao, A. Cazé, E. Castanié, R. Pierrat, N. Bardou, S. Collin, R. Carminati, and Y. De Wilde. Towards a full characterization of a plasmonic nanostructure with a fluorescent near-field probe. *Optics Express*, 21(9):11536, 2013.

[33] N Chevalier, MJ Nasse, JC Woehl, P Reiss, J Bleuse, F Chandezon, and S Huant. Cdse single-nanoparticle based active tips for near-field optical microscopy. *Nanotechnology*, 16(4):613, 2005.

[34] Thi Phuong Lien Ung, Rabeb Jazi, Julien Laverdant, Rémy Fulcrand, Gérard Colas Des Francs, Jean-Pierre Hermier, Xavier Quélin, and Stéphanie Buil. Scanning the plasmonic properties of a nanohole array with a single nanocrystal near-field probe. *Nanophotonics*, 9(4):793–801, 2020.

[35] Aurélien Cuche, Oriane Mollet, Aurélien Drezet, and Serge Huant. "deterministic" quantum plasmonics. *Nano Letters*, 10(11):4566–4570, 2010.

[36] L Aigouy, A Cazé, P Gredin, M Mortier, and R Carminati. Mapping and quantifying electric and magnetic dipole luminescence at the nanoscale. *Physical Review Letters*, 113(7):076101, 2014.

[37] A. Cuche, M. Berthel, U. Kumar, G. Colas Des Francs, S. Huant, E. Dujardin, C. Girard, and A. Drezet. Near-field hyperspectral quantum probing of multimodal plasmonic resonators. *Physical Review B*, 95(12):1–5, 2017.

[38] Clément Majorel, Christian Girard, Aurélien Cuche, Arnaud Arbouet, and Peter R. Wiecha. Quantum theory of near-field optical imaging with rare-earth atomic clusters. *Journal of the Optical Society of America B*, 37(5):1474, 2020.

[39] Eric Betzig and Robert J. Chichester. Single molecules observed by near-field scanning optical microscopy. *Science*, 262(5138):1422–1425, 1993.

[40] Randy X Bian, Robert C Dunn, X Sunney Xie, and PT Leung. Single molecule emission characteristics in near-field microscopy. *Physical Review Letters*, 75(26):4772, 1995.

[41] Pascal Anger, Palash Bharadwaj, and Lukas Novotny. Enhancement and quenching of single-molecule fluorescence. *Physical Review Letters*, 96(11):3–6, 2006.

[42] William L Barnes, Simon AR Horsley, and Willem L Vos. Classical antennas, quantum emitters, and densities of optical states. *Journal of Optics*, 22(7):073501, 2020.

[43] Gérard Colas des Francs, Christian Girard, Jean-Claude Weeber, Cédric Chicane, Thierry David, Alain Dereux, and David Peyrade. Optical analogy to electronic quantum corrals. *Physical Review Letters*, 86(21):4950, 2001.

[44] Gérard Colas Des Francs, Christian Girard, Jean Claude Weeber, and Alain Dereux. Relationship between scanning near-field optical images and local density of photonic states. *Chemical Physics Letters*, 345(5-6):512–516, 2001.

[45] Cédric Chicanne, Thierry David, R Quidant, Jean-Claude Weeber, Y Lacroute, Eric Bourillot, Alain Dereux, G Colas Des Francs, and Christian Girard. Imaging the local density of states of optical corrals. *Physical Review Letters*, 88(9):097402, 2002.

[46] A. Dereux, Ch Girard, C. Chicanne, G. Colas Des Francs, T. David, E. Bourillot, Y. Lacroute, and J. C. Weeber. Subwavelength mapping of surface photonic states. *Nanotechnology*, 14(8):935–938, 2003.

[47] Henk F. Arnoldus and John T. Foley. Spatial separation of the traveling and evanescent parts of dipole radiation. *Optics Letters*, 28(15):1299, 2003.

[48] Angela E Klein, Norik Janunts, Michael Steinert, Andreas Tünnermann, and Thomas Pertsch. Polarization-resolved near-field mapping of plasmonic aperture emission by a dual-snom system. *Nano Letters*, 14(9):5010–5015, 2014.

[49] Sergei Slussarenko and Geoff J Pryde. Photonic quantum information processing: A concise review. *Applied Physics Reviews*, 6(4):041303, 2019.

[50] Alexandre Blais, Steven M Girvin, and William D Oliver. Quantum information processing and quantum optics with circuit quantum electrodynamics. *Nature Physics*, 16(3):247–256, 2020.

[51] Christian L Degen, F Reinhard, and Paola Cappellaro. Quantum sensing. *Reviews of Modern Physics*, 89(3):035002, 2017.

[52] Stefano Pirandola, B Roy Bardhan, Tobias Gehring, Christian Weedbrook, and Seth Lloyd. Advances in photonic quantum sensing. *Nature Photonics*, 12(12):724–733, 2018.

[53] Tuvia Gefen, Amit Rotem, and Alex Retzker. Overcoming resolution limits with quantum sensing. *Nature Communications*, 10(1):1–9, 2019.

[54] Peter Lodahl, Sahand Mahmoodian, and Søren Stobbe. Interfacing single photons and single quantum dots with photonic nanostructures. *Reviews of Modern Physics*, 87(2):347, 2015.

[55] Da Cao, Alexandre Cazé, Michele Calabrese, Romain Pierrat, Nathalie Bardou, Stéphane Collin, Rémi Carminati, Valentina Krachmalnicoff, and Yannick De Wilde. Mapping the radiative and the apparent nonradiative local density of states in the near field of a metallic nanoantenna. *ACS Photonics*, 2(2):189–193, 2015.

[56] A. Femius Koenderink. Single-Photon Nanoantennas. *ACS Photonics*, 4(4):710–722, 2017.

[57] Peter Lodahl, A Floris Van Driel, Ivan S Nikolaev, Arie Irman, Karin Overgaag, Daniël Vanmaekelbergh, and Willem L Vos. Controlling the dynamics of spontaneous emission from quantum dots by photonic crystals. *Nature*, 430(7000):654–657, 2004.

[58] Dirk Englund, David Fattal, Edo Waks, Glenn Solomon, Bingyang Zhang, Toshihiro Nakaoka, Yasuhiko Arakawa, Yoshihisa Yamamoto, and Jelena Vučković. Controlling the spontaneous emission rate of single quantum dots in a two-dimensional photonic crystal. *Physical Review Letters*, 95(1):013904, 2005.

[59] Aleksandr Vaskin, Radoslaw Kolkowski, A Femius Koenderink, and Isabelle Staude. Light-emitting metasurfaces. *Nanophotonics*, 8(7):1151–1198, 2019.

[60] TH Taminiau, FD Stefani, Franciscus B Segerink, and NF Van Hulst. Optical antennas direct single-molecule emission. *Nature Photonics*, 2(4):234–237, 2008.

[61] Maria Sanz-Paz, Cyrine Ernandes, Juan Uriel Esparza, Geoffrey W. Burr, Niek F. Van Hulst, Agnès Maitre, Lionel Aigouy, Thierry Gacoin, Nicolas Bonod, Maria F. Garcia-Parajo, Sébastien Bidault, and Mathieu Mivelle. Enhancing Magnetic Light Emission with All-Dielectric Optical Nanoantennas. *Nano Letters*, 18(6):3481–3487, 2018.

[62] A. Drezet, Y. Sonnefraud, A. Cuche, O. Mollet, M. Berthel, and S. Huant. Near-field microscopy with a scanning nitrogen-vacancy color center in a diamond nanocrystal: A brief review. *Micron*, 70:55–63, 2015.

[63] Ravitej Uppu, Leonardo Midolo, Xiaoyan Zhou, Jacques Carolan, and Peter Lodahl. Quantum-dot-based deterministic photon–emitter interfaces for scalable photonic quantum technology. *Nature Nanotechnology*, 16(12):1308–1317, 2021.

[64] B. Le Feber, N. Rotenberg, and L. Kuipers. Nanophotonic control of circular dipole emission. *Nature Communications*, 6:1–6, 2015.

[65] Jean Claude Weeber, Yvon Lacroute, and Alain Dereux. Optical near-field distributions of surface plasmon waveguide modes. *Physical Review B - Condensed Matter and Materials Physics*, 68(11):1–10, 2003.

[66] Rashid Zia, Jon A. Schuller, and Mark L. Brongersma. Near-field characterization of guided polariton propagation and cutoff in surface plasmon waveguides. *Physical Review B - Condensed Matter and Materials Physics*, 74(16):1–12, 2006.

[67] A. Bouhelier, F. Ignatovich, A. Bruyant, C. Huang, G. Colas des Francs, J.-C. Weeber, A. Dereux, G. P. Wiederrecht, and L. Novotny. Surface plasmon interference excited by tightly focused laser beams. *Optics Letters*, 32(17):2535, 2007.

[68] Petr Dvořák, Tomáš Neuman, Lukáš Břínek, Tomáš Šamořil, Radek Kalousek, Petr Dub, Peter Varga, and Tomáš Šikola. Control and near-field detection of surface plasmon interference patterns. *Nano Letters*, 13(6):2558–2563, 2013.

[69] Petr Dvořák, Zoltán Édes, Michal Kvapil, Tomáš Šamořil, Filip Ligmajer, Martin Hrtoň, Radek Kalousek, Vlastimil Křápek, Petr Dub, Jiří Spousta, Peter Varga, and Tomáš Šikola. Imaging of near-field interference patterns by aperture-type SNOM – influence of illumination wavelength and polarization state. *Optics Express*, 25(14):16560, 2017.

[70] Takuya Matsuura, Keisuke Imaeda, Seiju Hasegawa, Hiromasa Suzuki, and Kohei Imura. Characterization of overlapped plasmon modes in a gold hexagonal plate revealed by three-dimensional near-field optical microscopy. *Journal of Physical Chemistry Letters*, 10(4):819–824, 2019.

[71] Keisuke Imaeda, Wataru Minoshima, Keiko Tawa, and Kohei Imura. Direct Visualization of Near-Field Distributions on a Two-Dimensional Plasmonic Chip by Scanning Near-Field Optical Microscopy. *Journal of Physical Chemistry C*, 123(16):10529–10535, 2019.

[72] Koichi Okamoto, Marko Lončar, Tomoyuki Yoshie, Axel Scherer, Yueming Qiu, and Pawan Gogna. Near-field scanning optical microscopy of photonic crystal nanocavities. *Applied Physics Letters*, 82(11):1676–1678, 2003.

[73] Silvia Vignolini, Francesca Intonti, Francesco Riboli, Laurent Balet, Lianhe H Li, Marco Francardi, Annamaria Gerardino, Andrea Fiore, Diederik S Wiersma, and Massimo Gurioli. Magnetic imaging in photonic crystal microcavities. *Physical Review Letters*, 105(12):123902, 2010.

[74] M Burresi, T Kampfrath, D Van Oosten, JC Prangsma, BS Song, S Noda, and L Kuipers. Magnetic light-matter interactions in a photonic crystal nanocavity. *Physical Review Letters*, 105(12):123901, 2010.

[75] A. Femius Koenderink, Maria Kafesaki, Ben C. Buchler, and Vahid Sandoghdar. Controlling the resonance of a photonic crystal microcavity by a near-field probe. *Physical Review Letters*, 95(15):1–4, 2005.

[76] S. Mujumdar, A. F. Koenderink, T. Sünner, B. C. Buchler, M. Kamp, A. Forchel, and V. Sandoghdar. Near-field imaging and frequency tuning of a high-Q photonic crystal membrane microcavity. *Optics Express*, 15(25):17214, 2007.

[77] L Lalouat, B Cluzel, P Velha, E Picard, D Peyrade, Jean-Paul Hugonin, Philippe Lalanne, E Hadji, and F De Fornel. Near-field interactions between a subwavelength tip and a small-volume photonic-crystal nanocavity. *Physical Review B*, 76(4):041102, 2007.

[78] R Rezvani Naraghi, S Sukhov, and A Dogariu. Disorder fingerprint: intensity distributions in the near field of random media. *Physical Review B*, 94(17):174205, 2016.

[79] Valentina Parigi, Elodie Perros, Guillaume Binard, Céline Bourdillon, Agnès Maître, Rémi Carminati, Valentina Krachmalnicoff, and Yannick De Wilde. Near-field to far-field characterization of speckle patterns generated by disordered nanomaterials. *Optics Express*, 24(7):7019–7027, 2016.

[80] Niccolò Caselli, Francesca Intonti, Federico La China, Francesco Biccari, Francesco Riboli, Annamaria Gerardino, Lianhe Li, Edmund H Linfield, Francesco Pagliano, Andrea Fiore, et al. Generalized fano lineshapes reveal exceptional points in photonic molecules. *Nature communications*, 9(1):1–8, 2018.

[81] Niccolò Caselli, Francesco Riboli, Federico La China, Annamaria Gerardino, Lianhe Li, Edmund H Linfield, Francesco Pagliano, Andrea Fiore, Francesca Intonti, and Massimo Gurioli. Tailoring the photon hopping by nearest-neighbor and next-nearest-neighbor interaction in photonic arrays. *ACS Photonics*, 2(5):565–571, 2015.

[82] KG Cognée, Wei Yan, F La China, D Balestri, F Intonti, M Gurioli, AF Koenderink, and Philippe Lalanne. Mapping complex mode volumes with cavity perturbation theory. *Optica*, 6(3):269–273, 2019.

[83] Niccolo Caselli, Tong Wu, Guillermo Arregui, Nicoletta Granchi, Francesca Intonti, Philippe Lalanne, and Massimo Gurioli. Near-field imaging of magnetic complex mode volume. *ACS Photonics*, 8(5):1258–1263, 2021.

[84] Francesco Riboli, Niccolò Caselli, Silvia Vignolini, Francesca Intonti, Kevin Vynck, Pierre Barthelemy, Annamaria Gerardino, Laurent Balet, Lianhe H Li, Andrea Fiore, et al. Engineering of light confinement in strongly scattering disordered media. *Nature Materials*, 13(7):720–725, 2014.

[85] Niccolò Caselli, Francesca Intonti, Federico La China, Francesco Biccari, Francesco Riboli, Annamaria Gerardino, Lianhe Li, Edmund H Linfield, Francesco Pagliano, Andrea Fiore, et al. Near-field speckle imaging of light localization in disordered photonic systems. *Applied Physics Letters*, 110(8):081102, 2017.

[86] Kevin Vynck, Romain Pierrat, Rémi Carminati, Luis S Froufe-Pérez, Frank Scheffold, Riccardo Sapienza, Silvia Vignolini, and Juan José Sáenz. Light in correlated disordered media. *arXiv preprint arXiv:2106.13892*, 2021.

[87] R. Carminati, A. Cazé, D. Cao, F. Peragut, V. Krachmalnicoff, R. Pierrat, and Y. De Wilde. Electromagnetic density of states in complex plasmonic systems. *Surface Science Reports*, 70(1):1–41, 2015.

[88] A Cazé, R Pierrat, and R Carminati. Spatial coherence in complex photonic and plasmonic systems. *Physical Review Letters*, 110(6):063903, 2013.

[89] Aristide Dogariu and Remi Carminati. Electromagnetic field correlations in three-dimensional speckles. *Physics Reports*, 559:1–29, 2015.

[90] Kaizad Rustomji, Marc Dubois, Pierre Jomin, Stefan Enoch, Jérôme Wenger, C Martijn de Sterke, and Redha Abdeddaim. Complete electromagnetic dyadic green function characterization in a complex environment—resonant dipole-dipole interaction and cooperative effects. *Physical Review X*, 11(2):021004, 2021.

[91] Boris Le Feber, John E Sipe, Matthias Wulf, Laurens Kuipers, and N Rotenberg. A full vectorial mapping of nanophotonic light fields. *Light: Science & Applications*, 8(1):1–7, 2019.

[92] Ramona Dallapiccola, C Dubois, A Gopinath, Francesco Stellacci, and L Dal Negro. Near-field excitation and near-field detection of propagating surface plasmon polaritons on au waveguide structures. *Applied Physics Letters*, 94(24):243118, 2009.

[93] Xifeng Ren, Aiping Liu, Changling Zou, Lulu Wang, Yongjing Cai, Fangwen Sun, Guangcan Guo, and Guoping Guo. Interference of surface plasmon polaritons from a "point" source. *Applied Physics Letters*, 98(20):201113, 2011.

[94] R Fujimoto, A Kaneta, K Okamoto, M Funato, and Y Kawakami. Interference of the surface plasmon polaritons with an ag waveguide probed by dual-probe scanning near-field optical microscopy. *Applied Surface Science*, 258(19):7372–7376, 2012.

[95] Aiping Liu, Chang-Ling Zou, Xifeng Ren, Xiao Xiong, Yong-Jing Cai, Haitao Liu, Fang-Wen Sun, Guang-Can Guo, and Guo-Ping Guo. Independently analyzing different surface plasmon polariton modes on silver nanowire. *Optics Express*, 22(19):23372–23378, 2014.

[96] Angela E Klein, Norik Janunts, Sören Schmidt, Shakeeb Bin Hasan, Christoph Etrich, Stefan Fasold, Thomas Kaiser, Carsten Rockstuhl, and Thomas Pertsch. Dual-snom investigations of multimode interference in plasmonic strip waveguides. *Nanoscale*, 9(20):6695–6702, 2017.

[97] Yuta Masaki, Keita Tomita, Yasuhiro Kojima, and Fumihiko Kannari. Measurement of propagation of ultrafast surface plasmon polariton pulses using dual-probe scanning near-field optical microscopy. *Applied Optics*, 58(21):5595–5601, 2019.

[98] Akio Kaneta, Tsuneaki Hashimoto, Katsuhito Nishimura, Mitsuru Funato, and Yoichi Kawakami. Visualization of the local carrier dynamics in an ingan quantum well using dual-probe scanning near-field optical microscopy. *Applied Physics Express*, 3(10):102102, 2010.

[99] Akio Kaneta, Ryo Fujimoto, Tsuneaki Hashimoto, Katsuhito Nishimura, Mitsuru Funato, and Yoichi Kawakami. Instrumentation for dual-probe scanning near-field optical microscopy. *Review of Scientific Instruments*, 83(8):083709, 2012.

[100] A. E. Klein, N. Janunts, A. Tunnermann, and T. Pertsch. Investigation of mechanical interactions between the tips of two scanning near-field optical microscopes. *Applied Physics B: Lasers and Optics*, 108(4):737–741, 2012.

[101] Angela Elisabeth Klein. *Scanning near-field optical microscopy: from single-tip to dual-tip operation*. PhD thesis, Thüringer Universitäts-und Landesbibliothek Jena, 2015.

[102] Tomonobu Nakayama, Yoshitaka Shingaya, and Masakazu Aono. Multiple-probe scanning probe microscopes for nanoarchitectonic materials science. *Japanese Journal of Applied Physics*, 55(11), 2016.

[103] Bert Voigtländer, Vasily Cherepanov, Stefan Korte, Arthur Leis, David Cuma, Sven Just, and Felix Lüpke. Invited review article: Multi-tip scanning tunneling microscopy: Experimental techniques and data analysis. *Review of Scientific Instruments*, 89(10):101101, 2018.

[104] Nancy M. Haegel. Integrating electron and near-field optics: Dual vision for the nanoworld. *Nanophotonics*, 3(1-2):75–89, 2014.

[105] Ann Roberts. Small-hole coupling of radiation into a near-field probe. *Journal of Applied Physics*, 70(8):4045–4049, 1991.

[106] Bert Voigtländer. *Atomic Force Microscopy*. Springer, 2019.

[107] Najmeh Abbasirad, Jonas Berzins, Kenneth Kollin, Sina Saravi, Norik Janunts, Frank Setzpfandt, and Thomas Pertsch. A fully automated dual-tip scanning near-field optical microscope for localized optical excitation and detection in the visible and near-infrared. *Review of Scientific Instruments*, 90(5):053705, 2019.

[108] Paul E West. Introduction to atomic force microscopy theory, practice, applications. 2007.

[109] B. Hecht, H. Bielefeldt, Y. Inouye, D. W. Pohl, and L. Novotny. Facts and artifacts in near-field optical microscopy. *Journal of Applied Physics*, 81(6):2492–2498, 1997.

[110] Lukas Novotny and Niek Van Hulst. Antennas for light. *Nature Photonics*, 5(2):83–90, 2011.

[111] Lin Sun, Benfeng Bai, Xiaoxia Meng, Tong Cui, Guangyi Shang, and Jia Wang. Near-field probing the magnetic field vector of visible light with a silicon nanoparticle probe and nanopolarimetry. *Optics Express*, 26(19):24637, 2018.

[112] P. James Schuck, Wei Bao, and Nicholas J. Borys. A polarizing situation: Taking an in-plane perspective for next-generation near-field studies. *Frontiers of Physics*, 11(2):1–17, 2016.

[113] Shiyi Xiao, Jiarong Wang, Fu Liu, Shuang Zhang, Xiaobo Yin, and Jensen Li. Spin-dependent optics with metasurfaces. *Nanophotonics*, 6(1):215–234, 2017.

[114] Konstantin Yu Bliokh, Francisco J Rodríguez-Fortuño, Franco Nori, and Anatoly V Zayats. Spin–orbit interactions of light. *Nature Photonics*, 9(12):796–808, 2015.

[115] J David Jackson. Electrodynamics. *The Optics Encyclopedia: Basic Foundations and Practical Applications*, 2007.

[116] N Rotenberg and L Kuipers. Mapping nanoscale light fields. *Nature Photonics*, 8(12):919–926, 2014.

[117] B Feber, N Rotenberg, D M Beggs, and L Kuipers. Simultaneous measurement of nanoscale electric and magnetic optical fields. *Nature Photonics*, 8(1):43–46, 2013.

[118] I. V. Kabakova, A. De Hoogh, R. E.C. Van Der Wel, M. Wulf, B. Le Feber, and L. Kuipers. Imaging of electric and magnetic fields near plasmonic nanowires. *Scientific Reports*, 6(March):1–9, 2016.

[119] HW Kihm, SM Koo, QH Kim, K Bao, JE Kihm, WS Bak, SH Eah, C Lienau, H Kim, P Nordlander, et al. Bethe-hole polarization analyser for the magnetic vector of light. *Nature Communications*, 2(1):1–6, 2011.

[120] Hyun Woo Kihm, Jineun Kim, Sukmo Koo, Jaesung Ahn, Kwangjun Ahn, Kwanggeol Lee, Namkyoo Park, and Dai-Sik Kim. Optical magnetic field mapping using a subwavelength aperture. *Optics Express*, 21(5):5625–5633, 2013.

[121] Denitza Denkova, Niels Verellen, Alejandro V. Silhanek, Ventsislav K. Valev, Pol Van Dorpe, and Victor V. Moshchalkov. Mapping magnetic near-field distributions of plasmonic nanoantennas. *ACS Nano*, 7(4):3168–3176, 2013.

[122] Denitza Denkova, Niels Verellen, Alejandro V. Silhanek, Pol Van Dorpe, and Victor V. Moshchalkov. Lateral magnetic near-field imaging of plasmonic nanoantennas with increasing complexity. *Small*, 10(10):1959–1966, 2014.

[123] M. Burresi, D. Van Oosten, T. Kampfrath, H. Schoenmaker, R. Heideman, A. Leinse, and L. Kuipers. Probing the magnetic field of light at optical frequencies. *Science*, 326(5952):550–553, 2009.

[124] B. Le Feber, N. Rotenberg, D. M. Beggs, and L. Kuipers. Simultaneous measurement of nanoscale electric and magnetic optical fields. *Nature Photonics*, 8(1):43–46, 2014.

[125] Ursula Schröter and Alain Dereux. Surface plasmon polaritons on metal cylinders with dielectric core. *Physical Review B*, 64(12):125420, 2001.

[126] Lin Sun, Benfeng Bai, and Jia Wang. Probing vectorial near field of light: imaging theory and design principles of nanoprobes. *Optics Express*, 26(14):18644–18663, 2018.

[127] Najmeh Abbasirad, Angela Barreda, Yi-Ju Chen, Jer-Shing Huang, Isabelle Staude, Frank Setzpfandt, and Thomas Pertsch. Near-field launching and mapping unidirectional surface plasmon polaritons using an automated dual-tip scanning near-field optical microscope. *Photonics Research*, 10(11):2628–2641, 2022.

[128] A. Drezet, A. Hohenau, J. R. Krenn, M. Brun, and S. Huant. Surface plasmon mediated near-field imaging and optical addressing in nanoscience. *Micron*, 38(4):427–437, 2007.

[129] Junxi Zhang, Lide Zhang, and Wei Xu. Surface plasmon polaritons: physics and applications. *Journal of Physics D: Applied Physics*, 45(11):113001, 2012.

[130] Pierre Berini and Israel De Leon. Surface plasmon–polariton amplifiers and lasers. *Nature Photonics*, 6(1):16–24, 2012.

[131] Sergey I. Bozhevolnyi and N. Asger Mortensen. Plasmonics for emerging quantum technologies. *Nanophotonics*, 6(5):1185–1188, 2017.

[132] Jian-Ying Jing, Qi Wang, Wan-Ming Zhao, and Bo-Tao Wang. Long-range surface plasmon resonance and its sensing applications: A review. *Optics and Lasers in Engineering*, 112:103–118, 2019.

[133] Isaac Suárez, Albert Ferrando, Jose Marques-Hueso, Antonio Díez, Rafael Abargues, Pedro J Rodríguez-Cantó, and Juan P Martínez-Pastor. Propagation length enhancement of surface plasmon polaritons in gold nano-/microwaveguides by the interference with photonic modes in the surrounding active dielectrics. *Nanophotonics*, 6(5):1109–1120, 2017.

[134] Adelmo S Souza, Vinicius Coelho, and Jorge Luís O Santos. General conditions of confinement of the electromagnetic wave at the metal-dielectric interface. *Brazilian Journal of Physics*, 51(3):449–460, 2021.

[135] Mohammad Amin Izadi and Rahman Nouroozi. Adjustable propagation length enhancement of the surface plasmon polariton wave via phase sensitive optical parametric amplification. *Scientific Reports*, 8(1):1–14, 2018.

[136] Aurélien Drezet, Andreas Hohenau, Daniel Koller, Andrey Stepanov, H Ditlbacher, Bernhard Steinberger, Franz Rembert Aussenegg, Alfred Leitner, and Joachim Rudolf Krenn. Leakage radiation microscopy of surface plasmon polaritons. *Materials Science and Engineering: B*, 149(3):220–229, 2008.

[137] Andrei Kolomenski, Alexandre Kolomenskii, John Noel, Siying Peng, and Hans Schuessler. Propagation length of surface plasmons in a metal film with roughness. *Applied Optics*, 48(30):5683, 2009.

[138] Kevin M. McPeak, Sriharsha V. Jayanti, Stephan J.P. Kress, Stefan Meyer, Stelio Iotti, Aurelio Rossinelli, and David J. Norris. Plasmonic films can easily be better: Rules and recipes. *ACS Photonics*, 2(3):326–333, 2015.

[139] Xiaofei Wu, René Kullock, Enno Krauss, and Bert Hecht. Single-crystalline gold microplates grown on substrates by solution-phase synthesis. *Crystal Research and Technology*, 50(8):595–602, 2015.

[140] Enno Krauss, Rene Kullock, Xiaofei Wu, Peter Geisler, Nils Lundt, Martin Kamp, and Bert Hecht. Controlled growth of high-aspect-ratio single-crystalline gold platelets. *Crystal Growth & Design*, 18(3):1297–1302, 2018.

[141] R Méjard, A Verdy, O Demichel, M Petit, L Markey, F Herbst, R Chassagnon, G Colas-des Francs, B Cluzel, and A Bouhelier. Advanced engineering of single-crystal gold nanoantennas. *Optical Materials Express*, 7(4):1157–1168, 2017.

[142] M. Prämassing, M. Liebtrau, H. J. Schill, S. Irsen, and S. Linden. Interferometric near-field characterization of plasmonic slot waveguides in single- and poly-crystalline gold films. *Optics Express*, 28(9):12998, 2020.

[143] Korbinian J Kaltenecker, Enno Krauss, Laura Casses, Mathias Geisler, Bert Hecht, N Asger Mortensen, Peter Uhd Jepsen, and Nicolas Stenger. Monocrystalline gold platelets: a high-quality platform for surface plasmon polaritons. *Nanophotonics*, 9(2):509–522, 2020.

[144] Yasuyuki Mitsuoka, Kunio Nakajima, Katsunori Homma, Norio Chiba, Hiroshi Muramatsu, Tatsuaki Ataka, and Katsuaki Sato. Polarization properties of light emitted by a bent optical fiber probe and polarization contrast in scanning near-field optical microscopy. *Journal of Applied Physics*, 83(8):3998–4003, 1998.

[145] L Ramoino, M Labardi, N Maghelli, Lucio Pardi, Maria Allegrini, and S Patane. Polarization-modulation near-field optical microscope for quantitative local dichroism mapping. *Review of Scientific Instruments*, 73(5):2051–2056, 2002.

[146] Daniel Ploss, Arian Kriesch, Hannes Pfeifer, Peter Banzer, and Ulf Peschel. Generation and subwavelength focusing of longitudinal magnetic fields in a metallized fiber tip. *Optics Express*, 22(11):13744–13754, 2014.

[147] Qian Wang, Ginu Rajan, Pengfei Wang, and Gerald Farrell. Polarization dependence of bend loss for a standard singlemode fiber. *Optics Express*, 15(8):4909–4920, 2007.

[148] Nicolai Hartmann, Giovanni Piredda, Johann Berthelot, Gérard Colas Des Francs, Alexandre Bouhelier, and Achim Hartschuh. Launching propagating surface plasmon polaritons by a single carbon nanotube dipolar emitter. *Nano Letters*, 12(1):177–181, 2012.

[149] J. P.Balthasar Mueller and Federico Capasso. Asymmetric surface plasmon polariton emission by a dipole emitter near a metal surface. *Physical Review B - Condensed Matter and Materials Physics*, 88(12):1–6, 2013.

[150] B. N. Tugchin, N. Janunts, M. Steinert, K. Dietrich, E. B. Kley, A. Tünnermann, and T. Pertsch. Quasi-linearly polarized hybrid modes in tapered and metal-coated tips with circular apertures: Understanding the functionality of aperture tips. *New Journal of Physics*, 19(6), 2017.

[151] Milton Kerker, D-S Wang, and CL Giles. Electromagnetic scattering by magnetic spheres. *JOSA*, 73(6):765–767, 1983.

[152] R Alaee, R Filter, D Lehr, F Lederer, and C Rockstuhl. A generalized kerker condition for highly directive nanoantennas. *Optics Letters*, 40(11):2645–2648, 2015.

[153] Seung-Yeol Lee, Il-Min Lee, Junghyun Park, Sewoong Oh, Wooyoung Lee, Kyoung-Youm Kim, and Byoungho Lee. Role of magnetic induction currents in nanoslit excitation of surface plasmon polaritons. *Physical Review Letters*, 108(21):213907, 2012.

[154] Yang Zhang, Elizabeth Boer-Duchemin, Tao Wang, Benoit Rogez, Geneviève Comtet, Eric Le Moal, Gérald Dujardin, Andreas Hohenau, Christian Gruber, and Joachim R. Krenn. Edge scattering of surface plasmons excited by scanning tunneling microscopy. *Optics Express*, 21(12):13938, 2013.

[155] Sergejs Boroviks, Christian Wolff, Jes Linnet, Yuanqing Yang, Francesco Todisco, Alexander S. Roberts, Sergey I. Bozhevolnyi, Bert Hecht, and N. Asger Mortensen. Interference in edge-scattering from monocrystalline gold flakes [Invited]. *Optical Materials Express*, 8(12):3688, 2018.

[156] Johann Berthelot, Alexandre Bouhelier, Gérard Colas Des Francs, Jean-Claude Weeber, and Alain Dereux. Excitation of a one-dimensional evanescent wave by conical edge diffraction of surface plasmon. *Optics Express*, 19(6):5303–5312, 2011.

[157] Si Luo, Hangbo Yang, Yuanqing Yang, Ding Zhao, Xingxing Chen, Min Qiu, and Qiang Li. Controlling wave-vector of propagating surface plasmon polaritons on single-crystalline gold nanoplates. *Scientific Reports*, 5(August):1–8, 2015.

[158] Tingting Zhang, Chi Wang, Huan Chen, Chengyun Zhang, Zhenglong Zhang, Yurui Fang, and Hairong Zheng. Controlled Multichannel Surface Plasmon Polaritons Transmission on Atomic Smooth Silver Triangular Waveguide. *Advanced Optical Materials*, 7(21), 2019.

[159] Lin Gu, Wilfried Sigle, Christoph T. Koch, Burcu Ögüt, Peter A. Van Aken, Nahid Talebi, Ralf Vogelgesang, Jianlin Mu, Xiaogang Wen, and Jian Mao. Resonant wedge-plasmon modes in single-crystalline gold nanoplatelets. *Physical Review B - Condensed Matter and Materials Physics*, 83(19):1–7, 2011.

[160] Franz-Philipp Schmidt, Harald Ditlbacher, Ulrich Hohenester, Andreas Hohenau, Ferdinand Hofer, and Joachim R Krenn. Universal dispersion of surface plasmons in flat nanostructures. *Nature Communications*, 5(1):1–6, 2014.

[161] Edson P Bellido, Alejandro Manjavacas, Yue Zhang, Yang Cao, Peter Nordlander, and Gianluigi A Botton. Electron energy-loss spectroscopy of multipolar edge and cavity modes in silver nanosquares. *ACS Photonics*, 3(3):428–433, 2016.

[162] Frederik Walla, Matthias M Wiecha, Nicolas Mecklenbeck, Sabri Beldi, Fritz Keilmann, Mark D Thomson, and Hartmut G Roskos. Anisotropic excitation of surface plasmon polaritons on a metal film by a scattering-type scanning near-field microscope with a non-rotationally-symmetric probe tip. *Nanophotonics*, 7(1):269–276, 2018.

[163] Ziheng Yao, Suheng Xu, Debo Hu, Xinzhong Chen, Qing Dai, and Mengkun Liu. Nanoimaging and nanospectroscopy of polaritons with time resolved s-snom. *Advanced Optical Materials*, 8(5):1901042, 2020.

[164] Upkar Kumar, Sreenath Bolisetty, Raffaele Mezzenga, Christian Girard, Erik Dujardin, and Aurelien Cuche. Single plasmon spatial and spectral sorting on a crystalline two-dimensional plasmonic platform. *Nanoscale*, 12(25):13414–13420, 2020.

[165] L Salomon, G Bassou, H Aourag, JP Dufour, F De Fornel, F Carcenac, and AV Zayats. Local excitation of surface plasmon polaritons at discontinuities of a metal film: Theoretical analysis and optical near-field measurements. *Physical Review B*, 65(12):125409, 2002.

[166] N Abbasirad, A Barreda, D Arslan, M Steinert, YJ Chen, JS Huang, I Staude, F Setzpfandt, and T Pertsch. Near-field interference map due to a dipolar emission near the edge of a monocrystalline gold platelet. *Journal of Optics*, 24(12):125001, 2022.

[167] A. Archambault, T. V. Teperik, F. Marquier, and J. J. Greffet. Surface plasmon Fourier optics. *Physical Review B - Condensed Matter and Materials Physics*, 79(19):1–8, 2009.

[168] Di Zhu, Zhaogang Dong, Hong Son Chu, Yuriy A. Akimov, and Joel K.W. Yang. Image Dipole Method for the Beaming of Plasmons from Point Sources. *ACS Photonics*, 1(12):1307–1312, 2014.

[169] Reuven Gordon. Vectorial method for calculating the fresnel reflection of surface plasmon polaritons. *Physical Review B*, 74(15):153417, 2006.

[170] Mattin Urbieta, Marc Barbry, Yao Zhang, Peter Koval, Daniel Sánchez-Portal, Nerea Zabala, and Javier Aizpurua. Atomic-scale lightning rod effect in plasmonic picocavities: A classical view to a quantum effect. *ACS Nano*, 12(1):585–595, 2018.

[171] Jeppe S Clausen, Emil Højlund-Nielsen, Alexander B Christiansen, Sadegh Yazdi, Meir Grajower, Hesham Taha, Uriel Levy, Anders Kristensen, and N Asger Mortensen. Plasmonic metasurfaces for coloration of plastic consumer products. *Nano Letters*, 14(8):4499–4504, 2014.

[172] Sabine Dobmann, Arian Kriesch, Daniel Ploss, and Ulf Peschel. Near-field analysis of bright and dark modes on plasmonic metasurfaces showing extraordinary suppressed transmission. *Advanced Optical Materials*, 2(10):990–999, 2014.

[173] Francesco Monticone and Andrea Alu. Metamaterials and plasmonics: From nanoparticles to nanoantenna arrays, metasurfaces, and metamaterials. *Chinese Physics B*, 23(4):047809, 2014.

[174] Hou-Tong Chen, Antoinette J Taylor, and Nanfang Yu. A review of metasurfaces: physics and applications. *Reports on Progress in Physics*, 79(7):076401, 2016.

[175] Patrice Genevet, Federico Capasso, Francesco Aieta, Mohammadreza Khorasaninejad, and Robert Devlin. Recent advances in planar optics: from plasmonic to dielectric metasurfaces. *Optica*, 4(1):139–152, 2017.

[176] Cheng-Wei Qiu, Tan Zhang, Guangwei Hu, and Yuri Kivshar. Quo vadis, metasurfaces? *Nano Letters*, 21(13):5461–5474, 2021.

[177] Hui-Hsin Hsiao, Cheng Hung Chu, and Din Ping Tsai. Fundamentals and applications of metasurfaces. *Small Methods*, 1(4):1600064, 2017.

[178] Nina Meinzer, William L Barnes, and Ian R Hooper. Plasmonic meta-atoms and metasurfaces. *Nature Photonics*, 8(12):889–898, 2014.

[179] Yuri Kivshar and Andrey Miroshnichenko. Meta-optics with mie resonances. *Optics and Photonics News*, 28(1):24–31, 2017.

[180] Aleksandr Vaskin, Soheila Mashhadi, Michael Steinert, Katie E. Chong, David Keene, Stefan Nanz, Aimi Abass, Evgenia Rusak, Duk Yong Choi, Ivan Fernandez-Corbaton, Thomas Pertsch, Carsten Rockstuhl, Mikhail A. Noginov, Yuri S. Kivshar, Dragomir N. Neshev, Natalia Noginova, and Isabelle Staude. Manipulation of Magnetic Dipole Emission from Eu 3+ with Mie-Resonant Dielectric Metasurfaces. *Nano Letters*, 19(2):1015–1022, 2019.

[181] Najmeh Abbasirad, Angela Barreda, Dennis Arslan, Michael Steinert, Stefan Fasold, Carsten Rockstuhl, Isabelle Staude, Frank Setzpfandt, and Thomas Pertsch. Investigation of dipole emission near a dielectric metasurface using a dual-tip scanning near-field optical microscope. *Nanophotonics*, 10(18):4511–4522, 2021.

[182] Denis G. Baranov, Roman S. Savelev, Sergey V. Li, Alexander E. Krasnok, and Andrea Alù. Modifying magnetic dipole spontaneous emission with nanophotonic structures. *Laser and Photonics Reviews*, 11(3), 2017.

[183] Mario Agio and Diego Martin Cano. The purcell factor of nanoresonators. *Nature photonics*, 7(9):674–675, 2013.

[184] M. Kuttge, E. J.R. Vesseur, A. F. Koenderink, H. J. Lezec, H. A. Atwater, F. J.García De Abajo, and A. Polman. Local density of states, spectrum, and far-field interference of surface plasmon polaritons probed by cathodoluminescence. *Physical Review B - Condensed Matter and Materials Physics*, 79(11):2–5, 2009.

[185] R. Sapienza, T. Coenen, J. Renger, M. Kuttge, N. F. Van Hulst, and A. Polman. Deep-subwavelength imaging of the modal dispersion of light. *Nature Materials*, 11(9):781–787, 2012.

[186] Dorian Bouchet, Mathieu Mivelle, Julien Proust, Bruno Gallas, Igor Ozerov, Maria F Garcia-Parajo, Angelo Gulinatti, Ivan Rech, Yannick De Wilde, Nicolas Bonod, et al. Enhancement and inhibition of spontaneous photon emission by resonant silicon nanoantennas. *Physical Review Applied*, 6(6):064016, 2016.

[187] Christian Girard. Near fields in nanostructures. *Reports on Progress in Physics*, 68(8):1883, 2005.

[188] Bert Hecht, Dieter W Pohl, Harry Heinzelmann, and Lukas Novotny. "tunnel" near-field optical microscopy: Tnom-2. In *Photons and Local Probes*, pages 93–107. Springer, 1995.

[189] Isabelle Staude, Andrey E Miroshnichenko, Manuel Decker, Nche T Fofang, Sheng Liu, Edward Gonzales, Jason Dominguez, Ting Shan Luk, Dragomir N Neshev, Igal Brener, et al. Tailoring directional scattering through magnetic and electric resonances in subwavelength silicon nanodisks. *ACS Nano*, 7(9):7824–7832, 2013.

[190] J Van de Groep and A Polman. Designing dielectric resonators on substrates: Combining magnetic and electric resonances. *Optics Express*, 21(22):26285–26302, 2013.

[191] Zhong-Jian Yang, Ruibin Jiang, Xiaolu Zhuo, Ya-Ming Xie, Jianfang Wang, and Hai-Qing Lin. Dielectric nanoresonators for light manipulation. *Physics Reports*, 701:1–50, 2017.

[192] Craig F Bohren and Donald R Huffman. *Absorption and scattering of light by small particles*. John Wiley & Sons, 2008.

[193] Ling Lu, John D Joannopoulos, and Marin Soljačić. Topological states in photonic systems. *Nature Physics*, 12(7):626–629, 2016.

[194] Antoine Canaguier-Durand, Romain Pierrat, and Rémi Carminati. Cross density of states and mode connectivity: Probing wave localization in complex media. *Physical Review A*, 99(1):013835, 2019.

[195] Dennis Arslan, Aso Rahimzadegan, Stefan Fasold, Matthias Falkner, Wenjia Zhou, Maria Kroychuk, Carsten Rockstuhl, Thomas Pertsch, and Isabelle Staude. Toward perfect optical diffusers: Dielectric huygens' metasurfaces with critical positional disorder. *Advanced Materials*, page 2105868, 2021.

[196] Khant Minn, Blake Birmingham, and Zhenrong Zhang. New development of nanoscale spectroscopy using scanning probe microscope. *Journal of Vacuum Science & Technology A: Vacuum, Surfaces, and Films*, 38(3):030801, 2020.

[197] Y Gorodetski, A Niv, V Kleiner, and E Hasman. Observation of the spin-based plasmonic effect in nanoscale structures. *Physical Review Letters*, 101(4):043903, 2008.

[198] Anton Vakulenko, Svetlana Kiriushechkina, Mingsong Wang, Mengyao Li, Dmitry Zhirihin, Xiang Ni, Sriram Guddala, Dmitry Korobkin, Andrea Alù, and Alexander B Khanikaev. Near-field characterization of higher-order topological photonic states at optical frequencies. *Advanced Materials*, 33(18):2004376, 2021.

[199] B. le Feber, J. E. Sipe, M. Wulf, L. Kuipers, and N. Rotenberg. A full vectorial mapping of nanophotonic light fields. *Light: Science and Applications*, 8(1), 2019.

[200] B. Hecht, H. Bielefeldt, D. W. Pohl, L. Novotny, and H. Heinzelmann. Influence of detection conditions on near-field optical imaging. *Journal of Applied Physics*, 84(11):5873–5882, 1998.